

**SPECTRAL ANALYSIS OF
LITHIUM-BEARING MICAS
WITH SHORTWAVE AND
LONGWAVE INFRARED
SPECTROSCOPY**

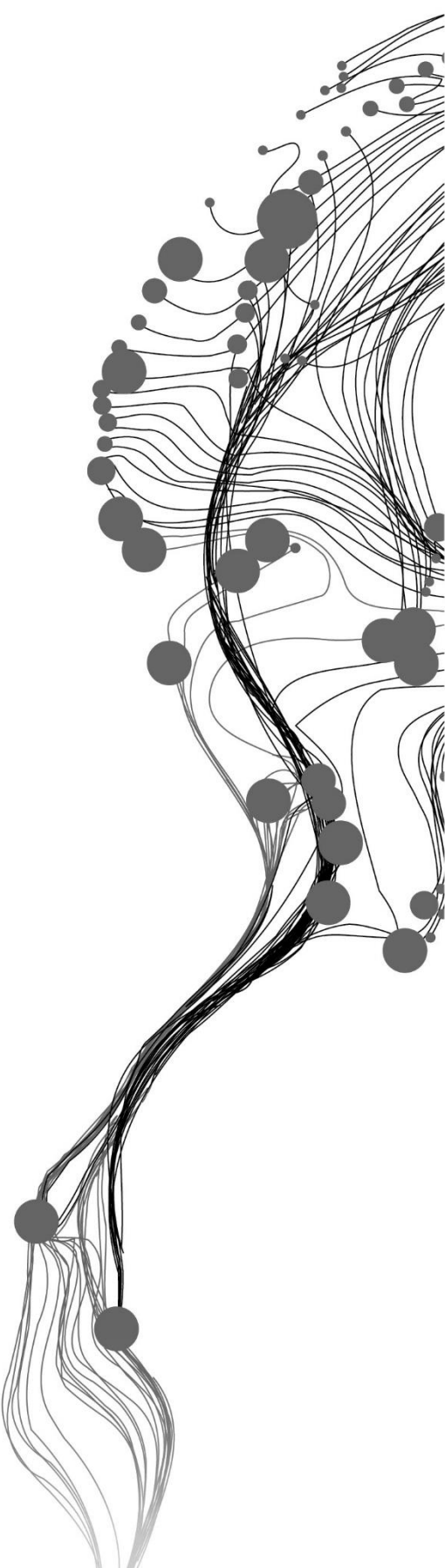
SELAMAWIT ABDISSA MEKONENN

August, 2023

SUPERVISORS:

Dr. A.H Dijkstra

Dr. C.A Hecker



SPECTRAL ANALYSIS OF LITHIUM-BEARING MICAS WITH SHORTWAVE AND LONGWAVE INFRARED SPECTROSCOPY

SELAMAWIT ABDISSA MEKONENN

Enschede, The Netherlands, August, 2023

Thesis submitted to the Faculty of Geo-Information Science and Earth Observation of the University of Twente in partial fulfilment of the requirements for the degree of Master of Science in Geo-information Science and Earth Observation.

Specialization: Applied Remote Sensing for Earth Observations

SUPERVISORS:

Dr. A.H Dijkstra

Dr. C.A Hecker

THESIS ASSESSMENT BOARD:

Dr. J.C Afonso (Chair)

Dr. F.S Desta (External Examiner, Delft University)

DISCLAIMER

This document describes work undertaken as part of a programme of study at the Faculty of Geo-Information Science and Earth Observation of the University of Twente. All views and opinions expressed therein remain the sole responsibility of the author, and do not necessarily represent those of the Faculty.

ABSTRACT

Lithium is one of the critical raw materials used for many applications, including rechargeable batteries for electric vehicles, laptops, and cell phones. Minerals, particularly mica minerals, are the most common and economically valuable lithium-bearing minerals found in hard rock. However, it is essential to recognize that not all mica minerals contain lithium; therefore, identifying and distinguishing mica minerals is crucial. The spectral characteristics obtained from infrared spectroscopy play a vital role in identifying and distinguishing mica minerals. Nevertheless, numerous factors can influence the diagnostic spectral features of mica minerals. Among these, elemental substitutions have a significant impact on changing the diagnostic features of mica minerals. This study aims to analyze the spectral characteristics of natural mica minerals and the effect of elemental substitution on the shift of absorption features using long-wave infrared (LWIR), mid-wave infrared (MWIR), visible to near infrared (VNIR), and short-wave infrared (SWIR) spectroscopy, integrated with electron microprobe analysis (EMPA) and X-ray diffraction (XRD). A total of 27 mica mineral samples were used to analyze their spectral characteristics. A spectral stack and scatter plot using major octahedral cation contents were employed to discern the spectral feature differences and determine the shift of absorption features.

The EMPA result showed that Si(IV) and Al(IV) are the major tetrahedral cations, while Al(VI), Fe(VI), and Mg(VI) are the major octahedral cations in the studied mica. Additionally, minor concentrations of Cr(VI), Ti(VI), and Mn(VI) also comprise the studied mica. XRD analysis demonstrates that the studied mica minerals exhibit similar diffraction patterns due to peak shifts caused by height differences. On the other hand, the LWIR-MWIR results showed that the studied mica minerals exhibit distinctive absorption features. Additionally, the absorption features obtained from the LWIR part of the spectrum resolve the absorption peak associated with Li-OH bending vibrations. Moreover, mica minerals such as muscovite display a systematic shift in absorption peaks due to the substitution of Al(VI) and Mg(VI) in the octahedral site. In the VNIR-SWIR regions, the studied mica minerals exhibit prominent absorption features. Spectral differences in terms of shape (symmetry and depth) and wavelength positions, resulting from variations in concentrations of major and minor element octahedral cations, allowed for the identification of the studied mica minerals. The stacked spectral features based on increasing major cations such as Al(VI) and Mg(VI) and scatter diagrams plotting 2200 nm features against Al(VI) and Mg(VI) content also display a systematic shift of wavelength positions. Generally, this study demonstrated the limitations of XRD and SWIR spectroscopy for distinguishing the studied mica minerals. Conversely, the LWIR analytical technique emerges as the most promising technique for differentiating the studied micas as well as distinguishing lithium-bearing micas.

Keywords: LWIR and MWIR spectroscopy, VNIR and SWIR spectroscopy, mica minerals, lithium-bearing mica, elemental substitutions

ACKNOWLEDGEMENTS

First and foremost, I would like to thank University of Twente for giving me a great chance to pursue a master's degree in Applied Remote Sensing for Earth Observations (ARS) at the Faculty of the International Institute for Geoinformation Science and Earth Observations (ITC).

I would like to acknowledge the Netherlands University Foundation for International Cooperation (NUFFIC) for financial support during the two years of my study.

I would like to express my sincere appreciation to my supervisors, Dr. Arjan Dijkstra and Dr. Chris Hecker, for their continuous follow-up and guidance, insightful comments, and encouragement from the preproposal formulations until the end of my thesis.

I would also like to thank Dr. Juan Carlos Afonso for his valuable comments and suggestions during the proposal defense and mid-term presentation.

My special thanks go to ITC geoscience laboratory assistants Kathrin Zweers-Peter and Camilla Marcatelli for the assistance on XRD, FTIR-ATR, and ASD Field Spec3 laboratory measurements.

Special thanks to the Utrecht University Geoscience Laboratory staff, particularly Dr. Eric Hellebrand and Tilly Bouten, for their invaluable support and assistance during the EMPA measurement.

Last but not least, I extend my heartfelt gratitude to my family and friends for their support and encouragement during my studies.

TABLE OF CONTENTS

1	INTRODUCTION	1
1.1	Background and Justification	1
1.2	Research Objectives	5
1.2.1	Main Objective	5
1.2.2	Specific Objectives	5
1.3	Research questions	5
1.4	Mica Minerals	6
1.5	Thesis structure	7
2	DATA AND METHODS	9
2.1	Dataset	9
2.1.1	Single-mineral mica samples	9
2.1.2	Rock samples	10
2.2	Analytical Methods	12
2.2.1	Electron Microprobe Analysis (EMPA)	12
2.2.2	X-Ray diffraction (XRD)	13
2.2.3	LWIR-MWIR Spectroscopy	14
2.2.4	VNIR-SWIR reflectance spectroscopy	14
2.2.5	SWIR imaging spectroscopy	15
3	EMPA AND XRD RESULTS	17
3.1	EMPA results	17
3.1.1	Classifications of the studied mica minerals	21
3.2	XRD results	23
4	LWIR-MWIR RESULTS	25
4.1	LWIR-MWIR spectral features of the studied mica minerals	25
4.2	Comparison of the LWIR-MWIR spectral features of the studied trioctahedral types of mica	35
5	VNIR-SWIR RESULTS	38
5.1	VNIR-SWIR spectral characteristics of the studied mica minerals	38
5.2	Comparison of the VNIR-SWIR spectral characteristics of the studied trioctahedral types of mica	50
5.3	Comparison of the VNIR-SWIR spectral characteristics of the studied lepidolite and muscovite mica	51
6	CALCULATIONS OF COMBINATION AND OVERTONES AND COMPARISON WITH OBSERVED FEATURES	57
7	DISCUSSION	60
7.1	Methods	60
7.2	Discussion on the results	63
7.2.1	The link between the LWIR-MWIR spectral features and elemental substitutions	63
7.2.2	The link between the SWIR spectral features and elemental substitutions	67

7.3	Application to imaging spectroscopy on Li-bearing rock	71
8	CONCLUSION AND RECOMMENDATION	74
	APPENDICES	79

LIST OF FIGURES

Figure 1.1: Structures of mica minerals, showing the alternating tetrahedral layers consisting of SiO ₄ tetrahedrons (where some Si can be replaced by Al), octahedral layers containing cations such as Mg, Fe, Al, Li, and/or vacancy, and the interlayers hosting cations such as K, Na and Ca. Figure taken from Jouandeh et al. (2021).....	7
Figure 2.1: Shows the sample preparation process for single-mineral mica samples for laboratory measurements. Figure A shows the Agate mortar and pestle used for crushing the samples. Figure B depicts the fine-grained fraction separated from the coarse-grained fraction using a <1 mm sieve.....	9
Figure 2.2: Shows the froth flotation technique to extract mica minerals (A) and the rock sample before and after the flotation technique (B).....	11
Figure 2.3: Shows sample preparation for electron microprobe analysis (EMPA) measurement. Figure A depicts the picked mica on the white plate before the resin. Figure B depicts the picked mica after the resin was poured.....	12
Figure 2.4: Methodological flowchart.....	16
Figure 3.1: Classification of the studied mica minerals plotted in terms of Mg-Li vs. tFe+Mn+Ti-Al(VI) (in a.p.f.u.) as calculated based on 11 oxygen atoms. In this diagram, a.p.f.u. stands for atom per formula unit, and tFe represents total iron.....	22
Figure 3.2: X-ray diffraction (XRD) patterns of the studied mica minerals. All the studied mica minerals depict similar diffraction peaks in the 5- 50° 2 θ range (Figure A). The shift of the peaks and peak height difference in the 25-29° 2 θ range (Figure B). Figure C shows the double diffraction peaks of the studied mica minerals. All the studied mica minerals do not have prominent diffraction patterns in the 35- 39° 2 θ (Figure D).....	24
Figure 4.1: LWIR and MWIR spectral features of the studied polyolithionite mica sample (LM 6). Figure A shows the distinct spectral features of the mineral in the OH-bending vibration region, and Figure B depicts the spectral features of the mineral in the OH-stretching vibration region.....	26
Figure 4.2: LWIR and MWIR spectral features of the studied lepidolite mica samples (offset for clarity). The samples are stacked based on increasing Si(IV) content in the tetrahedral site, as calculated from electron microprobe analysis. Figure A shows the spectral features of the studied lepidolite mica in the OH-bending vibration regions, and Figure B depicts the spectral features of the studied lepidolite in the OH-stretching vibration region.....	27
Figure 4.3: LWIR and MWIR spectral features of the studied zinnwaldite mica samples (offset for clarity). Figure A depicts the spectral features of the mineral in the OH-bending vibration region. Figure B displays the sharp and asymmetric absorption peaks of the zinnwaldite mica in the OH-stretching vibration region.....	28

Figure 4.4: LWIR and MWIR spectral features of biotite group mica samples (offset for clarity). Figure A shows the spectral features of the studied biotite group mica, in the OH-bending region. Figure B displays the spectral features of the minerals in the OH-stretching region.30

Figure 4.5: LWIR and MWIR spectral features of the studied muscovite mica samples (offset for clarity). Figure A shows the spectral features of the minerals in the OH-bend vibration region, and Figure B depicts the sharp and nearly symmetric absorption peaks of the minerals in the OH-stretch vibration region. The samples are stacked based on increasing Al(VI) content in the octahedral site, as calculated from electron microprobe analysis.31

Figure 4.6: Relation between the observed wavenumber position of main cation around 915 cm⁻¹ absorption peak in the LWIR reflection spectra of muscovite and their Al octahedral site occupancy calculated from the electron microprobe analysis. Linear regression results and R2 values are shown at the bottom right. 31

Figure 4.7: Relation between the observed wavenumber position of main cation around 3620 cm⁻¹ absorption peak in the LWIR reflection spectra of muscovite and their Al octahedral site occupancy calculated from the electron micro probe analysis. Linear regression results and R2 values are shown at the bottom right.32

Figure 4.8: LWIR and MWIR spectral features of the studied muscovite mica (offset for clarity). The samples are stacked based on increasing Mg(VI) content in the octahedral site, as calculated from electron microprobe analysis.32

Figure 4.9: Relation between the observed wavenumber position of the main cation around the 820 cm⁻¹ absorption peak in the LWIR reflection spectra of muscovite and their Mg octahedral site occupancy, as calculated from the electron microprobe analysis. Linear regression results and R2 values are shown at the bottom right.33

Figure 4.10: Relation between the observed wavenumber position of the main cation around the 3620 cm⁻¹ absorption peak in the LWIR reflection spectra of muscovite and their Mg octahedral site occupancy, as calculated from the electron microprobe analysis. Linear regression results and R2 values are shown at the bottom right.33

Figure 4.11: LWIR and MWIR spectral features of the studied fuchsite and muscovite mica minerals. Figure A shows the spectral features of the minerals in the OH-bending vibration region and the distinct absorption peaks of fuchsite at 880 cm⁻¹. Figure B depicts the sharp and symmetric absorption peak of the minerals in the OH-stretch vibration region.34

Figure 4.12: LWIR and MWIR spectral features of the studied trioctahedral types of mica. The samples are stacked based on the assumed increasing Li(VI) content in the octahedral site. Figure A depicts the distinct absorption features of the studied trioctahedral mica in the OH-bending vibration region. Figure B displays the absorption features of the studied trioctahedral types of mica in the OH-stretching region.36

Figure 5.1: VNIR and SWIR spectral characteristics of the studied polyolithionite mica (LM 6) in the 400–2500 nm range illustrated Figure A. Figure B depicts the spectral features of the studied polyolithionite mica

in the 2100–2500 nm range, specifically shows the precise wavelength position of the main octahedral cation, Al(VI).....	39
Figure 5.2: VNIR and SWIR spectral characteristics of the studied lepidolite mica samples in the 400–2500 nm range (offset for clarity). The samples are stacked based on increasing Al(VI) content in the octahedral site, as calculated from electron microprobe analysis (Figure A). Figure B depicts the absorption features of lepidolite mica in the 2100–2500 nm range, which shows the shift of the absorption features mainly around 2200 nm.....	40
Figure 5.3: Relation between the observed wavelength position of the main cation around 2200 nm absorption minimum in the reflection spectra of lepidolites and their Al octahedral site occupancy calculated from the electron probe microanalysis based on 22 oxygen, a total of 6 cations in this site based on this stoichiometry, Al(VI) means Al with a 6- fold coordination. Linear regression results and R2 values are shown at the bottom right.....	40
Figure 5.4: Relation between the observed wavelength position of the main cation-around 2200 nm absorption minimum in the reflection spectra of lepidolites and their Si tetrahedral site occupancy calculated from the electron probe microanalysis. Atoms per formula unit (a.p.f.u) based on 22 oxygen stoichiometry, so the maximum site occupancy of the tetrahedral site is 8 and only Si(VI) and Al(VI) are assumed to occupy the tetrahedral site. Linear regression results and R2 values shown at bottom right.	41
Figure 5.5: VNIR and SWIR spectral characteristics of the studied zinnwaldite mica samples (Figure A). The samples are stacked based on increasing Al(VI) content in the octahedral site, as calculated from electron microprobe analysis. Figure B shows the 2100–2500 nm spectral features of zinnwaldite formed as a result of octahedral cations, such as Al(VI) and Fe(VI).....	42
Figure 5.6: VNIR and SWIR spectral characteristics of the studied biotite group mica samples. Figure A illustrates the spectra feature of biotite group mica in the 400–2500 nm range. Figure B presents the spectral features of biotite group mica in the 2100–2500 nm range to show the precise wavelength positions of the absorption features formed due to the main cations, such as Fe and Mg.....	44
Figure 5.7: VNIR and SWIR spectral characteristics of siderophyllite mica. The samples are stacked based on increasing Fe(VI)and Mg(VI) content in the octahedral site, as calculated from electron microprobe analysis.....	44
Figure 5.8: Relation between the observed wavelength position of the main cation around 2250 nm absorption minimum in the reflection spectra of siderophyllite and their Fe octahedral site occupancy calculated from the electron probe microanalysis. Linear regression results and R2 values are shown at the bottom right.....	45
Figure 5.9: VNIR and SWIR spectral characteristics of the studied muscovite mica samples in the 400–2500 nm (Figure A). Figure B depicts the spectral features of muscovite mica in the 2100–2500 nm range to show the shift in wavelength position of the absorption feature formed by octahedral cations such as Al(VI) and Mg(VI) in the octahedral site. The samples are stacked based on increasing Al(VI) content, as calculated from the electron microprobe analysis.....	46

Figure 5.10: Relation between the observed wavelength position of the main cation around 2200 nm absorption minimum in the reflection spectra of muscovite and their Al octahedral site occupancy calculated from the electron probe microanalysis. Linear regression results and R2 values are shown at the bottom right.....47

Figure 5.11: VNIR and SWIR spectral characteristics of muscovite mica samples in the 400-2500 nm and 2100-2500 nm. The samples were stacked based on increasing Mg(VI) content in the octahedral site content, as calculated from electron microprobe analysis.....47

Figure 5.12: Relation between the observed wavelength position of the main cation around 2200 nm absorption minimum in the reflection spectra of lepidolites and their Mg octahedral site occupancy calculated from the electron probe microanalysis. Linear regression results and R2 values shown at bottom right.....48

Figure 5.13: Relation between the observed wavelength position of the main cation around 2200 nm absorption minimum in the reflection spectra of lepidolites and their Si tetrahedral site occupancy calculated from the electron probe microanalysis. Linear regression results and R2 values are shown at the bottom right.....48

Figure 5.14: VNIR and SWIR spectral characteristics of the studied fuchsite mica in the 400-2500 nm range. The mineral depicts a diagnostic absorption feature in the VNIR part of the spectrum at 425 nm and 621 nm.49

Figure 5.15: VNIR and SWIR spectral characteristics of the studied trioctahedral types of mica. The samples are stacked based on the assumed increasing Li(VI) octahedral site occupancy.....51

Figure 5.16: VNIR and SWIR spectral characteristics of lepidolite and muscovite micas. The samples are stacked based on increasing Al(VI) content in the octahedral site, as calculated from the electron microprobe analysis. The two mineral groups depict similar spectral characteristics, specifically in the SWIR part of the spectrum, due to the presence of OH, H₂O and Al-OH features.52

Figure 6.1: Shows wavelength positions of calculated and observed overtones and combinations of the studied muscovite mica samples. All the points falls on the 1:1 line (a line through 2195, 2195 and 2208,2208).59

Figure 7.1: LWIR and MWIR spectral characteristics of the studied trioctahedral and dioctahedral types of mica. Figure A depicts the distinct shape of the absorption features of the studied mica minerals in the OH-bending region. Figure B shows the spectral features of the studied mica in the OH-stretching region.62

Figure 7.2: VNIR and SWIR spectral characteristics of the studied trioctahedral and dioctahedral types of mica. Figure A displays the spectral characteristics of the studied mica minerals in the 400–2500 nm region and the diagnostic features of the studied zinnwaldite and fuchsite mica. Figure B shows the spectral features of the studied mica in the 2100–2500 nm region.....63

Figure 7.9: SWIR wavelength map of a pegmatite rock sample that contains mica minerals within and outside the veins. The image highlights mica minerals, which display absorption features in the 2190–2200 nm range (Figure A). Figure B displays the relation between the observed wavelength position of the main cation

around the 2200 nm absorption minimum in the reflection spectra of lepidolite and their Al octahedral site occupancy, as calculated based on 22 oxygen atoms. 72

Figure 7.10: SWIR wavelength map of a pegmatite rock sample containing mica minerals with different Al(VI) content. The image highlights mica minerals that show absorption features in the 2200–2014 nm range (Figure A). Figure B depicts the relationship between the observed wavelength position of the main cation around the 2200 nm absorption minimum in the reflection spectra of muscovite and their Al octahedral site occupancy, as calculated based on 22 oxygen atoms. 73

LIST OF TABLES

Table 2.1 Summary of specifications of ASD FieldSpec3 spectrometer (ASD, 2011)	15
Table 3.1 Mean chemical compositions of studied micas based on electron microprobe analysis of the epoxy mounted handpicked representative mica grains. The number of the analysis to calculate the reported mean (n) are given in the 4 th row.....	19
Table 4.1 Assignments of OH bands (cm ⁻¹) of the studied mica minerals	37
Table 5.1 Band assignments of absorption features (nm) of the studied mica minerals	53
Table 5.2 Name of the studied mica samples based on EMPA, LWIR and MWIR spectroscopy and VNIR and SWIR spectroscopy	55
Table 6.1 The calculated and observed overtones and combination of vibrational bonds of the studied mica minerals.	58

1 INTRODUCTION

1.1 Background and Justification

Critical raw materials (CRMs) are materials that have an essential role in modern technologies used in everyday life. In addition, CRMs play a significant role in combating climate change, being used as raw materials for energy transitions (Ferro & Bonollo, 2019; Pommeret et al., 2022). Due to this, the European Community lists 28 CRMs based on their essentiality for the development of the EU economy (European Commission, 2020).

Among these, lithium is one of the CRM used for many applications, such as rechargeable batteries for electric vehicles, laptops, and cell phones, and the production of glassware and ceramics, in particular (European Commission, 2020). In recent times, lithium has become a critical raw material due to the increasing demand for lithium batteries for electric vehicles (Breiter et al., 2019; Cardoso-Fernandes et al., 2020). In nature, this element does not exist as a native element. Pegmatite and granite and related magmatic deposits and evaporative brines are the main sources of lithium (Kesler et al., 2012). Due to the absence of brine distribution, hard rocks such as granite and pegmatite are the major sources of lithium on the European continent (Gourcerol et al., 2019).

Minerals that contain lithium in hard rocks are broadly classified as complex aluminum silicates, phosphates, and micas. However, not all minerals that contain lithium are economically valuable. The most common economically valuable lithium-bearing minerals are mica and spodumene (Kavanagh et al., 2018). Mica minerals are widely distributed in granitic rocks in the Variscan orogenic mountain belts, and they may be associated with granite pegmatite rocks containing spodumene (Dini et al., 2022).

Mica minerals are the most abundant rock-forming minerals in the earth's crust. They constitute the composition of all three types of rocks: igneous, sedimentary, and metamorphic. These minerals have a wide range of structural and chemical compositions (Tischendorf et al., 2007; Melka, 2009; LeGras et al., 2018). Despite their diverse range of structural and chemical composition, all mica minerals exhibit distinct basal cleavage and platy morphology, due to their layered atomic structure (Melka, 2009; Deer et al., 2013).

Different methods have been implemented to classify various types of mica species and analyze their spectral characteristics. Examples of such methods include electron microprobe analysis (EMPA), which successfully classifies octahedral-type micas based on the octahedral occupancy expressed by the parameters $Fe_{tot} + Mn + Ti - Al^{VI}$ and Mg-Li content (e.g., Tischendorf et al., 1997; Tischendorf et al., 2004). Raman spectroscopy has been used to study the spectral characteristics and effects of cationic substitution on the

shift of wavenumbers in synthetic trioctahedral types of mica (e.g., Robert et al., 1989). Similarly, infrared spectroscopy has been used to study the spectral characteristics of various mica minerals associated with chemical composition and crystalline structure (e.g., LeGras et al., 2018; Cardoso-Fernandes et al., 2021; Cloutier et al., 2021). Studies have shown that the spectral characteristics of a variety of mica minerals can be distinguished based on the diagnostic absorption features associated with the chemical composition and crystalline structure of the minerals. However, Raman spectroscopy has a lower spectral range and resolution than infrared spectroscopy. Compared to other techniques, infrared spectroscopy can be used to analyze samples that have any chemical composition (Besson & Drits, 1997). In recent times, infrared spectroscopy has been widely used in many geological applications. The method is capable of analyzing rocks and minerals of different sizes (Kholoshyn et al., 2020).

Infrared (IR) spectroscopy uses reflected light from different wavelengths to differentiate minerals based on their spectral response (Clark et al., 1990; Savitri et al., 2021). It extends from VNIR, 400–1300 nm, SWIR, 1300–2500 nm, MWIR, 3000–5000 nm, and LWIR, 8000–14000 nm (Clark, 1999; Savitri et al., 2021). The analysis of absorption features obtained from the SWIR and LWIR parts of the infrared spectrum has the potential for identifying and characterizing the structure and chemistry of mica minerals (LeGras et al., 2018).

SWIR spectroscopy is a method that provides valuable information about the chemical compositions and crystal structures of minerals, which is associated with the spectral response in distinct wavelength ranges (Lorenzo et al., 2021; Cloutier et al., 2021). The combinations and overtones of the fundamental absorption bands formed in the longwave part of the spectrum are responsible for the absorption features that are observed in the SWIR region of the spectrum. As a result, carbonates, sulfates, and Al- and Mg-bearing (OH) phyllosilicates (e.g., mica) mineral groups exhibit diagnostic spectral absorption features (Clark et al., 1990; Hecker et al., 2019). Studies have been carried out using this technique to analyze the spectral characteristics of mica group minerals and successfully distinguished several mica minerals based on the diagnostic absorption features related to the combination features of Al-OH (2200 nm), Fe-OH (2250 nm), and Mg-OH (2340 nm) (LeGras et al., 2018; Li et al., 2021).

LWIR and MWIR spectroscopy is another essential technique used to examine the possibility of recognizing the cationic substitution of the OH groups (Petit et al., 1999). Additionally, it has the potential to determine the composition of octahedral sheets using the fundamental vibrational modes retrieved from the long-wave and mid-wave parts of the spectrum. The crystal lattice and the chemical composition (site occupancy) affect the fundamental absorption features; this, in turn, means that the combinations and overtones are also affected, but not the other way around (Petit et al., 1999).

The absorption features on the mica minerals observed in the infrared part of the electromagnetic spectrum (SWIR and LWIR) are obtained from stretching fundamentals (e.g., ν Si-O, ν O-H) and first overtones

($2\nu\text{OH}$), bending fundamentals (eg. δOH) and combination bands of bending and stretching fundamentals ($\delta\text{OH}+\nu$) (LeGras et al., 2018). These absorption features are crucial for distinguishing and classifying a variety of mica minerals. Numerous factors would affect the diagnostic absorption features of mica minerals.

Among these, elemental substitutions have a significant impact on the shift of vibrational wavenumbers as well as the change in shape, position, and depth of absorption features of minerals depicted in infrared spectroscopy (Beran, 2002). The shift in the wavenumber and the changes in shape, and depth of absorption features are indications of the change in chemical composition and concentration of cations in mica minerals. Therefore, to distinguish and classify various mica minerals and determine the concentrations of the major cations, it is essential to analyze the influence of elemental substitutions associated with the vibrational fundamental features.

Different studies have been conducted to analyze the effect of elemental substitution on the shift of absorption features in a variety of mica minerals. Among these, Besson & Drits (1997) used infrared spectroscopy in the 3400 cm^{-1} - 3800 cm^{-1} wavenumber ranges to analyze the shift of OH-stretch wavenumbers due to the cationic substitution of Al, Mg, and Fe^{3+} in the dioctahedral type of mica. The result indicated the band of $\text{Al}^{3+}\text{-Al}^{3+}$ occurs between $3621\text{-}3658\text{ cm}^{-1}$ wavenumber range, Mg-Mg at 3583 cm^{-1} , Al- Fe^{3+} at 3573 cm^{-1} , and Al - Mg^{2+} exists at 3604 cm^{-1} , respectively. Additionally, the study showed that with the substitution of Al with Fe or Mg, the feature shifts to a lower wavenumber. On the other hand, Redhammer et al. (2000) analyzed synthetic trioctahedral mica (annite and siderophyllite) using infrared spectroscopy in the range of $4000\text{-}400\text{ cm}^{-1}$ to analyze cationic substitution of Al^{3+} , Fe^{2+} , and Fe^{3+} on the shift of OH-stretching wavenumbers. The result indicated that the band of $3\text{Fe}^{3+}\text{-OH}$ observed in the $3644\text{-}3667\text{ cm}^{-1}$, $2\text{Al}^{3+}\text{Fe}^{2+}\text{-OH}$ in the $360\text{-}3611\text{ cm}^{-1}$ range, and $2\text{Fe}^{2+}\text{Fe}^{3+}\text{-OH}$ in the $3621\text{-}3629\text{ cm}^{-1}$ range. Additionally, they identified the feature shifts towards the lower wavenumber with increasing Al^{3+} content. Martnez-Alonso et al. (2002) also used infrared spectroscopy to analyze the OH-related fundamental modes of vibration in dioctahedral mica (muscovite). In their study, they demonstrated the relationship between the shift of wavenumber of OH in-plane bend ($\delta\text{-OH}$) and OH stretch ($\nu\text{-OH}$) fundamental vibrations due to the cationic substitution of Al^{2+} , Fe^{3+} , and Mg^{2+} . They conclude that the substitution of Al with Fe^{3+} or Mg^{2+} causes the feature to shift to a lower wavenumber. This means the concentration of Al decreases when it is replaced by Fe^{3+} and Mg^{2+} . Recently, Cloutier et al. (2021) reviewed previous studies to determine the cause for the shift of SWIR spectroscopic absorption features of white mica (muscovite and celadonite). They reviewed the OH stretching vibration $\nu(\text{OH})$ of Al-Al occurs at $3621\text{-}3658\text{ cm}^{-1}$, Al-Mg at 3604 cm^{-1} , and Al- Fe^{3+} 3573 cm^{-1} . The OH in-plane bend $\delta(\text{OH})$ of Al-Al at 915 cm^{-1} , Al-Mg at 840 cm^{-1} , and Al- Fe^{3+} 875 cm^{-1} .

Previous studies were focused on analyzing the effect of cationic substitution of Al^{2+} , Al^{3+} , Fe^{2+} , Fe^{3+} , and Mg^{2+} on the shift of the wavenumbers of the OH-related fundamentals in the dioctahedral mica and

synthetic trioctahedral mica minerals, such as annite and siderophyllite. However, only a limited study specifically analyzed the effects of cationic substitution on the shift of wavenumbers and change in the shape of absorption features in the lithium-bearing mica minerals. One exception is, Robert et al. (1989) who analyzed the influence of cationic substitution of Al, Mg, and Li on the shift of OH-stretching wavenumbers in the trioctahedral type of mica using Raman and Infrared (IR) spectrometry. The result showed a shift in OH-stretching wavenumbers associated with the OH group bonded to cations; for instance, Mg_2Li or Li_2Al were seen to be associated with a spectral feature in the $3755\text{-}3740\text{ cm}^{-1}$ wavenumber range, Mg_3 or $AlMgLi$ gave a feature in $3740\text{-}3715\text{ cm}^{-1}$ wavenumber range, and Mg_2Al or Al_2Li yielded a feature at less than 3700 cm^{-1} . The study concluded that a systematic shift was observed toward shorter wavenumbers (higher wavelength) in all types of trioctahedral bands as the bulk Al content increased in mica.

Nevertheless, the nature of the trioctahedral mica used by Robert et al. (1989) was synthetic, and they only studied the effect of elemental substitution in the OH-stretching vibration region. In addition, they analyzed only a limited compositional range of the trioctahedral type of lithium-bearing mica (hydroxyl-bearing lepidolite mica series).

Therefore, this research aims to analyze the spectral characteristics of various types of natural mica minerals and investigate the effects of elemental substitution on the shift of wavelength and wavenumber positions and change of depth of absorption features using VNIR-SWIR ($350\text{-}2500\text{ nm}$) and LWIR-MWIR ($8000\text{-}370\text{ cm}^{-1}$) spectroscopy, integrated with electron microprobe analysis (EMPA) and X-ray diffraction (XRD). The study used 14 single-mineral mica samples and 13 pegmatite and granite rock samples. The results will determine whether lithium-bearing mica can be distinguished from non-lithium-bearing mica using IR spectroscopy. Finally, the results will provide insights into the relationship between the substitutions of main octahedral and tetrahedral cations and the shift of absorption features in both dioctahedral and trioctahedral types of mica.

1.2 Research Objectives

1.2.1 Main Objective

The main objective of the present study is to build a systematic understanding of the effect of elemental substitutions, including lithium, on the spectral behavior of dioctahedral and trioctahedral types of Li-bearing mica using VNIR-SWIR and LWIR-MWIR spectroscopy.

1.2.2 Specific Objectives

To accomplish the main objective of the study the following sub-objectives and research questions are formulated:

1. To analyze the spectral behavior and chemical compositions of a series of natural mica flakes using VNIR-SWIR and LWIR-MWIR spectroscopy, integrated with mineral chemical analysis (EMPA).
2. To evaluate infrared spectroscopy (LWIR and SWIR) as a method for distinguishing lithium-bearing mica from non-lithium-bearing mica.

1.3 Research questions

1. What are the spectral characteristics of mica minerals in the VNIR-SWIR and LWIR- MWIR spectroscopy?
2. What is the link between spectral features and chemical substitution?
3. Is infrared spectroscopy a valuable method for distinguishing lithium mica from non-lithium mica?
4. How do the combinations and overtones that we can calculate from the measured fundamental features compare to the combinations and overtones that we observe by SWIR spectroscopy?
5. How does elemental substitution, including lithium, influence the shift of the wavelength of fundamental absorption features and changes the position, and depth of absorption features of trioctahedral Li-mica?
6. How can we quantify lithium from Li-bearing mica flakes?

1.4 Mica Minerals

Micas are grouped under hydrated phyllosilicate minerals; they have a negatively charged 2:1 layer structure. Their crystal structure is primarily composed of two tetrahedral Si-O sheets and an octahedral Al, Mg, Fe, and Li-OH sheet (Melka, 2009) (*Figure 1.1*).

The simplified formula can be expressed by $IM_{2-3} \square_{1-0} T_4O_{10} A_2$ (Rieder et al., 1998; Yavuz, 2001; Melka, 2009). The symbol I has commonly represented the interlayers such as K, Na, and Ca, while the symbol M represented the cations, including Al, Fe, Mg, Mn, Li, Ti, and Cr, while \square represents vacancy. The symbol T mainly represented Be, Al, B, Fe, and Si, and A represented OH, F, and Cl (Rieder et al., 1998; Yavuz, 2001).

Based on the distribution of cations, the tetrahedral and octahedral sheets are distinguished systematically. The tetrahedral sheet is primarily comprised of four cations: Si, Al, Fe³⁺, and Be²⁺. Oxygen (O) is the main anion that constitutes the tetrahedral sheet of mica. On the other hand, the octahedral sheet is predominantly composed of Mg, Al, Fe²⁺, Fe³⁺, Li, Ti, Cr, and Mn cations. Hydroxyl (OH) and fluorine (F) are the main anions that build the octahedral types of mica. Both tetrahedral and octahedral sheets mainly composed of K, Na, and Ca interlayer cations (Tischendorf et al., 2007; LeGras et al., 2018).

The classification of mica group minerals involves various approaches, one of which is based on the occupancy of the interlayer cation. Based on this criterion, mica minerals can be classified into two types: true mica, which contains monovalent cations in the interlayer, and brittle mica, which contains divalent cations in the interlayer (Rieder et al., 1998, Melka, 2009, Deer et al., 2013). In addition, true mica can be further classified into common true potassium (K) mica, uncommon true-K micas, and uncommon true non-K micas. Similarly, the brittle type of micas can be further subdivided into common brittle micas and uncommon brittle micas (Tischendorf et al., 2007).

The common true-K mica predominantly contains major elements such as Mg, Fe, Al, and Li. Minerals including muscovite, phlogopite, and annite are examples of such common true-K micas. On the other hand, uncommon true-K micas comprise minor elements such as Mn²⁺, Fe³⁺, and F and are observed in minerals like fluorannite and ferriphlogopite (Tischendorf et al., 2007; Melka, 2009). The uncommon true non-K micas, which are primarily composed of monovalent cations, namely Na, Rb, Cs, or NH₄, as a major substituting for K, are typically observed in minerals like paragonite. The common brittle micas mostly contain Ca or Ba as the main cation for K substitution in minerals like margarite. In contrast, the uncommon brittle mica is composed of major elements such as V, Be, Fe, Ti, S, and O as major elements besides Ca or Ba and is observed in minerals like anandite (Tischendorf et al., 2007; Deer et al., 2013).

On the other hand, based on octahedral site occupancy, which is the most commonly used classification method, true and brittle mica can be further divided into dioctahedral and trioctahedral subgroups (Tischendorf et al., 2004; LeGras et al., 2018). In the dioctahedral type of mica, one in three cation sites is vacant, and the hydroxyl (OH) is bonded with the two cations and is situated on octahedral vacant sites. Muscovite, celadonite, and phengite are examples of minerals that belong to this group. In contrast, in the trioctahedral type of mica, all three sites are filled with a cation. Mineral examples from this group include biotite, lepidolite, and zinnwaldite (Robert et al., 1989; Tischendorf et al., 2004; Melka, 2009).

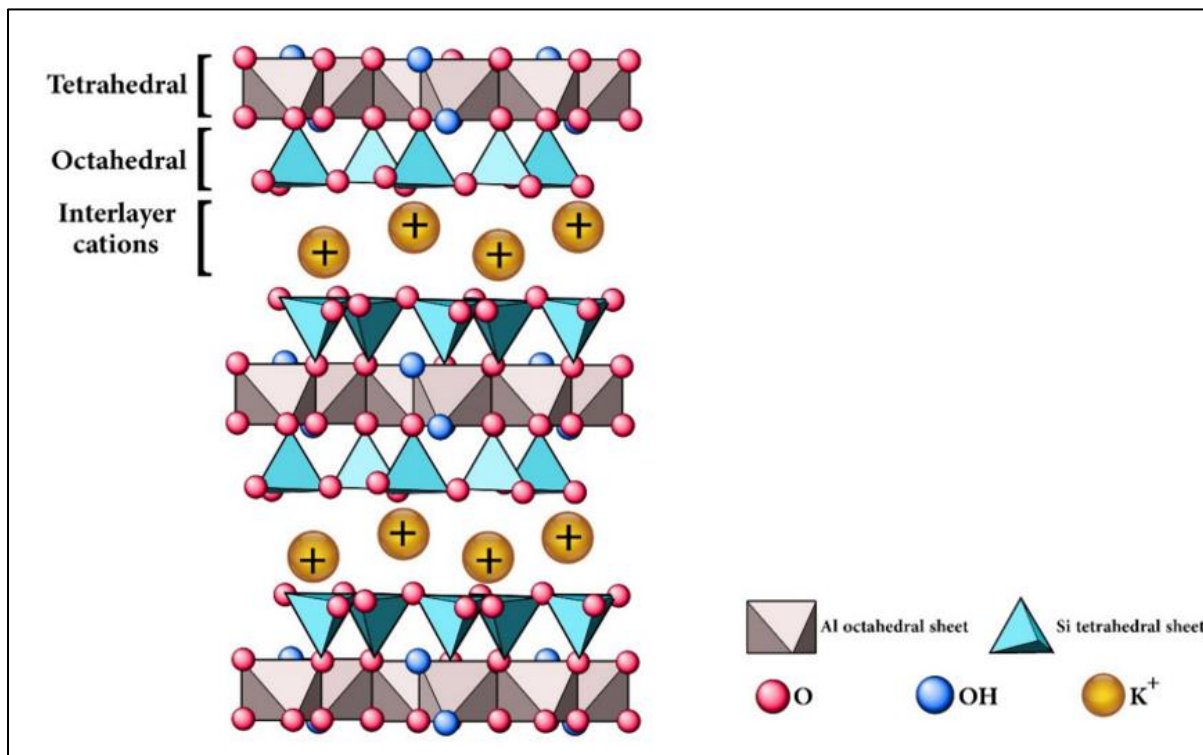


Figure 1.1: Structures of mica minerals, showing the alternating tetrahedral layers consisting of SiO_4 tetrahedrons (where some Si can be replaced by Al), octahedral layers containing cations such as Mg, Fe, Al, Li, and/or vacancy, and the interlayers hosting cations such as K, Na and Ca. Figure taken from Jouandeh et al. (2021).

1.5 Thesis structure

This thesis is structured into eight chapters. **Chapter 1** introduces the background and justification of the research, previous research, the research gap, the research objective, the research question, and background information about mica minerals. **Chapter 2** discusses the dataset and methods used in this study. **Chapter 3** presents results acquired from electron microprobe analysis (EMPA) and XRD. **Chapter 4** presents the results obtained from LWIR and MWIR spectroscopy. **Chapter 5** presents results acquired from VNIR and SWIR spectroscopy. **Chapter 6 (a mini-chapter)** demonstrates the calculation of combinations and overtones and comparison with observed features. **Chapter 7** discusses the results obtained from these methods, and finally, **Chapter 8** summarizes the research findings and makes recommendations for future research.

2 DATA AND METHODS

Single-mineral mica and mica-rich rock samples were the main data used for this study. The section below describes the dataset, sample preparation methods, and various analytical methods used for this study to accomplish the research objectives and answer the research questions. These methods include crushing single-mineral mica and rock samples, froth flotation of rock samples, and picking mica minerals from crushed rock samples. The analytical methods include electron microprobe analysis (EMPA), X-ray diffraction (XRD), LWIR-MWIR spectroscopy, VNIR-SWIR spectroscopy, and SWIR imaging spectroscopy. The data analysis was performed using Microsoft Excel, Hyppy, and ENVI 5.6.1 software. The list of the studied samples is found in Appendix 1. The datasets and methods used are described in detail in the section below.

2.1 Dataset

2.1.1 Single-mineral mica samples

In this study, a total of 14 single-mineral mica samples were used for laboratory analysis. These samples were collected by ITC staff during various research campaigns conducted in the Czech Republic, Portugal, Finland, and Zimbabwe. To prepare the samples for laboratory analysis, the following steps were employed: At the first step, the soft samples were crushed by hand, while the hard samples were crushed using a hammer. Subsequently, the crushed samples were ground using an Agate mortar and pestle. To obtain a consistent and homogenized sample, the powdered fractions were separated from the coarse-grained fraction using a <math><1\text{ mm}</math> sieve (*Figure 2.1*). The samples were labeled with the code LM, which stands for lithium mica.

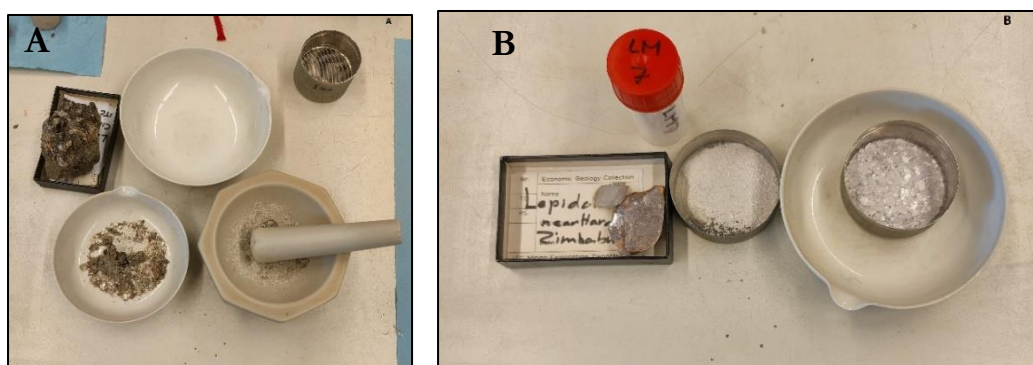


Figure 2.1: Shows the sample preparation processes for single-mineral mica samples for laboratory measurements. Figure A shows the Agate mortar and pestle used for crushing the samples. Figure B depicts the fine-grained fraction separated from the coarse-grained fraction using a <math><1\text{ mm}</math> sieve.

2.1.2 Rock samples

A total of 13 mica-rich rock samples consisting of granite and pegmatite were used for this study. These samples were collected by ITC staff in different research campaigns, including in the United Kingdom (Merrivale, Meldon, Cornwall, and Carn Brea), Germany (Cinovec), Scotland (Glen Gairn), New Mexico (Hardling), and Kazakhstan (Kalba Range). The samples were used for the extraction of additional mica minerals to fill in any compositional gaps in the series of micas available for this research. Additionally, one pegmatite rock sample was used for SWIR imaging spectroscopy analysis. For the extraction of mica minerals from the rock samples, different techniques were implemented, and detailed descriptions are provided in the section below.

2.1.2.1 Sample preparations for extraction of mica minerals from the rock samples

Crushing the rock sample using a hammer was the initial step for separating the mica minerals from the other minerals that constitute the rock samples. Then, the crushed samples were ground using an Agate mortar and pestle. A < 1 mm sieve was used to separate the fine-grained fraction from the coarse-grained fraction. To separate mica minerals from other minerals, the froth flotation technique was performed using distilled and mineral water (*Figure 2.2*).

The first experiment was conducted using ultrapure (distilled) water. In the first step, 250 ml of distilled water was poured into beakers, and a tube connected with compressed air was placed at the bottom of the beaker. The beaker containing the distilled water was then placed on the hot plate, and subsequently, 1 ml of sulfuric acid and liquid detergent were poured into the beaker. The addition of sulfuric acid and the liquid detergent aimed to produce a foam that carried mica minerals. Following this, the pulverized sample was added to the beaker (*Figure 2.2.A*). A magnetic stirrer was used to mix the pulverized samples with the water. The bubbles within the foam were generated by gently applying pressure to the compressed air connected to the tube. Finally, the filter paper was used to collect the floated fraction.

The second experiment was carried out using mineral water. Initially, the pulverized rock samples were rinsed with tap water to eliminate the very fine powder fractions that could not be picked up by a binocular microscope. The remaining pulverized samples that sank to the bottom were then mixed with 50 ml of tap water. In a separate container, 250 ml of mineral water was mixed with 1 ml of sulfuric acid and 2 ml of liquid detergent. The mineral water, mixed with sulfuric acid and liquid detergent, was poured into the beakers that contained the samples. The mixture was stirred gently on a magnetic stirrer to generate bubbles that carried mica and other minerals. Finally, the filter paper was used to collect the floated fractions.

Following the flotation method, hand-picking was performed on the floated fractions under a binocular microscope. Ethanol alcohol was used on the floated fractions to enhance the clarity of the minerals during picking.



Figure 2.2: Shows the froth flotation technique to extract mica minerals (A) and the rock sample before and after the flotation technique (B).

2.1.2.2 Sample preparations for electron microprobe analysis (EMPA) measurement

Sample preparation for EMPA measurement was carried out on both single-mineral mica and mica minerals extracted from the rock samples. For each mica sample, 3–7 grains were picked and mounted on a white and transparent plate, which was covered with white double-sided tape. After the grain-mounted samples dried and settled completely, the following day, a well-mixed solution of 5 grams of Araldite 2020 epoxy resin and 1.5 grams of Araldite 2020 was poured into a circular plastic block that was placed on the plate containing the mica mineral grains. After 24 hours, the resin underwent solidification and attained a sufficient degree of hardness to permit the removal of the plate and the circular block, leaving only the mounted grain attached to the solidified resin. The poured resin facilitated easy handling, polishing, and grinding of the grains. Subsequently, grinding and polishing were performed using sand papers of varying particle sizes (500, 1000, and 4000 grit), and finally, a fine-polishing stage using 1 μ m diamond paste was applied to make the grains completely flat and level. The grinding process was continued until all the grains were exposed to the surface, and their exposure was checked through a binocular microscope. The grain mounting, resin mounting, grinding, and polishing were carried out at the ITC geoscience laboratory.

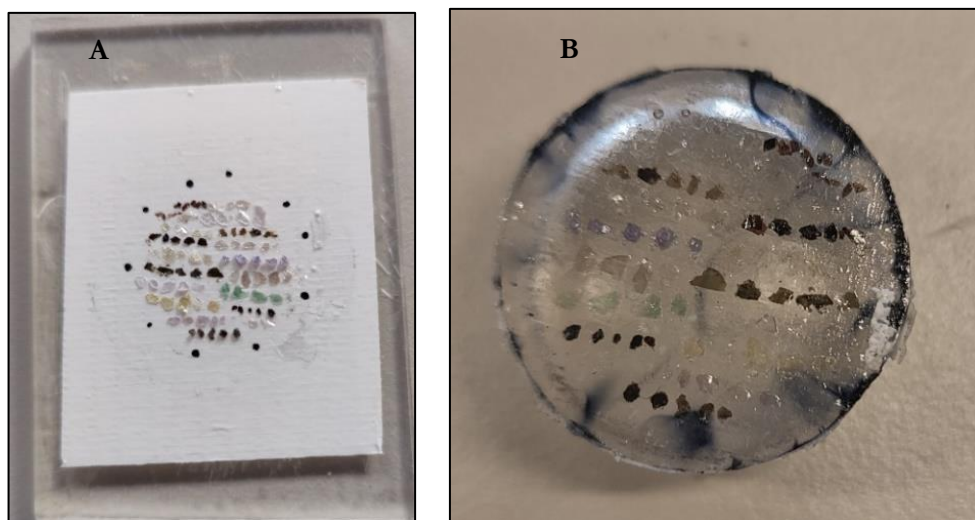


Figure 2.3: Shows sample preparation for electron microprobe analysis (EMPA) measurement. Figure A depicts the picked mica on the white plate before the resin. Figure B depicts the picked mica after the resin was poured.

2.2 Analytical Methods

Various analytical methods were implemented to analyze the spectral characteristics and effects of elemental substitutions on the shift of wavenumber (wavelength) and changes in the depth of absorption features in the studied mica minerals. These methods include, EMPA, XRD, LWIR-MWIR spectroscopy and VNIR-SWIR spectroscopy, and SWIR imaging spectroscopy. A detailed explanation of the methods is provided in the sections below.

2.2.1 Electron Microprobe Analysis (EMPA)

Electron microprobe analysis (EMPA) is a type of analytical method used to determine the major and trace element compositions of minerals. In this study, the method used to determine the major element concentration allowed for the calculation of the content of octahedral and tetrahedral cations as well as interlayers. The analysis was conducted at Utrecht University with the help of Dr. Eric Hellebrand and Tilly Bouten using a JEOL JXA-8530F Hyperprobe Field Emission Electron Probe Microanalyzer, which allows for better spatial resolution below 1 micron. The measurement was carried out using a wavelength dispersive spectrometer (WDS) with a 10 μm beam diameter. The operating conditions were a 15 kilovolts (kV) accelerating voltage and a 10 nanoampere (nA) beam current. The counting time for each element was 28 s. The crystals of elements were measured by thallium acid phthalate (TAP) for elements such as Si and Al; pentanerythritol (PETL) for Ti and Cr; lithium fluoride (LIFH) for Fe and Mn; tellurium aluminium phosphorus (TAPH) for Mg and N; and PETH for Ca and K. To calibrate the instrument (convert counts to concentrations), the standard reference minerals, such as KL-2 Kilauea glass for Si, Al, Hematite for Fe, Tephroite for Mn, Diopside for Ca and Mg, Jadeite for Na, K^+TiPO_5 for K and Ti, and Chromium metal for Cr, were measured before the measurement of the studied samples.

Before conducting the measurements, the mounts were cleaned using ethanol and coated with carbon to eliminate any gases and create a conductive layer. Additionally, as an unknown quality control measure, diopside and KL-2 glass standards were also measured three times after the sample measurements.

Subsequently, the major element concentrations of 27 mica mineral samples were acquired. Their tetrahedral and octahedral site occupancy were then calculated from the major element concentrations based on a formula unit of 22 oxygen stoichiometry, as recommended by Deer et al. (2013). For graphical representation of the studied mica, the octahedral site occupancy was recalculated using a formula unit of 11 oxygen stoichiometry, as suggested by Tischendorf et al. (2004). To estimate Li concentrations in the trioctahedral types of mica, specifically siderophyllite mica, this study employed major element correlations, such as MgO, as recommended by Tischendorf et al. (1999; 2004), using the formula $\text{Li}_2\text{O} = [2.1 / (0.356 + \text{MgO})] - 0.088$. This formula is particularly relevant when the concentration of MgO is > 3 wt%.

However, for the studied trioctahedral types of mica minerals such as polyolithionite, lepidolite, and zinnwaldite, the lithium concentration could not be estimated using the formula $\text{Li}_2\text{O} = (0.289 * \text{SiO}_2) - 9.658$, $F > 4$. Similarly, for the dioctahedral types of mica such as muscovite and fuchsite, it was not possible to estimate the concentration of lithium using the formula $\text{Li}_2\text{O} = 0.39356 * F^{1.326}$, $F < 4$. These limitations arose due to the lack of Fluorine (F) concentration data of the studied mica minerals, which are required in the respective formulas. This is because lithium has a positive correlation with fluorine (F) in mica minerals.

As a result, for the dioctahedral types of mica, except for sample LM 5, which has an assumed lithium concentration of $\text{Li}_2\text{O} = 0.10$ Wt%, all the remaining samples were assigned zero lithium concentrations. This assumption was made based on the location of the sample. Specifically, sample LM 5 comes from Hardling, where lithium extraction takes place.

On the other hand, for assuming the concentration of lithium in the trioctahedral type mica, this study used the data from *mindat.org*. Subsequently, using mindat.org data, the lithium concentrations were assumed for polyolithionite, lepidolite, and zinnwaldite. The polyolithionite sample assumed lithium-oxide concentrations of 6.5 wt%, all the lepidolite samples assumed lithium-oxide concentrations of 6.00 wt%, and the zinnwaldite samples assumed lithium-oxide concentrations of 3.50 wt%. After that, the Li content in the octahedral site was calculated for the studied mica minerals.

2.2.2 X-Ray diffraction (XRD)

The X-ray diffraction (XRD) measurement was used for the identification of the studied mica minerals. The measurements were obtained using a Bruker D2 phaser X-ray diffractometer with a Cu X-ray source at the ITC geoscience laboratory. The measurements were conducted on the powdered samples, which had a grain size of less than 1mm, using a silicon wafer sample holder. The spectra were measured from 6 to 70° 2 theta

value with an increment of 0.012° and an average time per measurement of 574 s; = 10 scans were typically collected, so one full measurement took ~ 95 minutes. Measurements were taken using a 0.6 mm divergence slit, a 1 mm knife, and a 8 mm detector slit. Mineral identification was performed by manually searching mineral names using DIFFRAC. EVA version 3.1 software.

2.2.3 LWIR-MWIR Spectroscopy

The LWIR-MWIR spectral characteristics measurements were used to determine the OH-bending (δ -OH) and OH-stretching (ν -OH) fundamental vibrations in the tetrahedral and octahedral environments. The spectra were collected using Bruker Vertex 70 FTIR-ATR spectroscopy equipped with a DLaTGS detector at the ITC Geoscience Laboratory. The instrument was cooled to room temperature and purged with dry air. Each mineral sample consisted of 128 cm^{-1} sample scan time in the spectral range 8000 cm^{-1} - 370 cm^{-1} with a resolution of 2 wavenumbers. Before measuring the spectra of minerals, background measurements were taken on an empty Attenuated Total Reflectance (ATR) device to calibrate the instrument for individual samples.

Before obtaining the ATR spectra, the powdered mineral samples were kept in the oven at 50°C for 15 hours. This drying procedure was performed to eliminate the adsorbed water from the samples. The following day, the heated samples were stored in the desiccator to keep them dry. A plastic Petri dish sample holder was used when the samples were moved to the ATR room. For one measurement, 0.10 g of powdered samples were used, weighted by a Sartorius balance. The spectra of each mineral sample were measured three times on different times and days to see whether the spectral response of the minerals did not change.

2.2.4 VNIR-SWIR reflectance spectroscopy

The VNIR-SWIR spectral characteristics of the studied mica minerals were acquired using an ASD FiledSpec3 spectrometer in the 350–2500 nm wavelength range. The reflectance spectra were obtained in the VNIR (400–1300 nm) and SWIR (1300–2500 nm) regions. The measurements were conducted on the powdered mica mineral samples using a contact probe attachment equipped with an internal light source at the ITC geoscience laboratory.

Before measuring the powdered sample, optimization and a white reference (a material that 100% reflected the incoming light) were measured. The white reference was used to convert measured radiant energy intensity to reflectance values between 0 and 1. The spectrum averaging and the white reference were set to 40 readings per measurement during referencing. Additionally, 100 readings were set for dark current measurements. Ten measurements were taken for each sample, and splice correction was performed for each spectra using Viewspecpro software to remove the intensity offset in the spectra. Then, the splice-

corrected spectra were exported as ASCII files to be displayed in the ENVI software. Reflectance spectra measurements of a Mylar reference material (NIST SRM-1920a) and an in-house ruby standard showed that the wavelength accuracy of the ASD instrument was better than 1.5 nm across the entire wavelength range (A.H. Dijkstra, personal communication).

Table 2.1 Summary of specifications of ASD FieldSpec3 spectrometer (ASD, 2011)

Specification	Value
Wavelength range	350-2500 nm
Spectral resolution	3 nm at 700 nm
	10 nm at 1400 nm
	10 nm at 2100 nm
Sampling interval	1.4 nm at 350-1050 nm
	2 nm at 100-2500 nm
Scanning time	100 milliseconds
Scans/Second	10 spectra per second

2.2.5 SWIR imaging spectroscopy

In this study, SWIR imaging spectroscopy was employed to evaluate the applicability of imaging spectroscopy for discriminating wavelength shifts resulting from variations in octahedral cation contents.

A SWIR Specim hyperspectral camera was used to acquire an image of a pegmatite rock sample. The image acquisition process involved scanning the sample in the SWIR (1000–2500 nm) range, at a spatial resolution of 256 μm . To prevent light interference, the measurement was performed in dark laboratory conditions. The scanning was done by placing a tray of sample on the stage of the camera. The measurement was conducted at the ITC geoscience laboratory.

After that, to enhance the image quality and obtain accurate data from the sample, different pre-processing steps, such as spatial and spectral sub-setting and masking to remove the noisy bands and unwanted space from the sample surface and Minimum Noise Fraction (MNF) to remove noisy spikes from the spectra, were done on the SWIR image of the sample.

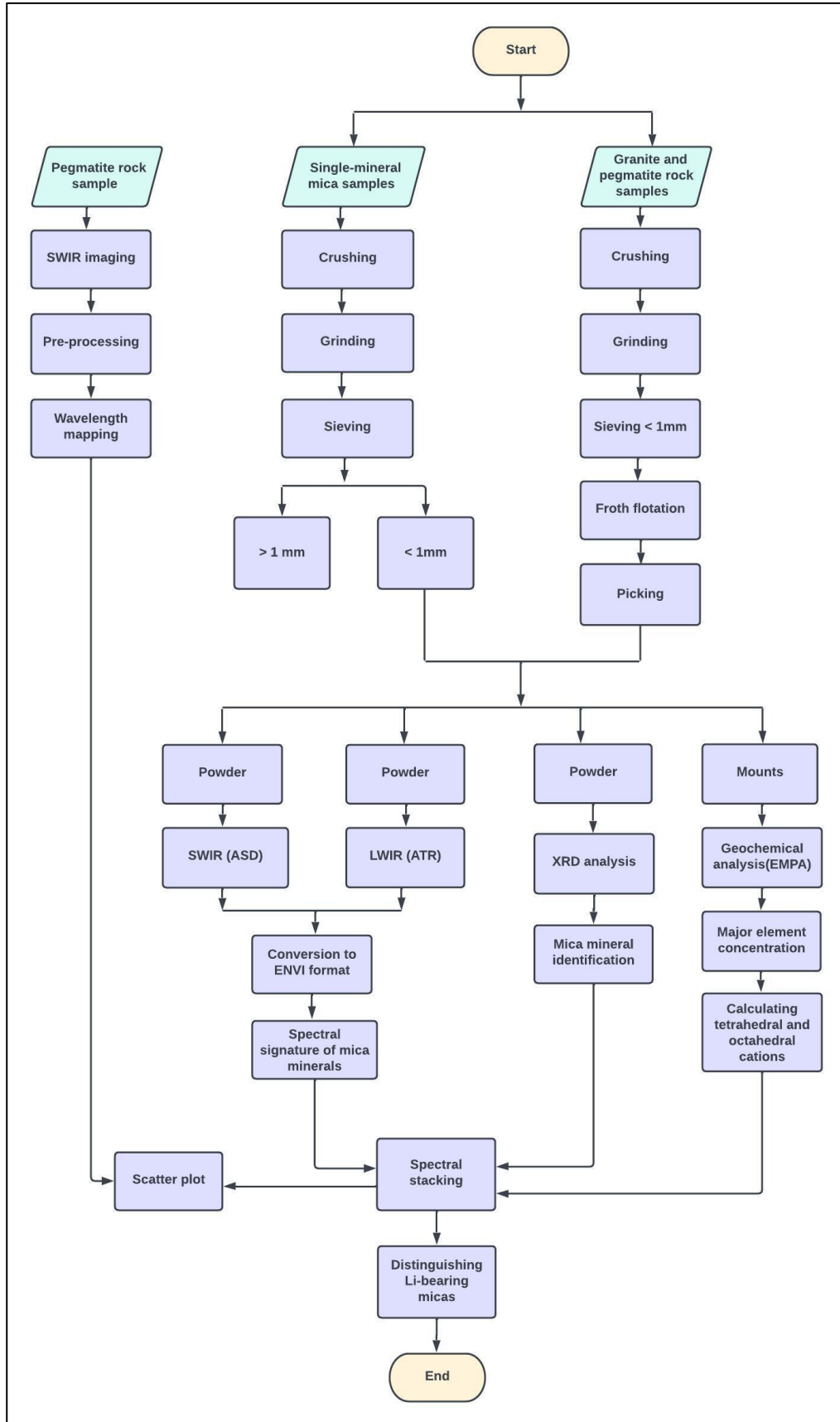


Figure 2.4: Methodological flowchart

3 EMPA AND XRD RESULTS

This chapter presents the results obtained from the electron microprobe analysis (EMPA) and X-ray diffraction (XRD) analytical methods. The chapter consists of two sections: the first section (section 3.1) describes the EMPA results of the studied mica minerals, and the second section (section 3.2) presents the XRD results of the studied mica minerals.

3.1 EMPA results

Based on their concentrations calculated using 22 oxygen stoichiometry, Al(IV) and Si(IV) are the predominant tetrahedral cations, while Al(VI), Fe(VI), and Mg(VI) are the predominant octahedral cations that comprise the studied mica minerals. In all the studied mica minerals, both dioctahedral and trioctahedral types of mica, the concentration of Ca and Na in the interlayer is very low, approaching zero. In contrast, the concentration of K is relatively high, with an average of around 2. Therefore, K is the predominant interlayer in all the studied mica minerals.

The table below shows the major element concentrations that constituted the studied mica minerals, calculations of tetrahedral and octahedral site occupancy based on 22 and 11 oxygen stoichiometry, lithium assumptions, and concentrations of interlayer cations.

SPECTRAL ANALYSIS OF LITHIUM-BEARING MICAS WITH SHORTWAVE AND LONGWAVE INFRARED SPECTROSCOPY

Table 3.1 Mean chemical compositions of studied micas based on electron microprobe analysis of the epoxy mounted handpicked representative mica grains. The number of the analysis to calculate the reported mean (n) are given in the 4th row.

Sampl es	Poly	Lep						Zinn		Side			Musc									Fu c
	LM6	LM7	LM8	LM 10	LM11	LM 20	LM 34	LM 3	LM 32	LM 28	LM 36	LM 38	LM 5	LM 13	LM 14	LM 15	LM 17	LM 22	LM 23	LM 27	LM 37	LM 24
Major and minor elements (reported as wt% of the oxide)																						
n	4	5	6	3	7	3	3	4	3	2	5	4	6	3	2	3	3	3	4	3	4	3
SiO ₂	60.3	51.7	46.8	52.5	47.8	53.4	51.1	47.1	47.1	37.0	34.3	34.9	44.1	46.2	43.1	46.9	46.5	46.3	45.0	45.1	44.9	47.3
TiO ₂	1.76	0.00	0.04	0.00	0.00	0.00	0.23	0.33	0.00	2.47	2.20	4.26	0.01	0.13	0.38	0.72	0.28	0.15	0.72	0.54	0.35	0.44
AlO ₃	11.9	26.7	30.8	26.2	33.8	24.1	23.6	21.4	20.8	20.5	19.7	14.5	37.8	33.7	31.9	37.3	37.8	37.9	32.7	31.8	34.3	32.5
Cr ₂ O ₃	0.00	0.00	0.00	0.00	0.00	0.00	0.00	0.00	0.00	0.00	0.01	0.02	0.00	0.00	0.00	0.00	0.00	0.00	0.01	0.00	0.00	1.29
FeO	1.17	0.01	0.10	0.05	0.04	0.03	0.00	11.5	11.7	20.3	20.3	23.3	0.07	3.71	4.03	0.84	1.50	1.28	4.53	4.99	2.39	1.46
MnO	0.23	0.82	2.20	0.24	0.47	0.45	3.57	0.16	1.38	0.22	0.35	0.3	0.17	0.02	0.00	0.01	0.00	0.03	0.01	0.10	0.07	0.00
MgO	0.01	0.00	0.00	0.00	0.00	0.00	0.00	0.23	0.00	4.36	4.78	8.05	0.00	0.94	0.70	0.75	0.50	0.17	1.35	1.05	0.96	2.27
CaO	0.00	0.00	0.00	0.00	0.00	0.00	0.00	0.00	0.00	0.00	0.00	0.00	0.00	0.00	0.00	0.00	0.00	0.00	0.00	0.00	0.00	0.00
Na ₂ O	0.24	0.26	0.27	0.30	0.37	0.17	0.27	0.19	0.15	0.09	0.15	0.07	0.54	0.46	0.34	0.79	0.88	0.58	0.51	0.59	0.81	0.95
K ₂ O	11.8	9.08	10.1	10.7	9.14	11.3	10.9	10.2	10.3	9.64	9.49	9.53	11.0	10.6	10.5	10.6	10.5	10.9	10.8	10.7	10.4	10.0
Assumed Li₂O concentration (Wt%)																						
Li ₂ O	6.50	6.00	6.00	6.00	6.00	6.00	6.00	3.50	3.50	0.30	0.30	0.16	0.10	0.00	0.00	0.00	0.00	0.00	0.00	0.00	0.00	0.00
Calculated tetrahedral site occupancy based on a 22-oxygen stoichiometry																						
Si	7.98	6.71	6.11	6.78	6.05	6.96	6.74	6.64	6.65	5.64	5.47	5.52	5.95	6.21	6.13	6.06	6.07	6.04	6.11	6.24	5.98	6.29
Al(IV)	0.02	1.28	1.89	1.22	1.95	1.04	1.26	1.36	1.35	2.36	2.53	2.48	2.05	1.79	1.87	1.94	1.93	1.96	1.89	1.76	2.02	1.71
Sum	8.00	8.00	8.00	8.00	8.00	8.00	8.00	8.00	8.00	8.00	8.00	8.00	8.00	8.00	8.00	8.00	8.00	8.00	8.00	8.00	8.00	8.00
Calculated octahedral site occupancy based on a 22-oxygen stoichiometry																						
Al(VI)	1.85	2.81	2.83	2.76	3.08	2.66	2.43	2.20	2.12	1.32	1.18	0.23	3.96	3.54	3.48	3.74	3.78	3.88	3.34	3.41	3.35	3.44
Ti	0.18	0.00	0.00	0.00	0.00	0.00	0.02	0.04	0.00	0.28	0.26	0.51	0.00	0.01	0.04	0.07	0.03	0.01	0.07	0.06	0.03	0.04
Cr	0.00	0.00	0.00	0.00	0.00	0.00	0.00	0.00	0.00	0.00	0.00	0.00	0.00	0.00	0.00	0.00	0.00	0.00	0.00	0.00	0.00	0.10
Fe	0.13	0.00	0.01	0.00	0.00	0.00	0.00	1.36	1.39	2.60	2.71	2.95	0.00	0.42	0.48	0.09	0.16	0.14	0.51	0.58	0.27	0.16
Mn	0.03	0.09	0.25	0.00	0.04	0.00	0.40	0.00	0.16	0.00	0.05	0.02	0.02	0.00	0.00	0.00	0.00	0.00	0.00	0.00	0.00	0.00
Mg	0.00	0.00	0.00	0.00	0.00	0.00	0.00	0.00	0.00	0.99	1.13	1.90	0.00	0.16	0.15	0.14	0.08	0.01	0.27	0.22	0.19	0.45
Li	3.46	3.13	3.14	3.11	3.05	3.14	3.18	1.98	1.99	0.19	0.19	0.10	0.10	0.00	0.00	0.00	0.00	0.00	0.00	0.00	0.00	0.00
Sum	5.64	6.03	6.23	5.87	5.80	6.33	6.91	7.01	5.37	5.53	5.70	4.07	4.13	4.15	4.05	4.05	4.04	4.20	4.26	3.85	4.10	
Octahedral site occupancy based on a 22 cation, 11 oxygen-stoichiometry (used for the graph in figure 3.1)																						
Al(VI)	0.93	1.41	1.42	1.38	1.54	1.33	1.22	1.10	1.06	0.66	0.59	0.12	1.98	1.77	1.74	1.87	1.89	1.94	1.67	1.71	1.68	1.72
Ti	0.09	0.00	0.00	0.00	0.00	0.00	0.01	0.02	0.00	0.14	0.13	0.26	0.00	0.01	0.02	0.04	0.02	0.01	0.04	0.03	0.02	0.02
Cr	0.00	0.00	0.00	0.00	0.00	0.00	0.00	0.00	0.00	0.00	0.00	0.00	0.00	0.00	0.00	0.00	0.00	0.00	0.00	0.00	0.00	0.00
Fe	0.07	0.00	0.01	0.00	0.00	0.00	0.15	0.68	0.70	1.30	1.36	1.48	0.00	0.21	0.24	0.05	0.08	0.07	0.26	0.29	0.14	0.08

SPECTRAL ANALYSIS OF LITHIUM-BEARING MICAS WITH SHORTWAVE AND LONGWAVE INFRARED SPECTROSCOPY

Mn	0.02	0.05	0.13	0.00	0.02	0.00	0.20	0.00	0.08	0.00	0.03	0.01	0.01	0.00	0.00	0.00	0.00	0.00	0.00	0.00	0.00	0.00
Mg	0.00	0.00	0.00	0.00	0.00	0.00	0.00	0.00	0.00	1.50	0.57	0.95	0.00	0.08	0.08	0.07	0.04	0.01	0.14	0.11	0.10	0.23
Li	1.73	1.57	1.57	1.56	1.53	1.57	0.59	0.99	1.00	0.10	0.10	0.05	0.05	0.00	0.00	0.00	0.00	0.00	0.00	0.00	0.00	0.00
Interlayers site occupancy based on a 22-oxygen stoichiometry																						
Mg-Li	-1.73	-1.57	-1.57	-1.56	-1.53	-1.57	-1.59	-0.99	-1.00	0.40	0.47	0.90	-0.05	0.08	0.08	0.07	0.04	0.01	0.14	0.11	0.10	0.23
tFe+	-0.76	-1.37	-1.29	-1.38	-1.52	-1.33	-0.86	-0.40	-0.29	0.78	0.92	1.63	-1.97	-1.56	-1.48	-1.79	-1.80	-1.87	-1.38	-1.39	-1.53	-1.62
Mn+T																						
i-																						
Al(VI)																						
Ca	0.00	0.00	0.00	0.00	0.00	0.00	0.00	0.00	0.00	0.00	0.00	0.00	0.00	0.00	0.00	0.00	0.00	0.00	0.00	0.00	0.00	0.00
Na	0.06	0.06	0.07	0.08	0.09	0.04	0.07	0.05	0.04	0.03	0.04	0.02	0.13	0.12	0.10	0.20	0.22	0.15	0.13	0.16	0.21	0.25
K	2.00	1.50	1.68	1.77	1.47	1.89	1.83	1.85	1.87	1.87	1.93	1.92	1.90	1.83	1.91	1.76	1.76	1.82	1.88	1.57	1.76	1.71
Sum	2.06	1.56	1.75	1.85	1.56	1.93	1.90	1.90	1.91	1.90	1.97	1.94	2.03	1.95	2.01	1.96	1.98	1.97	2.01	1.73	1.97	1.96

Note: Poly=Polyolithionite Lep=Lepidolite Zinn=Zinnwaldite Side= Siderophyllite Musc=Muscovite Fuc = Fuchsite

3.1.1 Classifications of the studied mica minerals

The figure below (*Figure 3.1*) shows the classification scheme of the studied mica minerals. The classification scheme was done based on the parameters Mg-Li (*mgli*) and tFe+Mn+Ti-Al(vi) (*feal*) (Tischendorf et al., 2004), which are based on the occupancy of octahedral site. In the classification diagram, the black circles located at the edge of the outer boundary represent end-member composition micas on the octahedral occupancy in terms of (Mg + tFe + Mn + Ti + Li + Al(vi)) (Tischendorf et al., 2004).

As can be seen in *Figure 3.1*, sample LM 6 is plotted close to the polyolithionite region, which is an endmember of lepidolite mica. This mineral is characterized by the lowest amount of *mgli* near -2 and *feal* close to -1. All the studied samples, LM 7, LM 8, LM 10, LM 11, and LM 20, fall in the lepidolite region and cluster in a limited area. Additionally, the density of the points is higher in the marginal region than in the central portion. The samples are distinguished by *mgli* and *feal* close to -1.5 (*Figure 3.1*). On the other hand, sample LM 34 falls in the lepidolite region, close to polyolithionite mica. The studied samples, LM 3 and LM 32, fall on the circumference of the zinnwaldite boundary. These minerals are characterized by *mgli* = -1 and *feal* close to -0.5.

The studied samples, such as LM 28, LM 36, and LM 38, fall in the siderophyllite region and are characterized by the highest amounts of *mgli* from 0.5 to 1 and *feal* from 0.8 to 1.8. As illustrated in the diagram, the distribution of the points is systematic; for instance, sample LM 38 falls close to the margin of the siderophyllite boundary, while samples LM 28 and LM 36 fall close to the central portion (*Figure 3.1*). This could probably be due to the variations in concentrations of major octahedral cations such as Fe, Al, Mg, and Li. According to Tischendorf et al. (2004), the presence of these four essential cations in the samples, the samples falls more appropriate in the central portion. As compared to sample LM 38, samples LM 28 and LM 36 fall close to the central portion of the siderophyllite region (*Figure 3.1*).

The studied samples, such as LM 15, LM 13, LM 14, LM 17, LM 22, LM 23, LM 27, and LM 37, fall in the muscovite region. The samples are differentiated by *mgli* close to 0 and *feal* close to -1.2. As shown in *Figure 3.1*, the samples are clustered in a relatively large area and depict variations of *mgli* and *feal* content. For instance, samples such as LM 13, LM 37, LM 14, LM 27, and LM 23 fall *mgli* > 0 and *feal* close to -1.2, and samples such as LM 5, LM 22, LM 17, and LM 15 fall *mgli* close to 0 and *feal* < -1.7. Specifically, in sample LM 5, the values of *mgli* < 0 and *feal* < 1.7 are lower than the other muscovite samples. Sample LM 24, which is a variety of muscovite, specifically fuchsite, falls in the muscovite mica region, distinguished by *mgli* close to 0.5 and *feal* close to -1.7.

Therefore, based on their position in the classification diagram consisting of *mgli* and *feal*, the following mica minerals were identified: polyolithionite, lepidolite, zinnwaldite, siderophyllite, and muscovite.

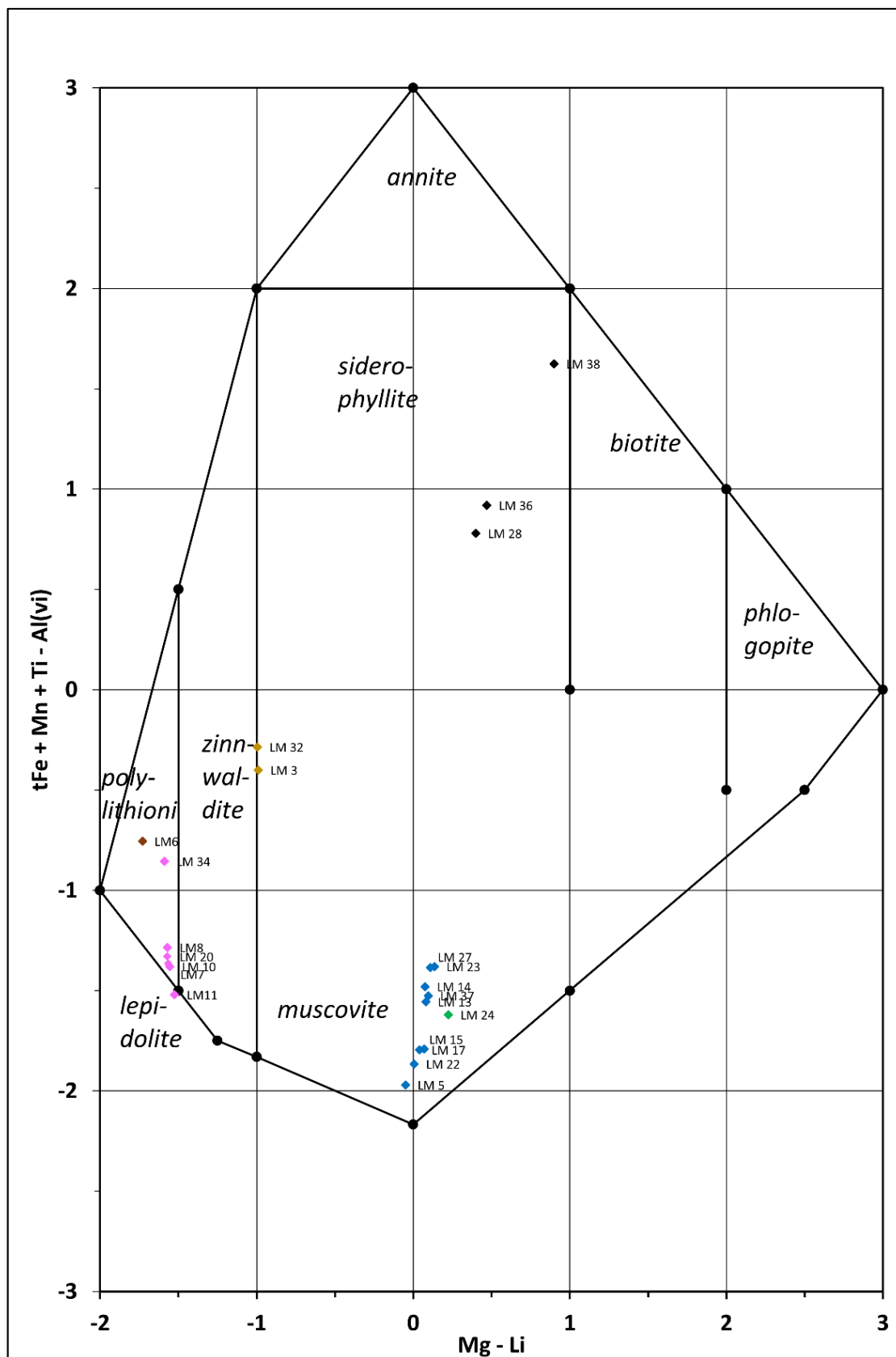


Figure 3.1: Classification of the studied mica minerals plotted in terms of Mg-Li vs. tFe+Mn+Ti-Al(VI) (in a.p.f.u.), as calculated based on 11 oxygen atoms. In this diagram, a.p.f.u. stands for atom per formula unit and tFe represents total iron.

3.2 XRD results

The X-ray diffraction patterns of the studied mica minerals are presented in Figures 3.2 A, B, C, and D. The samples are stacked based on the EMPA Tischendorf classification. All the studied mica minerals, including polyolithionite, lepidolite, zinnwaldite, biotite group, and muscovite, depict similar diffraction patterns in the 5-50 ° 2 θ range, with varying peak heights. The dominant peaks are prominently observed in the 8-10 ° 2 θ , 17-19 ° 2 θ , and 25-27 ° 2 θ ranges.

The polyolithionite and lepidolite mica have the same diffraction patterns and peak heights in the 5-50 ° 2 θ range. They display four sharp peaks in the 8-10 ° 2 θ , 17-19 ° 2 θ , 25-29 ° 2 θ , 35-39 ° 2 θ , and 45-47 ° 2 θ ranges. Besides, they depict one smaller peak in the 35-39 ° 2 θ range. This suggests a similar crystalline structure, atomic arrangement, and chemical composition of the minerals since polyolithionite is an end member of lepidolite mica.

Similarly, the zinnwaldite and siderophyllite mica depict very similar diffraction patterns, peak positions, and peak heights in the 5-50 ° 2 θ range. They exhibit two sharp peaks in the 8-10 ° 2 θ and 25-29 ° 2 θ ranges. Additionally, they depict two smaller peaks in the 35-39 ° 2 θ and 45-47 ° 2 θ ranges. This is also attributed to the similar crystalline structure and atomic arrangement.

Muscovite mica also shows prominent peaks in the 5-50 ° 2 θ range. The mineral depicts two sharp diffraction peaks in the 8-10 ° 2 θ and 25-29 ° 2 θ ranges. Besides, it exhibits three smaller peaks in the 17-19 ° 2 θ , 35-39 ° 2 θ , and 45-47 ° 2 θ ranges. The height of diffraction peaks observed in the 17-19 ° 2 θ decreases towards sample LM 23, which contains low Al and high Mg content. The different patterns of minerals could probably be due to the different arrangements of atoms and chemical compositions of the minerals.

As illustrated in Figure 3.2B, in the 25-29 ° 2 θ ranges, the diffraction peaks display a significant height displacement (shifting the 2 θ peak positions). Additionally, in the 45-47 ° 2 θ ranges, except siderophyllite mica, all studied mica minerals exhibit double diffraction patterns. In Figure 3.2D all the studied mica minerals do not display prominent diffraction peaks.

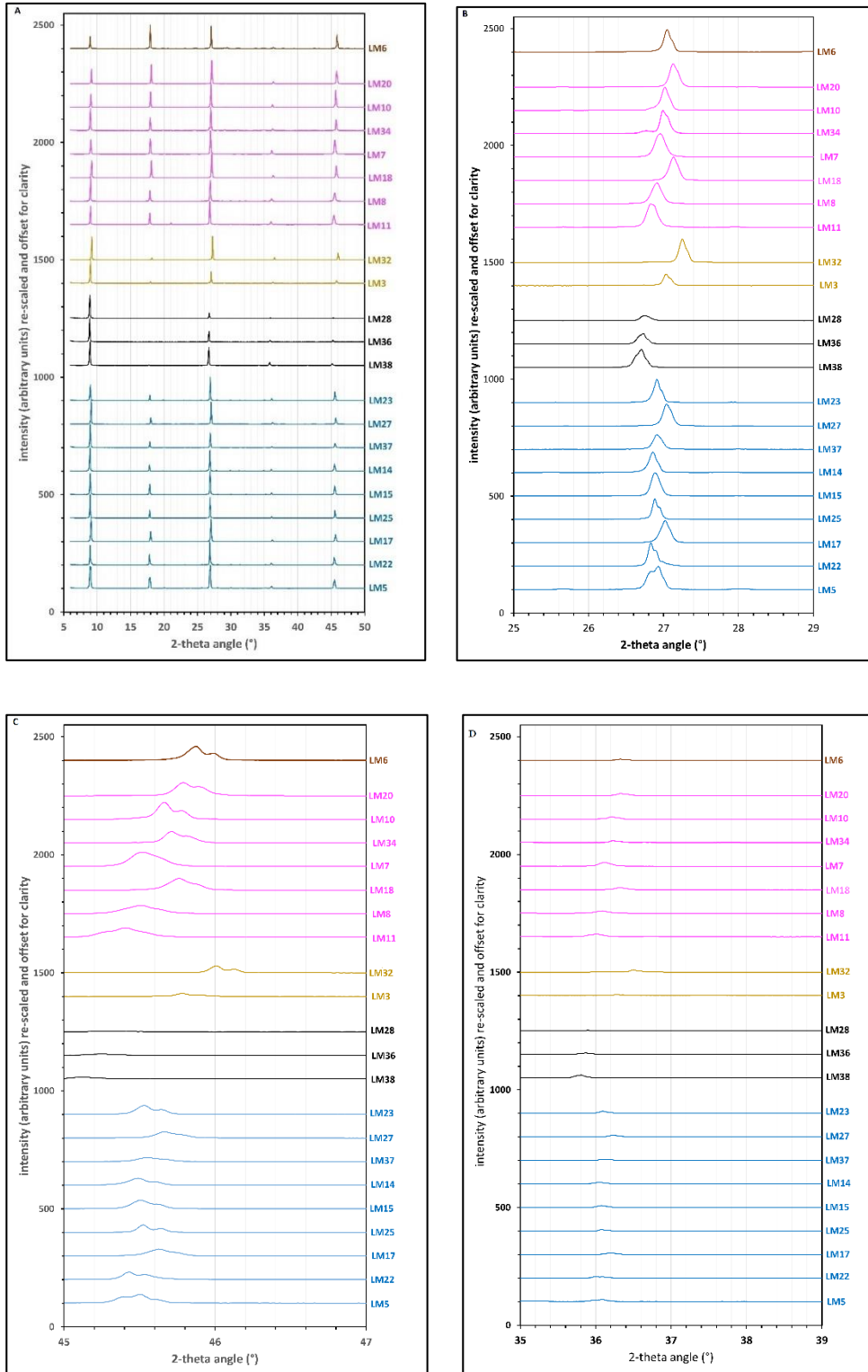


Figure 3.2: X-ray diffraction (XRD) patterns of the studied mica minerals. All the studied mica minerals depict similar diffraction peaks in the 5- 50° 2 θ range (Figure A). The shift of the peaks and peak height difference in the 25-29° 2 θ range (Figure B). Figure C shows the double diffraction peaks of the studied mica minerals. All the studied mica minerals do not have prominent diffraction patterns in the 35- 39° 2 θ (Figure D).

4 LWIR-MWIR RESULTS

This chapter presents the LWIR-MWIR spectral features of the studied mica minerals obtained in the 8000–3700 cm^{-1} range. The chapter consists of two sections: Section 4.1 describes the LWIR-MWIR spectral features of different groups of the studied mica minerals, and Section 4.2 discusses the comparison of the LWIR-MWIR spectral features of the studied trioctahedral types of mica minerals all together.

4.1 LWIR-MWIR spectral features of the studied mica minerals

In the LWIR-MWIR parts of the spectrum, the studied mica minerals display distinct absorption features. To enhance the clarity and better distinguish the absorption features related to bonds involving tetrahedral and octahedral cations in the studied mica minerals, the analysis of the absorption features focused on 700–1100 cm^{-1} for OH-bending vibration and 3500–3800 cm^{-1} for OH-stretching vibration. These specific wavenumber ranges are used to determine and assign the absorption peaks of the bonds involving the major tetrahedral and octahedral cations that constitute the studied mica minerals. Based on their distinct absorption features, six mica minerals were identified. The identified mica minerals include polyolithionite, lepidolite, zinnwaldite, the biotite group, muscovite, and fuchsite. The minerals are ordered based on the assumed increasing Li(VI) content in the octahedral site (Table 3.1).

The spectral features, along with their corresponding band assignments, are described and interpreted in the respective sub-sections below. A summary of the band assignments for all absorption peaks observed in the studied mica minerals is provided in Table 4.1.

4.1.1. Polyolithionite

Polyolithionite, chemically expressed as $\text{K}_2(\text{Li}_4\text{Al}_2)[\text{Si}_8\text{O}_{20}](\text{OH},\text{F})_4$, is grouped under the tri-octahedral types of mica; specifically, it is an end-member of lepidolite mica. The mica from LM 6 is compositionally very close to that of the end member of polyolithionite, as shown in Table 3.1 and Figure 4.1. The tetrahedral sites of the studied polyolithionite sample are occupied by 7.98 Si and 0.02 Al cations per 22 oxygen atoms.

The studied polyolithionite mica depicts distinct spectral features in the 700-1100 cm^{-1} and 3500-3800 cm^{-1} ranges, as illustrated in Figure 4.1. Its distinct spectral features are defined by the double absorption peaks observed at 960 cm^{-1} and 990 cm^{-1} and the two symmetric absorption peaks at 873 cm^{-1} and 1098 cm^{-1} regions (Figure 4.1A). The features observed at 960 cm^{-1} and 990 cm^{-1} are probably due to Si-O in-plane

vibrations (Beran, 2002). On the other hand, the features observed at 873 cm^{-1} and 1098 cm^{-1} are probably due to the presence of Al-O in-plane vibration and Si-O-Si asymmetric stretch bands, based on the studies of Redhammer et al. (2000) and Beran (2002). Additionally, the studied polyolithionite mica exhibits two symmetrical absorption peaks at 787 cm^{-1} and 713 cm^{-1} , which are almost certainly due to Si-O-Si symmetric stretch modes and Li-OH bending vibrations.

In the 3500–3800 cm^{-1} range, the mineral displays two sharp absorption peaks at 3624 cm^{-1} and 3695 cm^{-1} (Figure 4.1B). These features are almost certainly attributed to the presence of Al-Al-Li-OH stretching vibrations (Robert et al., 1989).

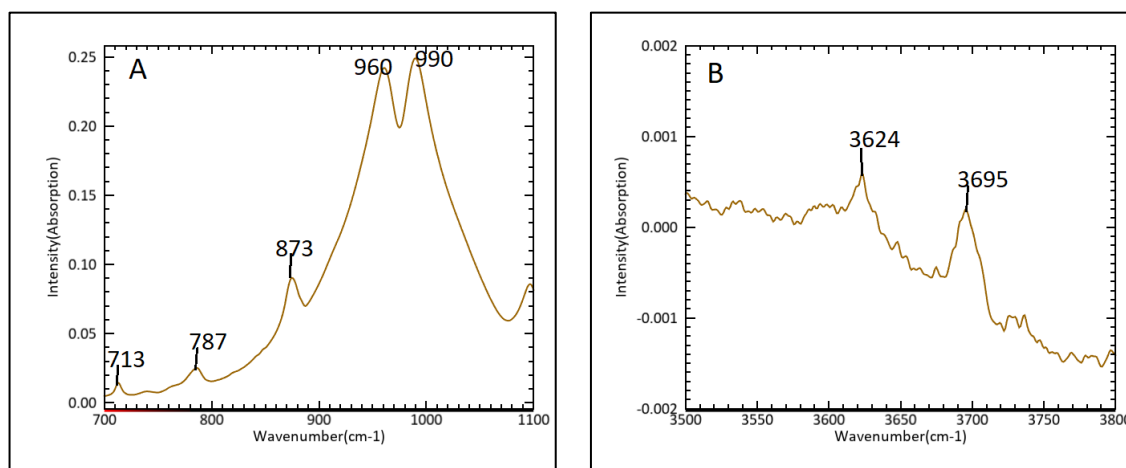


Figure 4.1: LWIR-MWIR spectral features of the studied polyolithionite mica sample (LM 6). Figure A shows the distinct spectral features of the mineral in the OH-bending vibration region, and Figure B depicts the spectral features of the mineral in the OH-stretching vibration region.

4.1.2. Lepidolite mica

Lepidolite, chemically defined as $\text{K}_2(\text{Li,Al})_{5-6}[\text{Si}_{6-7}\text{Al}_{2-1}\text{O}_{20}](\text{OH,F})_4$, is grouped under the trioctahedral types of mica. Table 3.1 shows that the tetrahedral sites of the studied lepidolite mica samples are occupied by 6.05–6.78 Si and 1.04–1.95 Al cations per 22 oxygen atoms.

The dataset consists of six samples, five of which are obtained from single-mineral mica samples and one from a granite rock sample. As can be seen in Figure 4.2, all the studied samples exhibit a wide with multiple overlapping sub-peaks in the 900–999 cm^{-1} range. These features probably due to the presence of Si-O in plane-vibrations (Beran, 2002). Additionally, all the studied samples display multiple absorption peaks in the 829–833 cm^{-1} , 760–798 cm^{-1} , and 745–752 cm^{-1} ranges. These features are probably due to the presence of Al-O-Al in-plane vibrations, Si-O-Si symmetric stretch modes, and Al-O-Si in-plane vibrations, respectively (Jenkins, 1989; Redhammer et al., 2000; Martínez-Alonso et al., 2002). Moreover, sample LM 34 depicts an

absorption peak at 723 cm^{-1} , which is almost certainly due to the presence of Li-OH bending vibrations. This feature is also observed in samples LM 7, LM 8, and LM 10 as a shoulder in their respective spectra (Figure 4.2).

In the $3500\text{--}3800\text{ cm}^{-1}$ wavenumber range, all the analyzed samples display one prominent absorption peak in the $3624\text{--}3699\text{ cm}^{-1}$ range (Figure 4.2B). Additionally, sample LM 11 exhibits an additional absorption peak at 3699 cm^{-1} . These observed features are almost certainly due to the presence of Al-Al-Li-OH stretching vibrations (Robert et al., 1989).

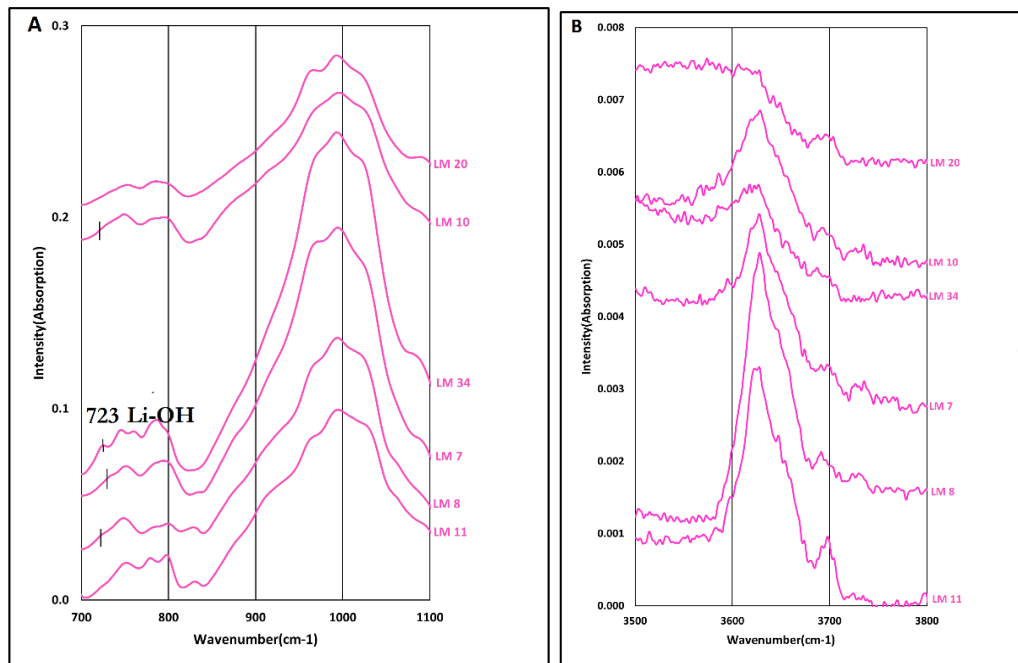


Figure 4.2: LWIR-MWIR spectral features of the studied lepidolite mica samples (offset for clarity). The samples are stacked based on increasing Si(IV) content in the tetrahedral site, as calculated from electron microprobe analysis. Figure A shows the spectral features of the studied lepidolite mica samples in the OH-bending vibration regions, and Figure B depicts the spectral features of the studied lepidolite mica samples in the OH-stretching vibration region.

4.1.3. Zinnwaldite mica

Zinnwaldite, chemical defined as $\text{K}_2(\text{Li, Fe, Al, } \square)_6[(\text{Si, Al})_8\text{O}_{20}](\text{OH, F})_4$, grouped under the trioctahedral types of mica, specifically belongs to the polyolithionite-siderophyllite series and is known as lithium iron mica (Kloprogge et al., 2003; Schneider et al., 2017). Table 3.1 shows that the tetrahedral sites of the studied zinnwaldite mica are occupied by 6.64-6.65 Si and 1.35-1.36 Al per 22 oxygen atoms. The dataset consists of two samples: one (LM 32) from a single-mineral mica sample and the other (LM 3) from a granite rock sample.

In the 800–1000 cm^{-1} range, the two samples show different spectral features (*Figure 4.3A*), despite their chemical similarity. For instance, sample LM 3 from Nanpean Quarry displays a sharp absorption peak at 976 cm^{-1} , while sample LM 32 from Cinovec exhibits broad absorption peaks at 1025 cm^{-1} , along with an additional broad absorption peak at 992 cm^{-1} . These observed features are probably attributed to Si-O in-plane vibrations (Beran, 2002). In addition, both samples depict multiple absorption peaks in the 700–800 cm^{-1} range. However, the multiple absorption peaks observed in LM 3 are relatively sharper compared to LM 32. These features are probably due to the presence of Si-O-Si symmetric stretch modes and Al-O-Si in-plane vibrations (Jenkins, 1989; Martínez-Alonso et al., 2002). Moreover, sample LM 3 depicts an absorption peak at 713 cm^{-1} , which is almost certainly due to the presence of Li-OH bending vibrations.

As illustrated in *Figure 4.3*, in the 3500–3800 cm^{-1} range, the two samples show one prominent, sharp and asymmetric absorption peak at 3621 cm^{-1} . Additionally, LM 3 depicts an additional absorption peak at 3698 cm^{-1} . These observed features are almost certainly due to the presence of Al-Al-Li-OH stretching vibrations (Robert et al., 1989).

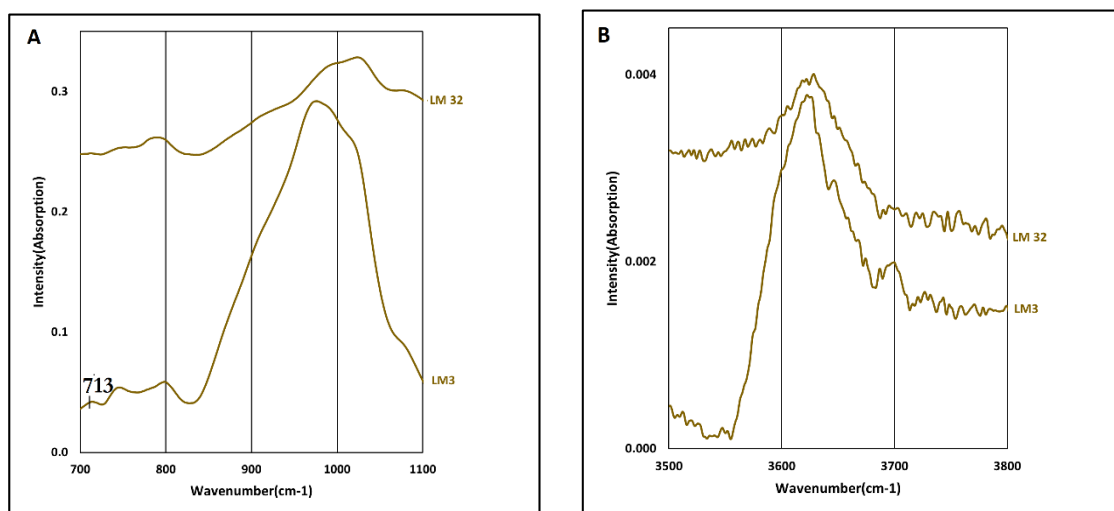


Figure 4.3: LWIR-MWIR spectral features of the studied zinnwaldite mica samples (offset for clarity). Figure A depicts the spectral features of the mineral in the OH-bending vibration region. Figure B displays the sharp and asymmetric absorption peaks of the zinnwaldite mica in the OH-stretching vibration region.

4.1.4. Biotite group mica

The biotite group mica, also known as trioctahedral dark mica, contains four distinct end members, namely, siderophyllite, annite, phlogopite, and eastonite (Sontevska et al., 2008). In the present study, the dataset consists of six samples, two of which were obtained from single-mineral mica samples and four of which were extracted from granite rock samples. Table 3 shows the average electron microprobe analysis of three samples from this group, such as LM 28, LM 36, and LM 38, belonging to the siderophyllite mica, chemically

expressed as $K_2Fe^{2+}_4Al_2[Al_4Si_4O_{20}](OH)_4$. The tetrahedral sites of these samples are occupied by 5.47–5.64 Si and 2.36–2.53 Al per 22 oxygen atoms. The remaining three samples, such as LM 12, LM 16, and LM 35, do not have EMPA data as they were removed during polishing processes. However, their reflection spectra are stacked together with LM 28, LM 36, and LM 38 in Figures 4.4 to analyze and compare their spectral features.

Spectrally, the studied siderophyllite and other biotite group micas are characterized by their highest absorption peak, observed in the 957–993 cm^{-1} range (*Figure 4.4A*). This observed feature is probably due to the presence of Si-O in-plane vibrations (Jenkins, 1989; Redhammer et al., 2000; Beran, 2002). Additionally, except for LM 12, the remaining samples display broad multiple absorption peaks in the 700–800 cm^{-1} range. These features are likely attributed to Si-O-Si symmetric stretch modes and Al-O-Si in-plane vibrations (Jenkins, 1989; Redhammer et al., 2000). Moreover, the studied samples show absorption peaks around the 720 cm^{-1} region, which is almost certainly due to the presence of Li-OH bending vibrations.

In the 3500–3800 cm^{-1} range, the studied samples display distinct variations in absorption peak positions and shapes (*Figure 4.4B*). For instance, sample LM 36 depicts the double, relatively sharp absorption peaks at 3593 cm^{-1} and 3655 cm^{-1} . On the other hand, LM 16 shows a single sharp absorption peak at 3703 cm^{-1} . In contrast, samples LM 28 and LM 35 depict a shoulder centered at 3623 cm^{-1} and 3651 cm^{-1} . These features observed in the 3623–3703 cm^{-1} range are probably due to stretching vibrations of Fe^{2+} - Fe^{2+} - Fe^{2+} -OH, whereas the features observed at 3593 cm^{-1} probably due to the presence of Al^{3+} - Al^{3+} - Fe^{2+} -OH stretching vibrations (Redhammer et al., 2000).

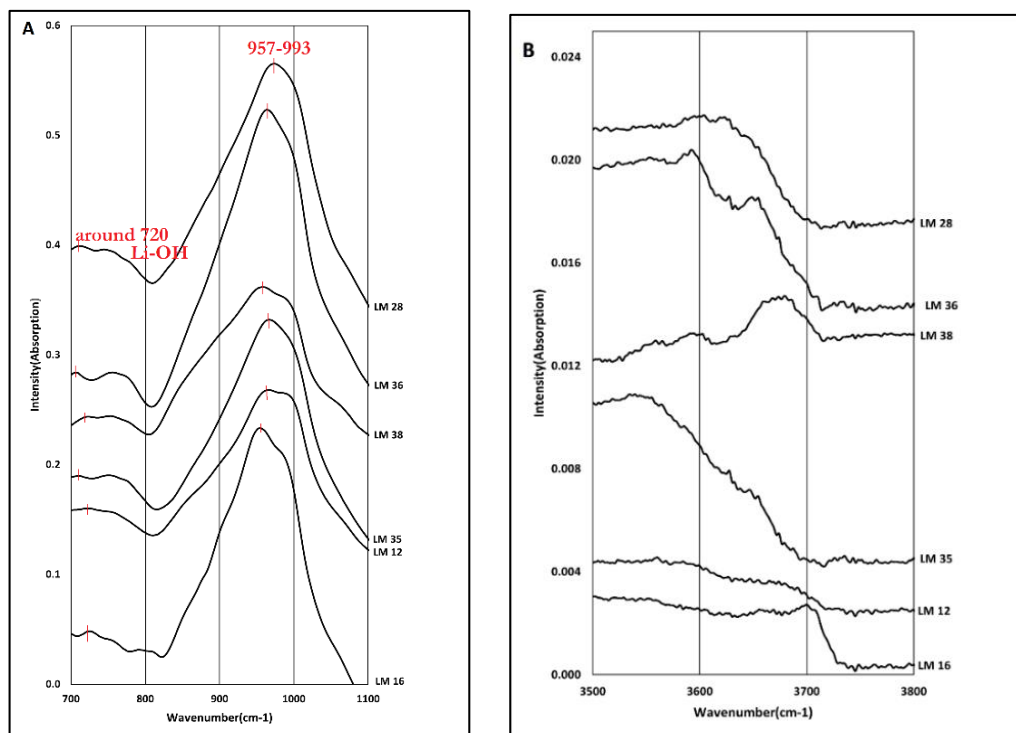


Figure 4.4: LWIR-MWIR spectral features of biotite group mica samples (offset for clarity). Figure A shows the spectral features of the studied biotite group mica, in the OH-bending region. Figure B displays the spectral features of the minerals in the OH-stretching region. The samples such as LM 38, LM 36, and LM 28 are stacked based on increasing Li(VI) content, as estimated from electron microprobe analysis using the major element correlation of MgO.

4.1.5. Muscovite mica

Muscovite, chemically expressed as $K_2Al_4[Si_6Al_2O_{20}](OH,F)_4$, is classified as a dioctahedral type of mica. Table 3.1 shows the tetrahedral sites of the studied muscovite mica samples are occupied by 5.95–6.24 Si and 1.76–2.05 Al per 22 oxygen atoms. The data set consists of ten samples, four of which were obtained from single-mineral mica samples and six from granite and pegmatite rock samples.

Spectrally, the studied muscovite mica is characterized by a sharp and highest absorption peak in the 981–986 cm^{-1} range, along with a broad absorption peak in the 917–928 cm^{-1} range. These observed absorption peaks are almost certainly due to the presence of Si-O-Si symmetric stretch modes and Al-Al-OH bending vibrations. Additionally, the studied samples also display a relatively small, sharp peak in the 822–828 cm^{-1} range and multiple absorption peaks in the 798–802 cm^{-1} and 742–749 cm^{-1} ranges (Figure 4.5A). These absorption peaks are almost certainly due to the presence of Al-Mg-OH bend vibrations, Al-O-Al in-plane vibrations, and Al-O-Si in-plane vibrations, respectively (Beran, 2002; Martínez-Alonso et al., 2002; Singha & Singh, 2016; Cloutier et al., 2021). Moreover, sample LM 5 displays an additional absorption peak at 725 cm^{-1} , which does not appear in the remaining samples. This particular feature is almost certainly due to the presence of Li-OH bending vibrations.

Furthermore, the studied samples also depict sharp and nearly symmetric absorption peak in the 3622–3627 cm^{-1} range. This feature is almost certainly due to the presence of Al-Al-OH stretching vibrations (Besson & Drits, 1997; Martínez-Alonso et al., 2002; Cloutier et al., 2021).

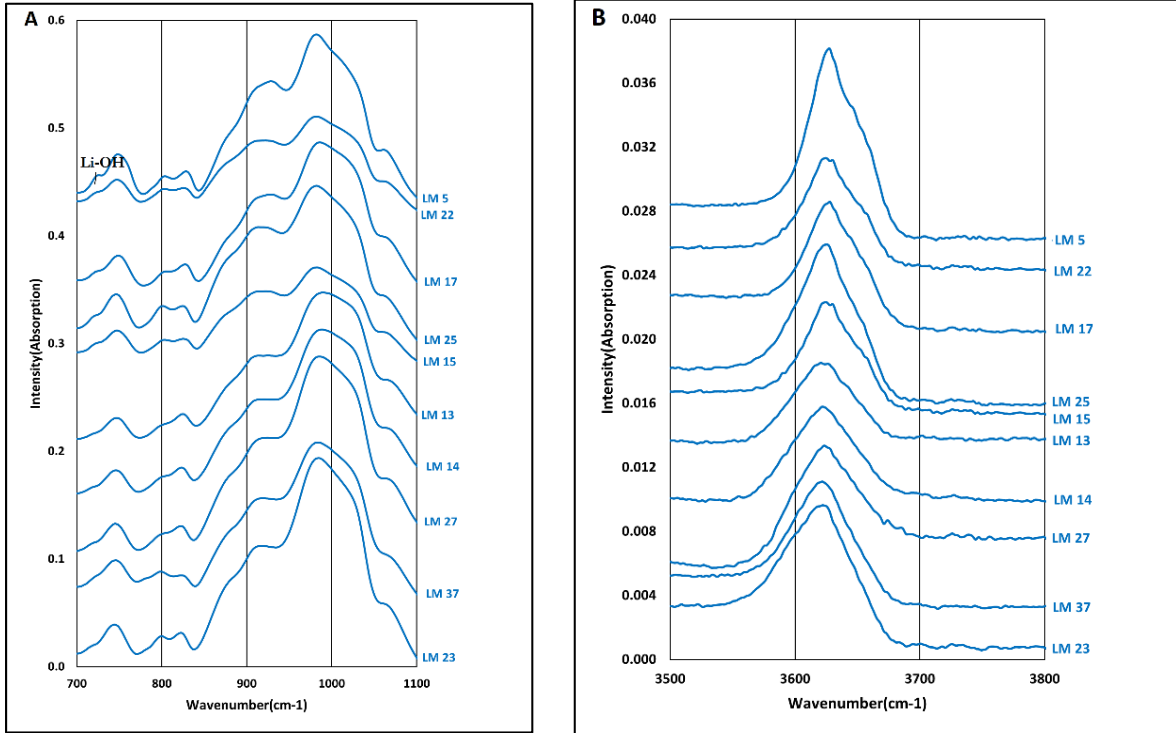


Figure 4.5: LWIR-MWIR spectral features of the studied muscovite mica samples (offset for clarity). Figure A shows the spectral features of the minerals in the OH-bending vibration region, and Figure B depicts the sharp and nearly symmetric absorption peaks of the minerals in the OH-stretching vibration region. The samples are stacked based on increasing Al(VI) content in the octahedral site, as calculated from electron microprobe analysis.

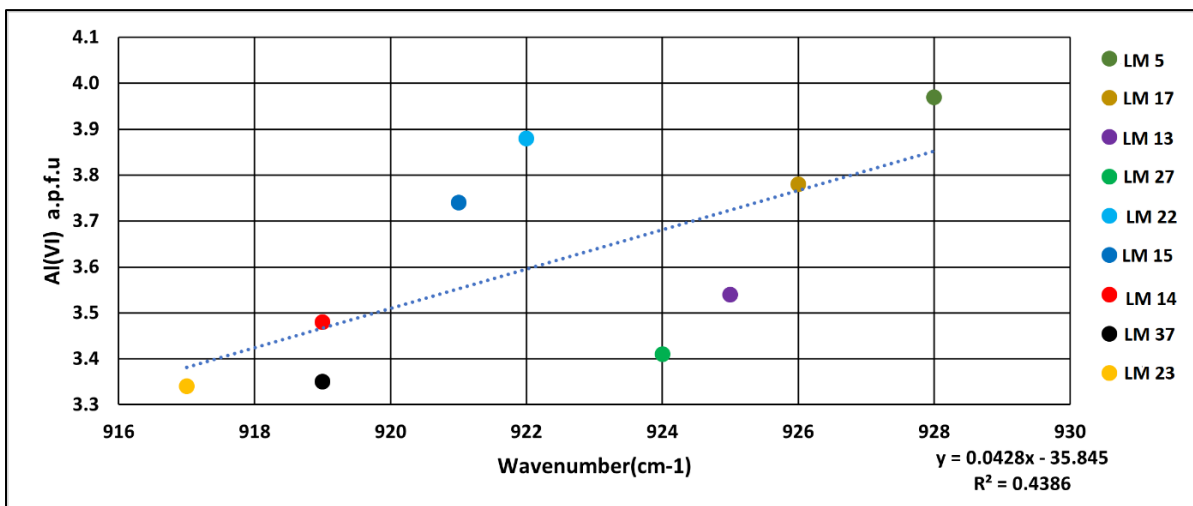


Figure 4.6: Relation between the observed wavenumber position of main cation around 915 cm^{-1} absorption peak in the LWIR reflection spectra of muscovite and their Al octahedral site occupancy calculated from the electron microprobe analysis. Linear regression results and R^2 values are shown at the bottom right.

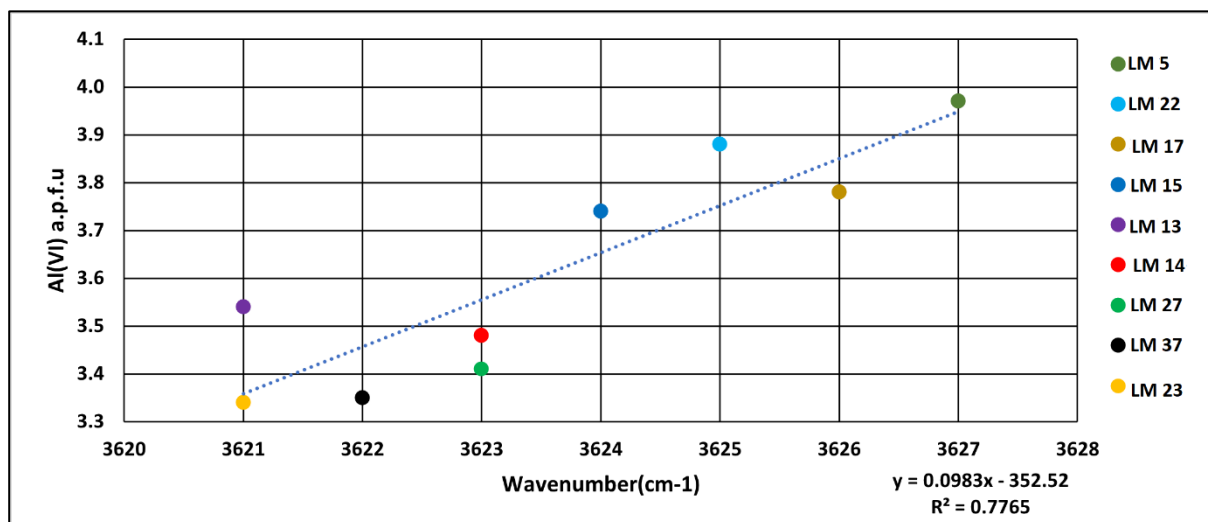


Figure 4.7: Relation between the observed wavenumber position of main cation around 3620 cm⁻¹ absorption peak in the LWIR reflection spectra of muscovite and their Al octahedral site occupancy calculated from the electron microprobe analysis. Linear regression results and R² values are shown at the bottom right.

The figures above (*Figures 5, 6, and 7*) depict the stacked spectra and scatter diagrams plotting the absorption features around the 915 cm⁻¹ and 3620 cm⁻¹ regions against increasing Al(VI) content. The feature shifts towards the higher wavenumber with increasing Al(VI) content in the octahedral site.

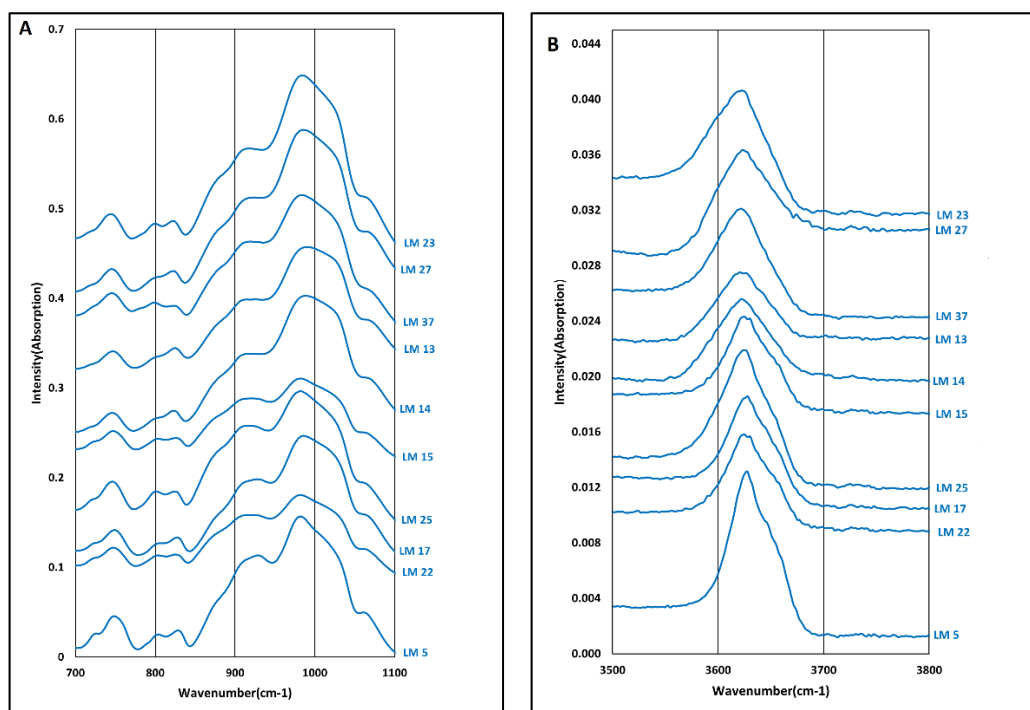


Figure 4.8: LWIR-MWIR spectral features of the studied muscovite mica (offset for clarity). The samples are stacked based on increasing Mg(VI) content in the octahedral site, as calculated from electron microprobe analysis.

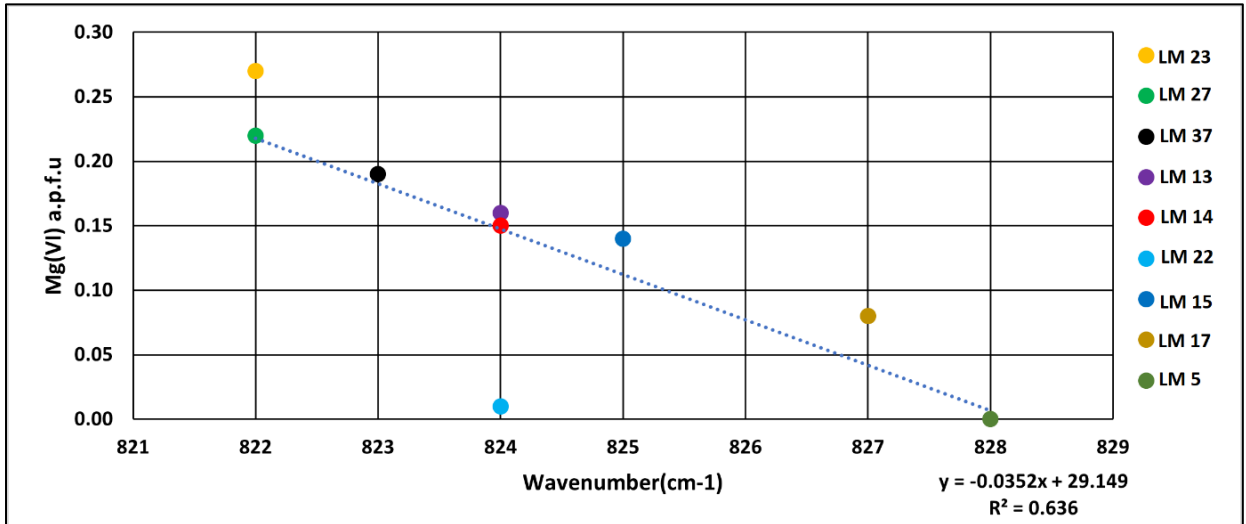


Figure 4.9: Relation between the observed wavenumber position of the main cation around the 820 cm^{-1} absorption peak in the LWIR reflection spectra of muscovite and their Mg octahedral site occupancy, as calculated from the electron microprobe analysis. Linear regression results and R^2 values are shown at the bottom right.

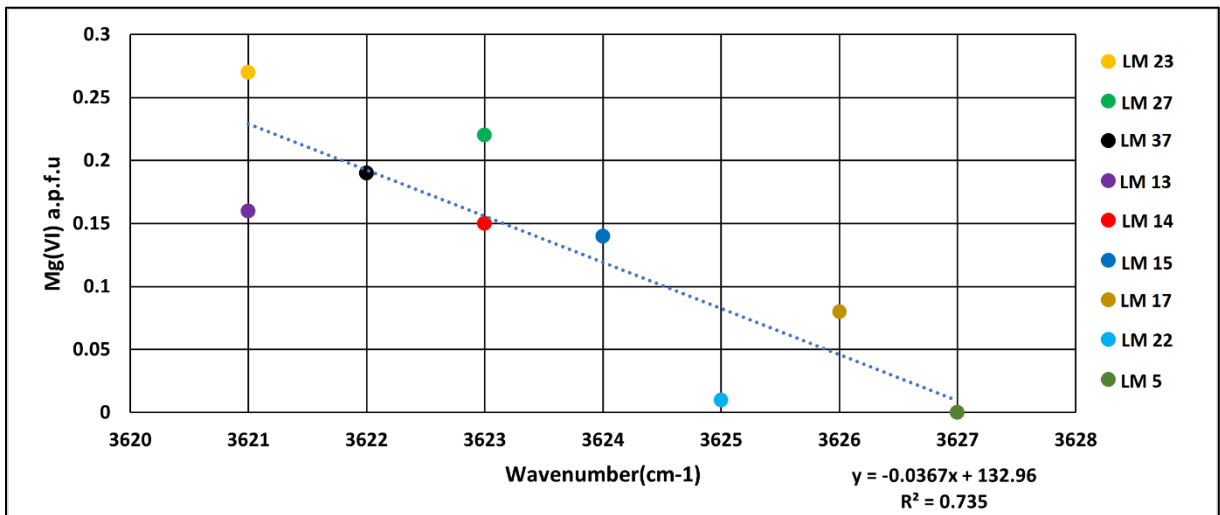


Figure 4.10: Relation between the observed wavenumber position of the main cation around the 3620 cm^{-1} absorption peak in the LWIR reflection spectra of muscovite and their Mg octahedral site occupancy, as calculated from the electron microprobe analysis. Linear regression results and R^2 values are shown at the bottom right.

The figures above (*Figures 8, 9, and 10*) display the stacked spectra and the scatter diagrams plotting absorption features around the 820 cm^{-1} and 3620 cm^{-1} regions. The feature shifts towards the higher wavenumber with decreasing Mg(VI) content in the octahedral site.

4.1.6. Fuchsite mica

Fuchsite, chemically expressed as $K_2(Al\ Cr)_2(Al_2Si_6O_{20})(OH)_4$ also known as green mica, belongs to the dioctahedral type of mica and is characterized by its high chromium concentration. Table 3.1 shows the average electron microprobe analysis of the studied fuchsite mica. The tetrahedral site of this sample is occupied by 6.29 Si and 1.71 Al, and the octahedral site is occupied by 0.1 Cr per 22 oxygen atoms.

The LWIR-MWIR spectral characteristics of fuchsite mica (LM 14) depict notable similarities to those of muscovite mica (e.g., LM 13); both of them depict prominent absorption peaks in the 700–1100 cm^{-1} range. However, the fuchsite mica has a distinct absorption peak at 880 cm^{-1} . This absorption feature is barely recognized in muscovite mica (Figure 4.11). This observed feature (880 cm^{-1}) is probably due to the presence of Al-Cr-OH bending vibrations (Petit et al.,1999). Similarly, in the 3500–3800 cm^{-1} range, both minerals display a sharp and symmetric absorption peak around 3620 cm^{-1} , which is attributed to Al-Al-OH stretching vibrations (Figure 4.11B).

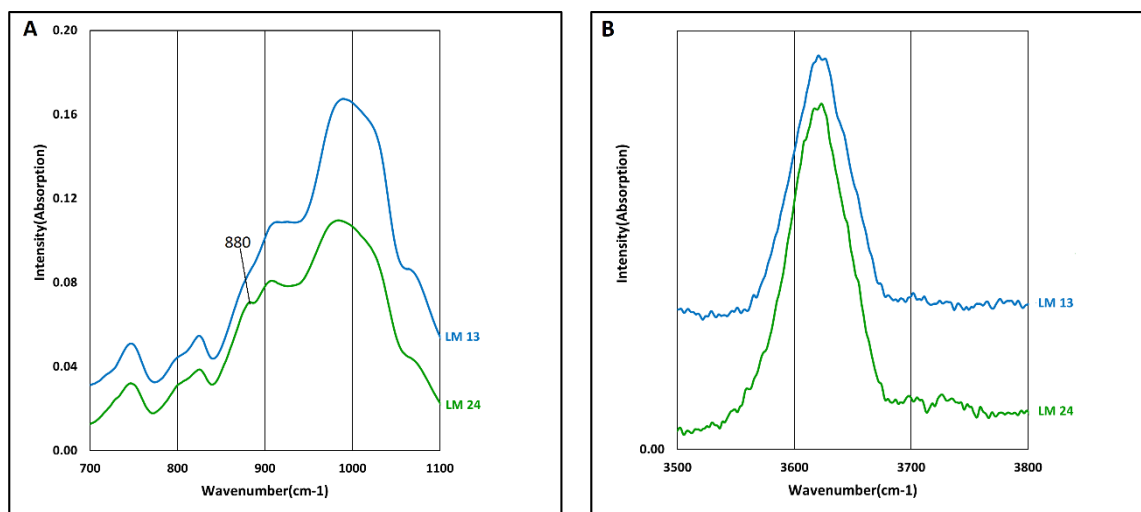


Figure 4.11: LWIR-MWIR spectral features of the studied fuchsite and muscovite mica minerals. Figure A shows the spectral features of the minerals in the OH-bending vibration region and the distinct absorption peaks of fuchsite at 880 cm^{-1} . Figure B depicts the sharp and symmetric absorption peak of the minerals in the OH-stretching vibration region.

4.2 Comparison of the LWIR-MWIR spectral features of the studied trioctahedral types of mica

The figure below shows the absorption features of the studied trioctahedral types of mica in the OH-bending (δ -OH) and OH-stretching (ν -OH) vibration regions. As described in the previous section (Section 4.1), the studied trioctahedral types of mica exhibit distinctive absorption features. However, some studied trioctahedral micas display similarity in their features (e.g., zinnwaldite and siderophyllite mica). Therefore, this section presents a concise summary of the diagnostic features of the studied trioctahedral types of mica minerals to aid in their differentiation. This differentiation may help to build a comprehensive understanding of their mineralogical characteristics. The detailed descriptions, including the band assignments and interpretations of the studied trioctahedral types of micas, are provided in the previous section (section 4.1).

The studied polyolithionite mica displays distinct absorption features, including two double absorption peaks at 960 cm^{-1} and 990 cm^{-1} , along with single absorption peaks at 873 cm^{-1} and 1098 cm^{-1} . Besides, two symmetrical absorption peaks at 785 cm^{-1} and 712 cm^{-1} are observed (*Figure 4.12A*). These unique absorption peaks, which are absent in the other studied trioctahedral types of mica, serve as a distinguishing feature for identifying this particular mineral from other types of the studied trioctahedral types of mica minerals, such as lepidolite, zinnwaldite, and siderophyllite.

Likewise, the studied lepidolite mica also depicts distinctive absorption features, characterized by a wide peak with multiple overlapping sub-peaks in the $900\text{--}999\text{ cm}^{-1}$ range. Specifically, the highest absorption peak observed around 999 cm^{-1} serves as a diagnostic feature of lepidolite mica to distinguish it from polyolithionite, zinnwaldite, and siderophyllite mica minerals (*Figure 4.12A*).

The absorption features of zinnwaldite mica exhibit significant differences from those of polyolithionite and lepidolite mica (*Figure 4.12A*). However, particularly in sample LM 3, it bears a close resemblance to that of siderophyllite mica. Both minerals display the highest peak in the $957\text{--}975\text{ cm}^{-1}$ range and multiple absorption peaks in the $700\text{--}800\text{ cm}^{-1}$ range. Nevertheless, in the zinnwaldite mica (LM 3), the absorption peaks observed at 797 cm^{-1} and 744 cm^{-1} are sharper than the siderophyllite mica observed in the $773\text{--}780\text{ cm}^{-1}$ and $747\text{--}754\text{ cm}^{-1}$ ranges. These distinguishing features allow the studied zinnwaldite mica (LM 3) to be distinguished from the studied siderophyllite mica. Additionally, the highest absorption peaks observed at 971 cm^{-1} and 993 cm^{-1} help to distinguish zinnwaldite from the studied polyolithionite and lepidolite mica.

Similarly, the studied siderophyllite mica depicts the highest absorption peak, observed in the $957\text{--}993\text{ cm}^{-1}$ range, and multiple broad absorption peaks in the $700\text{--}800\text{ cm}^{-1}$ range. These distinguishing features allow us to differentiate siderophyllite mica from the studied polyolithionite and lepidolite mica. Moreover, the presence of multiple broad absorption peaks aids in distinguishing siderophyllite from zinnwaldite mica (LM 3).

In the 3500–3800 cm^{-1} region, as shown in Figure 4.12B, the studied polyolithionite, lepidolite, and zinnwaldite micas show similar spectral features, which are defined by relatively sharp and asymmetric absorption peaks around the 3620 cm^{-1} region. As a result, distinguishing among them in this region is challenging. On the other hand, the absorption features of siderophyllite mica are different from those of the other trioctahedral micas (Figure 4.12B). It depicts broad, double, and shoulder-centered absorption features. Additionally, except for siderophyllite mica, all the studied mica minerals don't have an absorption peak around the 3590 cm^{-1} region. As a result, based on the distinct shape of these features, it is possible to differentiate siderophyllite from the other studied trioctahedral types of mica.

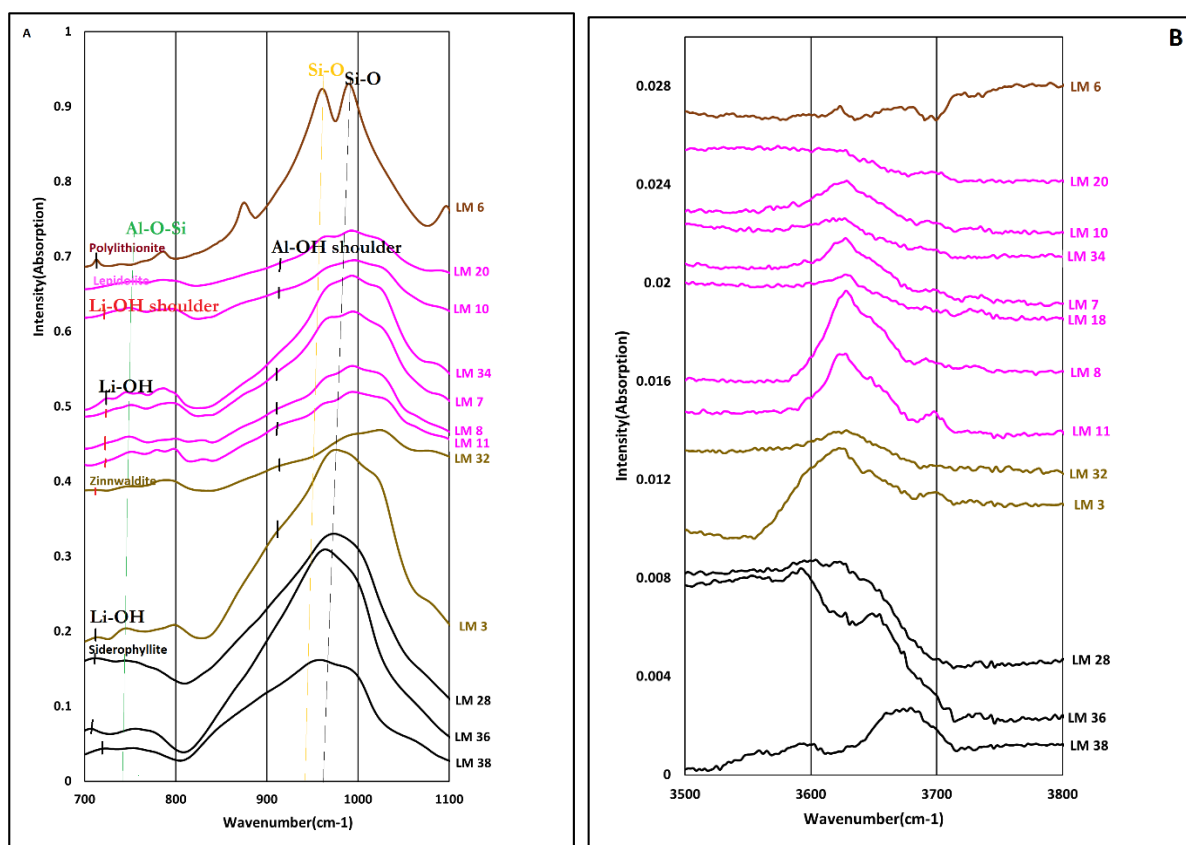


Figure 4.12: LWIR-MWIR spectral features of the studied trioctahedral types of mica. The samples are stacked based on the assumed increasing Li(VI) content in the octahedral site. Figure A depicts the distinct absorption features of the studied trioctahedral mica in the OH-bending vibration region. Figure B displays the absorption features of the studied trioctahedral types of mica in the OH-stretching region.

Table 4.1 Assignments of OH bands (cm⁻¹) of the studied mica minerals

Trioctahedral types of the mica											
Cations	δ-OH							ν-OH			
	Si-O	Si-O		Al-O	Al-O-Al	Si-O-Si	Al-O-Si	Li-OH	Al-Al-Li-OH	Al-Al-Li-OH	
Polyolithionite mica											
LM 6	990	960	-	874	-	785	-	712	3698	3621	-
Lepidolite mica											
LM 7	994	971	-	-	833	793	751	-	-	3627	-
LM 8	993	968	-	-	829	798	748	-	-	3626	-
LM 10	996	971	-	-	831	793	749	-	-	3625	-
LM 11	994	964	-	-	830	797,778	751	-	3699	3624	-
LM 18	999	976	-	-	-	791	752	-	-	3629	-
LM 20	993	967	-	-	-	786	752	-	3697	-	-
LM 34	993	970	-	-	-	787,760	745	724	-	3626	-
Zinnwaldite mica											
LM 3	975	-	-	-	-	798	744	713	3698	3625	-
LM 32	993	-	-	-	-	795	745	-	-	3621	-
Biotite group mica											
Cations	Si-O	Si-O				Si-O-Si	Al-O-Si	Li-OH	Fe ²⁺ -Fe ²⁺ -Fe ²⁺ -OH	Fe ²⁺ -Fe ²⁺ -Fe ³⁺ -OH	Al ³⁺ -Al ³⁺ -Fe ²⁺ -OH
LM 12	993	964	-	-	-	-	-	-	-	-	-
LM 16	985	987	-	-	-	807,791	759	725	3707	-	-
LM 28	974	-	-	-	-	780	747	710	-	3624	-
LM 35	965	-	-	-	-	776	746	-	3651	-	-
LM 36	966	-	-	-	-	773	748	706	3656	-	3593
LM 38	991	957	-	-	-	778	754	724	3675	-	3591
Diocahedral types of mica (Muscovite and Fuchsite)											
	Si-O-Si		Al-Al-OH	Al-Fe-OH	Al-Mg-OH	Al-O-Al	Al-O-Si	Li-OH		Al-Al-OH	
LM 5	981	-	928	-	828	802	749	725	-	3627	-
LM 13	986	-	925	-	824	801	746	-	-	3621	-
LM 14	988	-	919	-	824	801	744	-	-	3623	-
LM 15	981	-	921	-	825	799	748	-	-	3624	-
LM 17	987	-	926	-	827	801	749	-	-	3626	-
LM 22	984	-	922	-	824	801	748	-	-	3625	-
LM 23	984	-	917	-	822	799	742	-	-	3622	-
LM 25	979	-	913	-	825	800	746	-	-	3626	-
LM 27	984	-	924	-	822	798	744	-	-	3623	-
LM 37	982	-	919	-	823	798	745	-	-	3622	-
LM 24	981	-	907	882	824	802	746	-	-	3621	-

Note: In this study, the band assignment of the absorption peaks of OH-bending and OH-stretching vibrations was adopted from previous studies. However, it should be noted that for the trioctahedral types of mica such as polyolithionite, lepidolite, and zinnwaldite, there is a lack of previous studies, especially for the band assignments in the OH-bending region. Therefore, for assigning the bands for these minerals, this study used band assignments from previous studies of biotite group mica (Jenkins, 1989; Redhammer et al., 2000; Beran, 2002) and muscovite mica adopted from (Besson & Drits, 1997; Beran, 2002; Martínez-Alonso et al., 2002; Zviagina et al., 2020; Cloutier et al., 2021).

5 VNIR-SWIR RESULTS

This chapter presents the VNIR-SWIR spectral characteristics of the studied mica minerals obtained in the 350–2500 nm wavelength range. The chapter consists of three sections: Section 5.1 provides the VNIR-SWIR spectral characteristics of different groups of the studied mica minerals; Section 5.2 presents a collective comparison of the VNIR-SWIR spectral characteristics of the studied trioctahedral micas; and Section 5.3 describes a comparison of the VNIR-SWIR spectral characteristics of the studied lepidolite and muscovite mica minerals. The section below (Section 5.1) provides a detailed description and interpretation, including the band assignments of the spectral features observed in the studied mica minerals. A summarized band assignment of the spectral characteristics of all the studied mica minerals can be found in Table 5.1.

5.1 VNIR-SWIR spectral characteristics of the studied mica minerals

5.1.1. Polyolithionite mica

In the SWIR (1300–2500 nm) region, the studied polyolithionite mica exhibits prominent absorption features (*Figure 5.1*). Notably, it displays the first deepest, narrowest, and most symmetrical absorption feature at 2200 nm. This feature is associated with the interaction of OH with Al bonds in the structure of minerals and is commonly known as the Al-OH feature (Cardoso-Fernandes et al., 2021; Li et al., 2021). Additionally, at 1410 nm, the mineral has the second-deepest, narrowest, and most symmetrical absorption feature. This feature is almost certainly attributed to vibration bonds between OH and H₂O molecules in the mineral structure (Hunt, 1970; Clark et al., 1990). The third deepest absorption feature observed at 1912 nm appears slightly shallower and broader compared to the first and second deepest absorption features, which can be associated with the presence of a vibration bond in the H₂O molecule. Moreover, the mineral exhibits a shallow and broad absorption feature at 2349 nm and 2443 nm (*Figure 5.1B*). These features are almost certainly due to the presence of secondary Al-OH vibration bonds (Cardoso-Fernandes et al., 2021).

Furthermore, in the VNIR (400–1300 nm) region, the studied polyolithionite mica exhibits shallow and broad absorption features at 450 nm, 542 nm, and 790 nm (*Figure 5.1*). The presence of relatively high Ti (0.18), Fe (0.13), and Mn (0.03) content in the octahedral site, as illustrated in Table 3.1, suggests these features are almost certainly attributed to the electronic processes of transition metals such as Ti, Mn, and Fe.

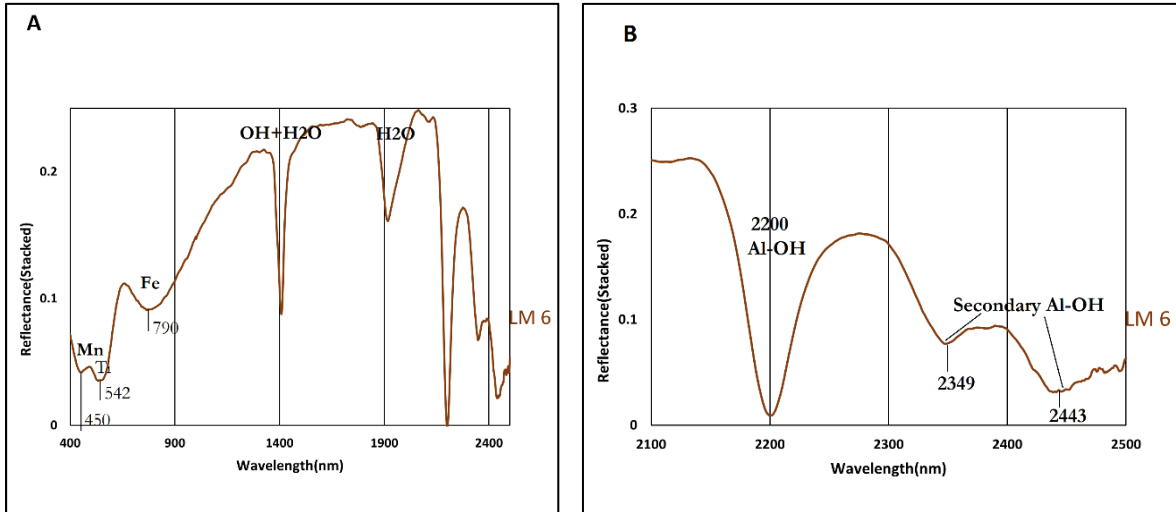


Figure 5.1: VNIR-SWIR spectral characteristics of the studied polyolithionite mica (LM 6) in the 400–2500 nm range illustrated Figure A. Figure B depicts the spectral features of the studied polyolithionite mica in the 2100–2500 nm range, specifically shows the precise wavelength position of the main octahedral cation, Al(VI).

5.1.2. Lepidolite mica

In the SWIR region, the studied lepidolite mica also exhibits prominent absorption features (*Figure 5.2A*). It depicts the first deepest, narrowest, and symmetrical absorption feature around 2200 nm, which is attributed to the presence of an Al-OH vibration bond. As observed in *Figure 5.2 B*, due to varying concentrations of Al(VI), all the studied samples display different positions of the first deepest absorption feature. The majority of the samples depict features in the 2200–2208 nm range. In contrast, two samples, specifically LM 8 and LM 11, exhibit the feature at 2196 nm and 2197 nm, respectively. Additionally, the features shift systematically towards the shorter wavelength with increasing Al(VI) content in the octahedral site, resulting in a spectral shift of 12 nm (*Figure 5.2B*). Similarly, the depth of the Al-OH feature also increases with increasing Al(VI) content.

Additionally, the studied samples exhibit the second deepest and most symmetrical absorption feature in the 1408–1410 nm range, which is likely attributed to the presence of vibration bonds of OH and H₂O molecules. Moreover, the studied samples display shallow and broad absorption features in the 1907–1917 nm, 2342–2355 nm, and 2438–2452 nm ranges, respectively. These features are almost certainly associated with the presence of vibration bonds in the H₂O molecule and secondary Al-OH vibration bonds (Clark, 1999; Bishop et al., 2008; Cardoso-Fernandes et al., 2021).

In the VNIR part of the spectrum, all studied samples also display prominent absorption features in the 449–564 nm range. As indicated in Table 2, with the exception of two samples (LM 10 and LM 20), the remaining samples contain relatively high Mn(VI) content in the octahedral site, ranging from 0.04–0.40,

suggesting these absorption features are primarily attributed to the electronic processes of transition metal ions of Mn. Additionally, the presence of Mn contributes to the pink color of lepidolite mica, which arises from the absorption of green around 560 nm and blue light around 450 nm and allows the reflection of red light around 620 nm. On the other hand, the absorption features observed in samples LM 10 and LM 20 could possibly be due to the effects of other transition metals or impurities.

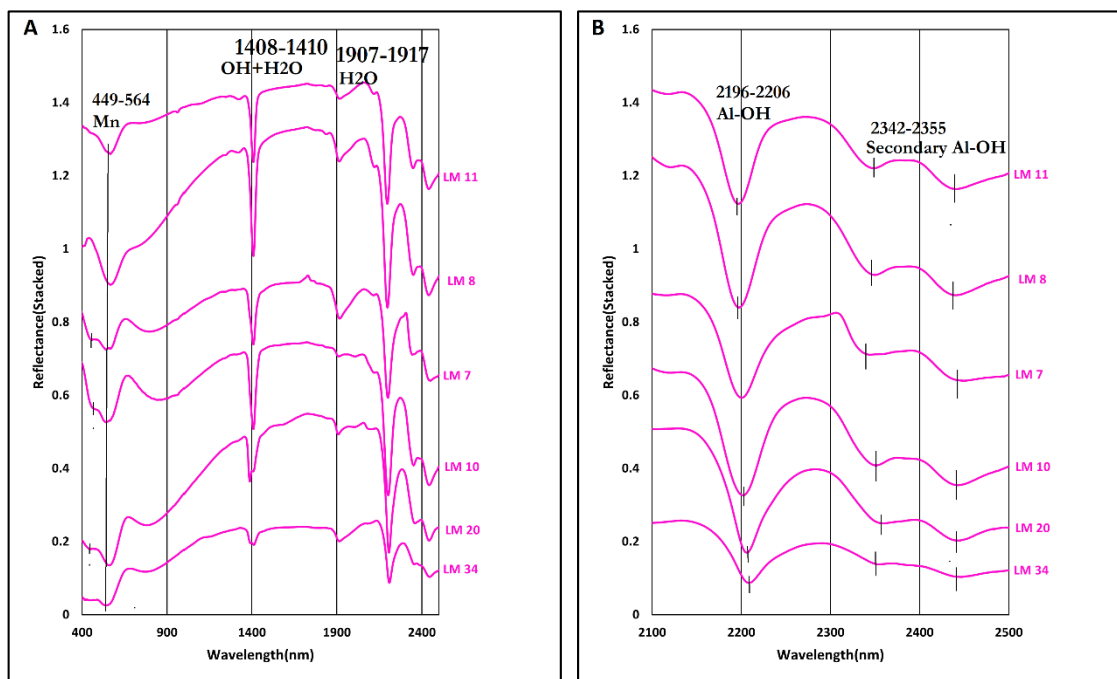


Figure 5.2: VNIR-SWIR spectral characteristics of the studied lepidolite mica samples in the 400–2500 nm range (offset for clarity). The samples are stacked based on increasing Al(VI) content in the octahedral site, as calculated from electron microprobe analysis (Figure A). Figure B depicts the absorption features of lepidolite mica in the 2100–2500 nm range, which shows the shift of the absorption features mainly around 2200 nm.

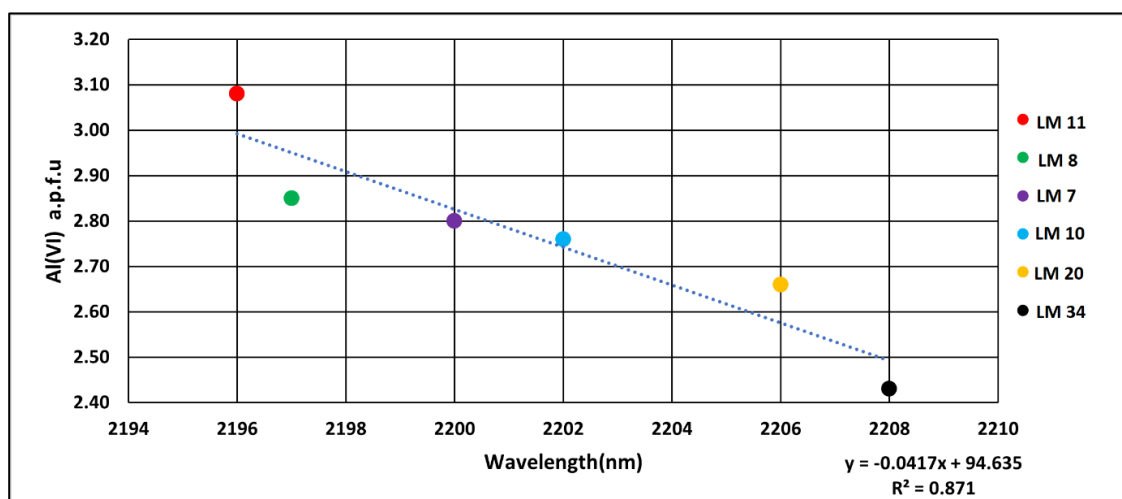


Figure 5.3: Relation between the observed wavelength position of the main cation around 2200 nm absorption minimum in the reflection spectra of lepidolites and their Al octahedral site occupancy calculated from the electron probe microanalysis based on 22 oxygen atoms, a total of 6 cations in this site based on this stoichiometry, Al(VI) means Al with a 6- fold coordination. Linear regression results and R^2 values are shown at the bottom right.

The Figure above (*Figure 5.3*) shows a scatter diagram plotting the 2200 nm feature against the content of Al(VI) in the octahedral site. The trend shows negative correlations between Al(VI) content and the 2200 nm feature. The 2200 nm feature shifts towards the shorter wavelength with increasing Al(VI) content in the octahedral site.

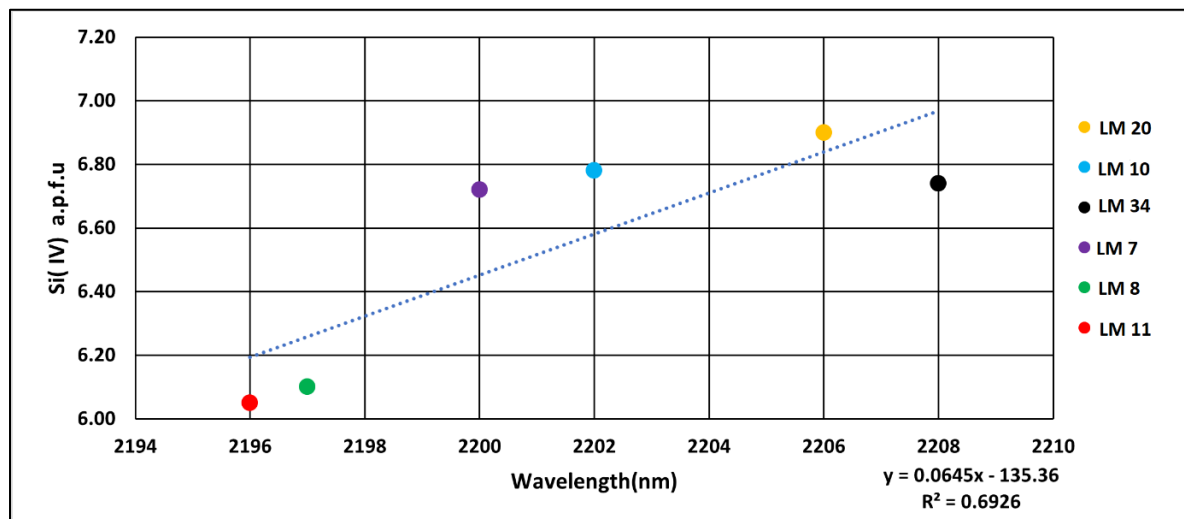


Figure 5.4: Relation between the observed wavelength position of the main cation-around 2200 nm absorption minimum in the reflection spectra of lepidolites and their Si tetrahedral site occupancy calculated from the electron microprobe analysis. Atoms per formula unit (a.p.f.u) based on 22 oxygen stoichiometry, so the maximum site occupancy of the tetrahedral site is 8 and only Si(VI) and Al(VI) are assumed to occupy the tetrahedral site. Linear regression results and R^2 values shown at bottom right.

A positive correlation trend is observed when the 2200 nm feature is plotted against Si(IV) content in the tetrahedral site. The feature is shifted to a higher wavelength with increasing Si(IV) content in the tetrahedral site. This is probably due to the potential substitution of Al(IV) by Si(IV) in the tetrahedral site.

5.1.3. Zinnwaldite mica

The studied zinnwaldite mica displays distinct absorption features in the 400–2500 nm range. Specifically, it exhibits deep and asymmetric absorption features at 2248 nm and 2253 nm. Notably, in the case of sample LM 32, the depth of this feature is deeper than that of LM 3. This difference is likely due to the high content of Fe(VI) in sample LM 32, as illustrated in Table 3.1. This observed feature is almost certainly due to the presence of Fe-OH vibration bonds in the crystal structure of the mineral (Clark et al., 1990; Cardoso-Fernandes et al., 2021).

Additionally, the studied samples display relatively shallow absorption features at 2218 nm and 2205 nm, which is attributed to the presence of Al-OH vibration bond. As can be seen in *Figure 5.4B*, this feature is shifted towards a higher wavelength with increasing Al(VI) content in the octahedral site. In contrast, an

opposite trend is observed in the case of lepidolite mica: the feature shifts towards the shorter wavelength position with increasing Al(VI) content. The observed shift in the case of zinnwaldite is probably due to the influence of other cations. As illustrated in Table 3.1, sample LM 3 contains a relatively high content of Ti (0.04); consequently, the presence of Ti(VI) in the octahedral site could contribute to the shift towards the higher wavelength position.

Moreover, due to the presence of a vibration bond in the H₂O molecule, a distinct shallow and symmetric absorption feature is observed at 1920 nm and 1908 nm. Likewise, the samples exhibit broad and shallow absorption features in the 2357–2449 nm range. These features are almost certainly due to the presence of secondary Al-OH vibration bond (Cardoso-Fernandes et al., 2021).

In the VNIR part of the spectrum, the studied zinnwaldite samples display distinct deep and symmetric absorption features at 896 nm, 897 nm, and 1200 nm. As observed in Table 3.1, the studied zinnwaldite samples contain a relatively high content of Fe(VI) (1.36 and 1.39). The presence of a high content of Fe suggests that these features are almost certainly associated with the electronic processes of transition metals of Fe incorporated into the crystal structure of the mineral.

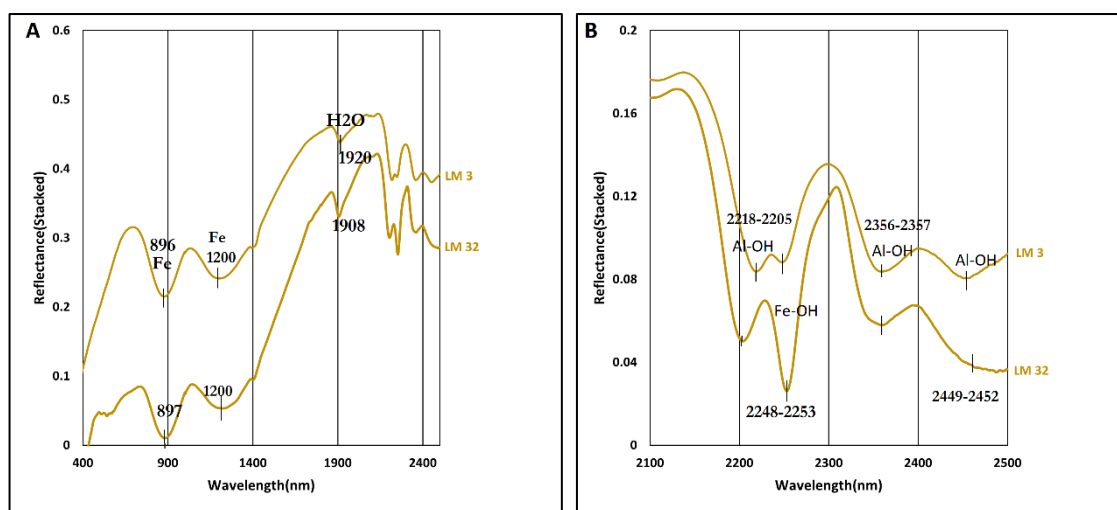


Figure 5.5: VNIR-SWIR spectral characteristics of the studied zinnwaldite mica samples (Figure A). The samples are stacked based on increasing Al(VI) content in the octahedral site, as calculated from electron microprobe analysis. Figure B shows the 2100–2500 nm spectral features of zinnwaldite formed as a result of octahedral cations, such as Al(VI) and Fe(VI).

5.1.4. Biotite group mica

As described in the previous section (*section 4.1.4*), the data set consists of six samples, namely LM 12, LM 16, LM 28, LM 35, LMM 36, and LM 38. Among the six samples, LM 12, LM 16, and LM 35 don't have EMPA data; however, they were stacked together with the other samples to analyze the spectral characteristics collectively.

In the SWIR part of the spectrum, the studied biotite group mica, displays distinct absorption features (*Figure 5.6*). Except for samples LM 35 and 36, which exhibit shallow absorption features at 1403 nm, 1914 nm, 1396 nm, and 1926 nm, respectively, the remaining samples do not have absorption features in these wavelength ranges. Additionally, samples LM 28 and LM 35 depict a shallow absorption feature at 2205 nm and 2212 nm, which is probably due to the mixture of muscovite mica during picking processes.

Moreover, all the studied samples exhibit absorption features in the 2248–2257 nm range. This feature is almost certainly associated with the presence of the Fe-OH vibration bond (Clark et al., 1999; Bishop et al., 2008). Additionally, all the studied samples exhibit absorption features in the 2335–2395 nm range, attributed to the Mg-OH vibration bond. In the figures below (*Figures 5.7 and 5.8*), the studied samples are stacked based on increasing Fe(VI) and Mg(VI) content, depicting a systematic shift toward the shorter wavelength with increasing Fe(VI) and Mg(VI) content in the octahedral site. This shift is almost certainly due to Tschermak's substitution of $\text{Al}^{3+}_{(IV)} + \text{Al}^{3+}_{(VI)} \leftrightarrow \text{Si}^{4+}_{(IV)} + \text{Mg}^{2+}_{(VI)}$ or $\text{Fe}^{2+}_{(VI)}$ (Lypaczewski & Rivard, 2018).

In the VNIR part of the spectrum, all the studied samples display broad and shallow absorption features in the 908–913 nm range. Additionally, samples LM 12, LM 16, and LM 38 show additional shallow and broad absorption features at 724 nm. As illustrated in Table 2, the studied samples from this group contain high Fe(VI) content, ranging from 2.60-2.95. The presence of a high content of Fe(VI) suggests these features are almost certainly attributed to the electronic process of transition metals such as Fe in the crystal structure of the minerals (Hunt, 1977; Clark et al., 1990).

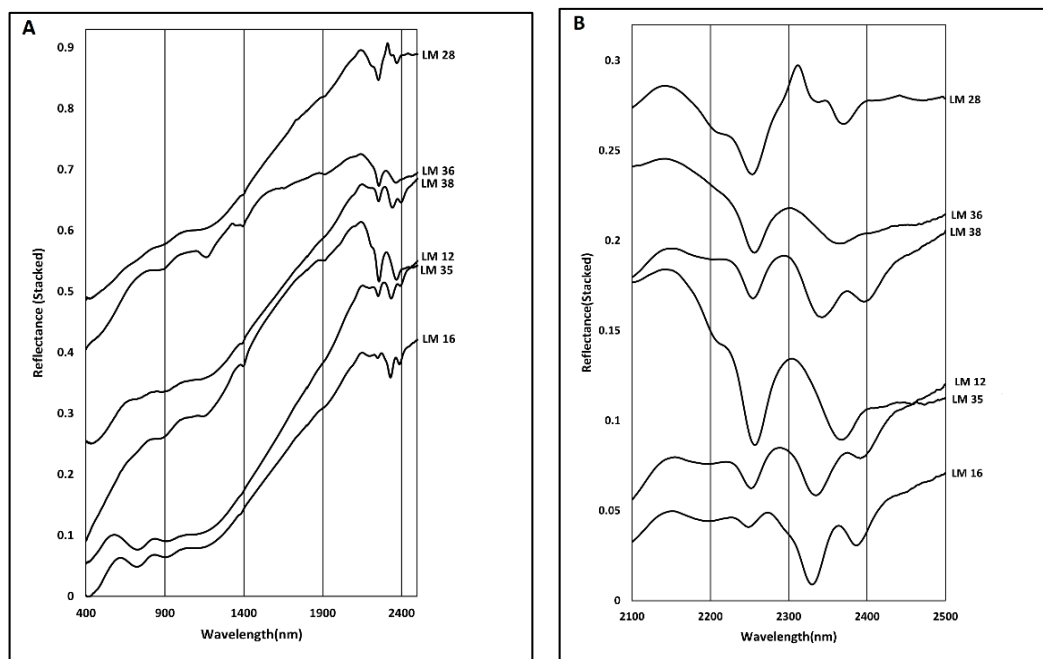


Figure 5.6: VNIR-SWIR spectral characteristics of the studied biotite group mica samples. Figure A illustrates the spectra feature of biotite group mica in the 400–2500 nm range. Figure B presents the spectral features of biotite group mica in the 2100–2500 nm range to show the precise wavelength positions of the absorption features formed due to the main cations, such as Fe and Mg. Samples such as LM 38, LM 36, and LM 28 were stacked based on increasing Li(VI) content in the octahedral site, as estimated by EMPA using Mg(VI) correlations.

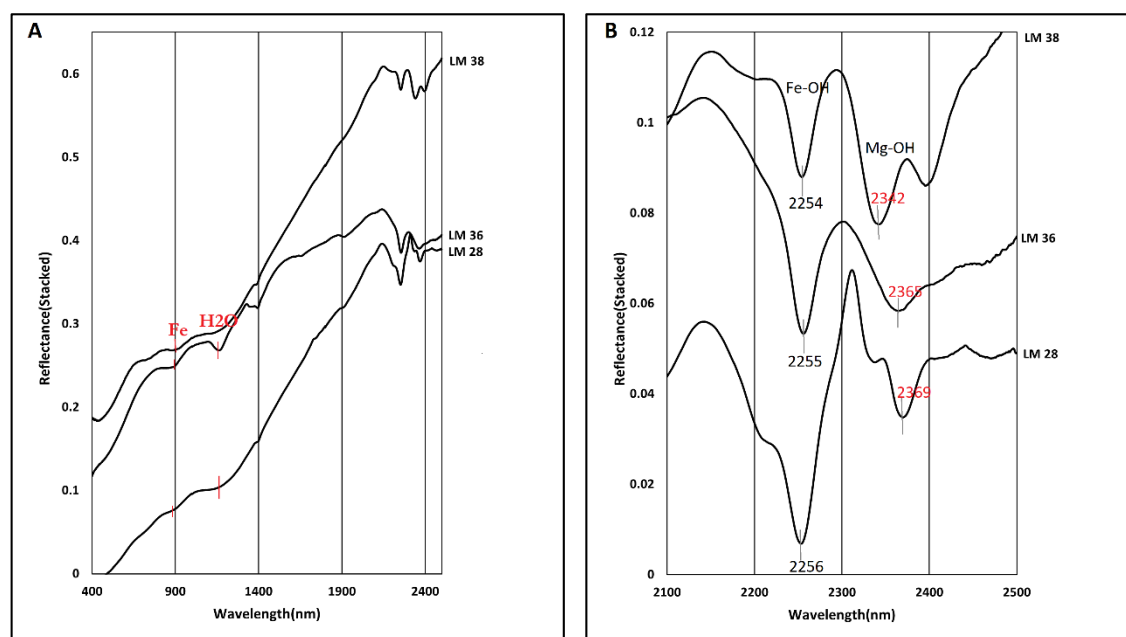


Figure 5.7: VNIR-SWIR spectral characteristics of siderophyllite mica. The samples are stacked based on increasing Fe(VI) and Mg(VI) content in the octahedral site, as calculated from electron microprobe analysis.

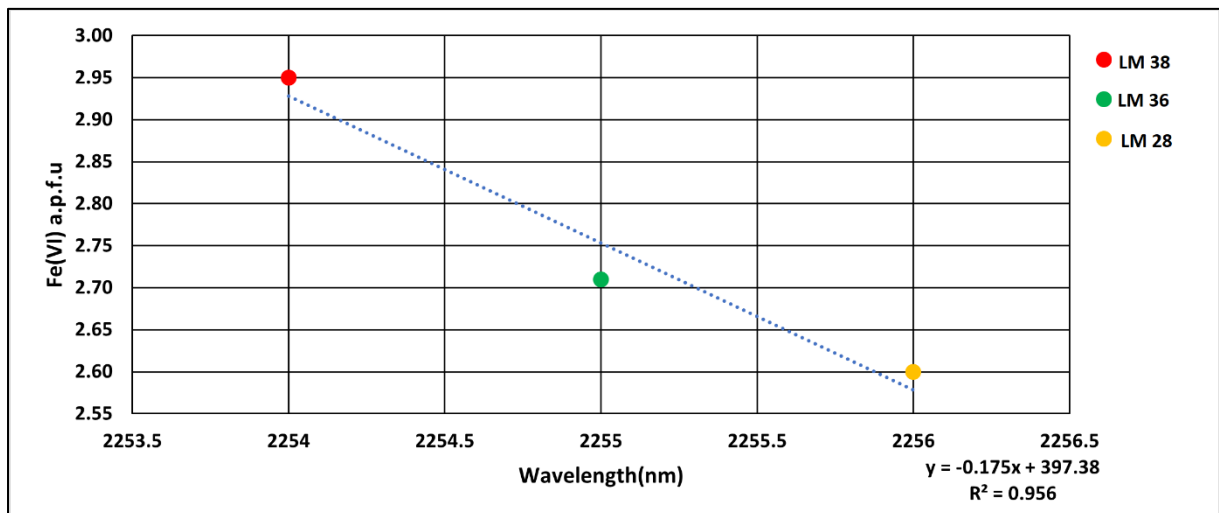


Figure 5.8: Relation between the observed wavelength position of the main cation around 2250 nm absorption minimum in the reflection spectra of siderophyllite and their Fe octahedral site occupancy, as calculated from the electron probe microanalysis. Linear regression results and R^2 values are shown at the bottom right.

5.1.5. Muscovite mica

The VNIR-SWIR spectral characteristics of the studied muscovite mica samples are presented in the figures below. The samples are stacked based on increasing Al(VI) and Mg(VI) content in the octahedral site, as calculated from electron microprobe analysis. Spectrally, muscovite mica displays the first deepest, narrowest, and most symmetric absorption feature around 2200 nm. The wavelength positions of the 2200 nm absorption feature of the studied samples vary from 2196 nm to 2206 nm. The majority of the samples display the feature in the 2200–2206 nm range, while three samples, specifically LM 5, LM 17, and LM 22, exhibit absorption feature at 2196 nm, 2199 nm, and 2198 nm, respectively (*Figure 5.9*). Such discrepancy in the studied samples can be attributed to variations in Al(VI) octahedral site occupancy, ranging from 3.97 to 3.34 out of a maximum of 4 in-dioctahedral micas (Table 3.1). Additionally, the feature shifts systematically towards the shorter wavelength position with increasing Al(VI) content in the octahedral site, which is observed as a spectral shift of 10 nm.

Moreover, all the studied samples have the second deepest, narrowest, and most symmetrical absorption features in the 1409–1413 nm range, which is attributed to the presence of vibrational bonds between OH and H₂O molecules. Furthermore, in the 1916–1921 nm, 2345–2362 nm, and 2435–2450 nm ranges, the studied samples exhibit broad and shallow absorption features. These features are attributed to the presence of vibration bonds of H₂O molecules and secondary Al-OH vibration bonds (Clark et al., 1990; Duke, 1994; Cardoso-Fernandes et al., 2021).

The figures below (*Figures 5.9B and 5.10*) illustrate the stacked spectra based on increasing Al(VI) content in the octahedral site and the scatter diagram plotting the 2200 nm feature against Al(VI) content, respectively. These diagrams clearly depict a negative correlation between the wavelength position of the Al-OH feature and the Al(VI) content in the octahedral site. The wavelength position of the Al-OH feature shifts towards the shorter wavelength with increasing Al(VI) content in the octahedral site (in agreement with Yang et al., 2011; Cloutier et al., 2021). Similarly, the depth of the Al-OH feature also increases with increasing Al(VI) content in the octahedral site (*Figure 5.9B*).

On the other hand, the stacked spectral features based on increasing Mg(VI) content in the octahedral site as well as the scatter diagrams plotting the 2200 nm features against Mg(VI) content in the octahedral site reveal a noticeable shift towards higher wavelengths with increasing Mg(VI) content (*Figures 5.11 and 5.12*).

In the VNIR part of the spectrum, except for sample LM 5, the remaining samples exhibit broad absorption features around 900 nm. As illustrated in Table 3.1, the samples contain relatively high Fe(VI) content in the octahedral site. The presence of Fe(VI) suggests this feature is almost certainly attributed to the electronic process of transition metal Fe. In contrast, samples LM 5 and LM 17 depict shallow and broad absorption features around 550 nm; this feature does not appear in the remaining samples.

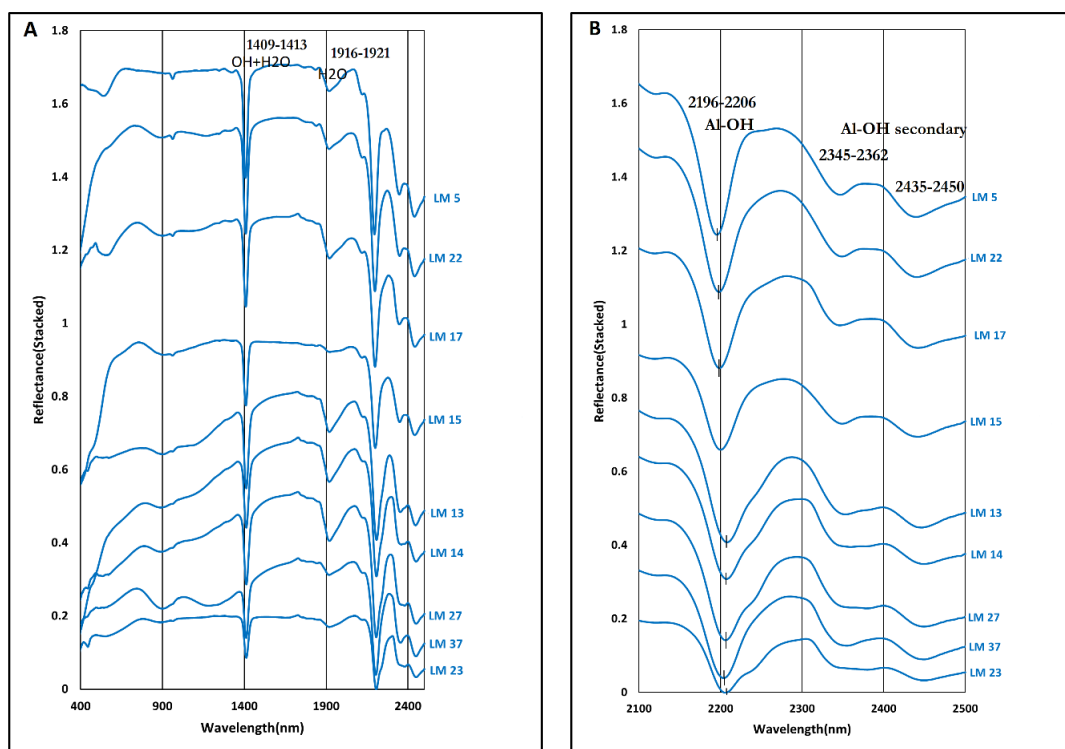


Figure 5.9: VNIR-SWIR spectral characteristics of the studied muscovite mica samples in the 400–2500 nm (Figure A). Figure B depicts the spectral features of muscovite mica in the 2100–2500 nm range to show the shift in wavelength position of the absorption feature formed by octahedral cations such as Al(VI) in the octahedral site. The samples are stacked based on increasing Al(VI) content, as calculated from the electron microprobe analysis.

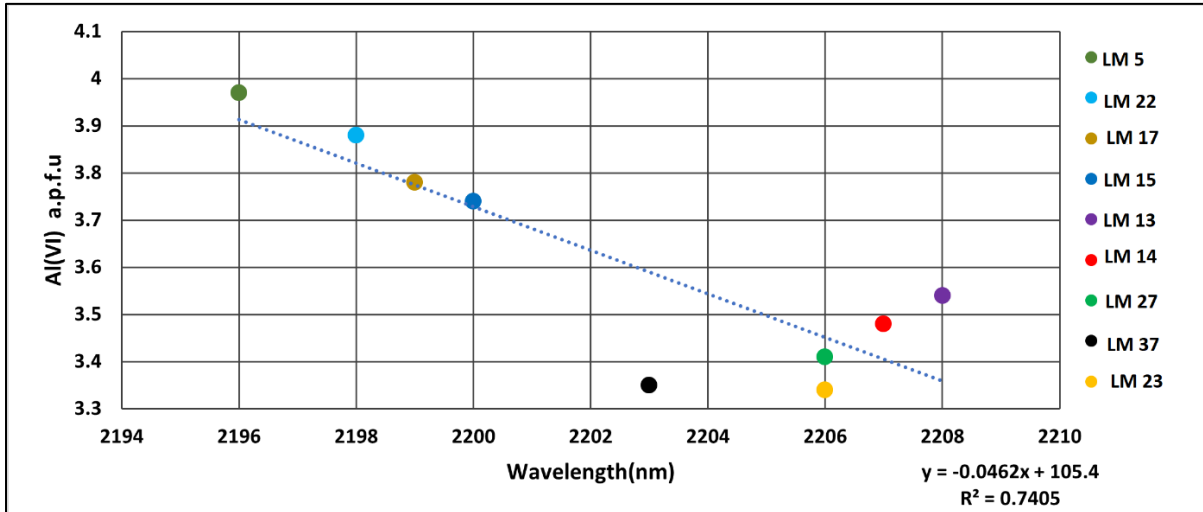


Figure 5.10: Relation between the observed wavelength position of the main cation around 2200 nm absorption minimum in the reflection spectra of muscovite and their Al octahedral site occupancy calculated from the electron probe microanalysis. Linear regression results and R^2 values are shown at the bottom right.

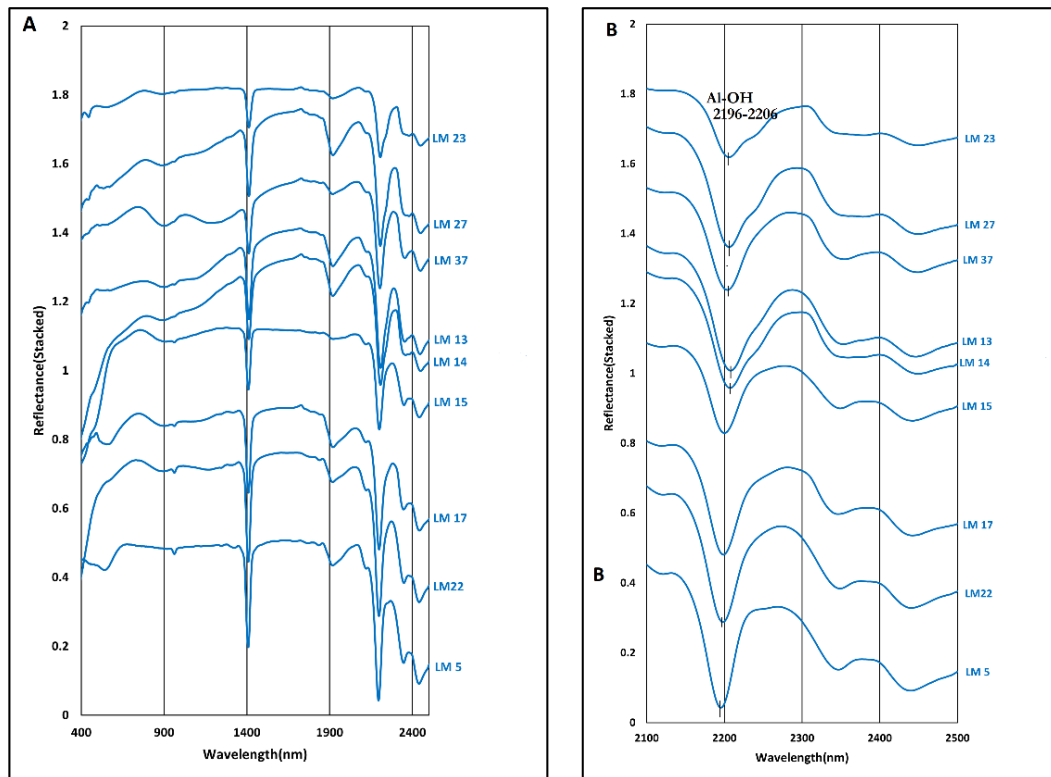


Figure 5.11: VNIR-SWIR spectral characteristics of muscovite mica samples in the 400-2500 nm and 2100-2500 nm. The samples were stacked based on increasing Mg(VI) content in the octahedral site, as calculated from electron microprobe analysis.

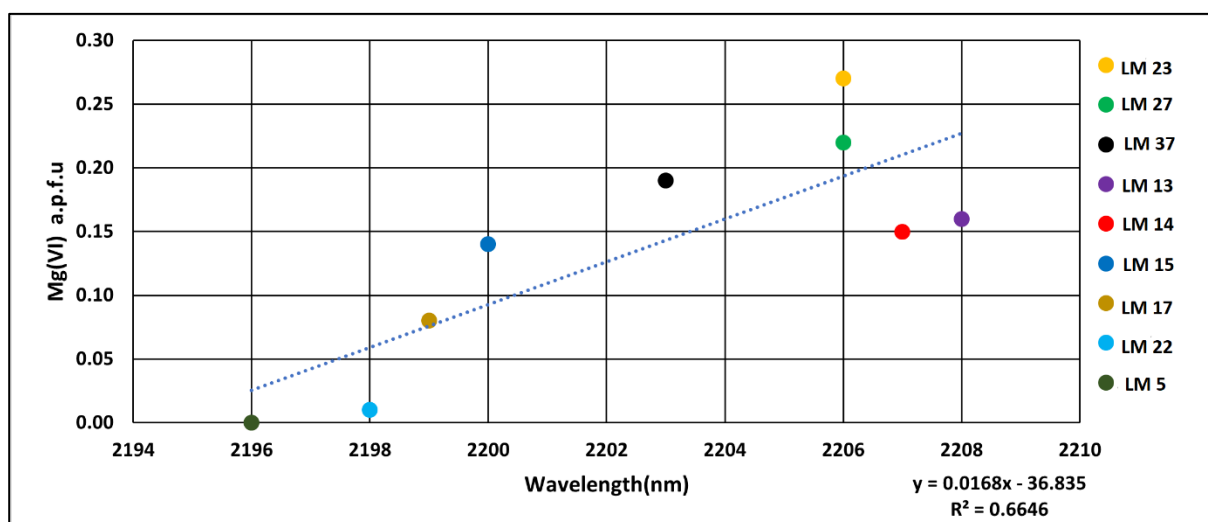


Figure 5.12: Relation between the observed wavelength position of the main cation around 2200 nm absorption minimum in the reflection spectra of lepidolites and their Mg octahedral site occupancy calculated from the electron probe microanalysis. Linear regression results and R^2 values shown at bottom right.

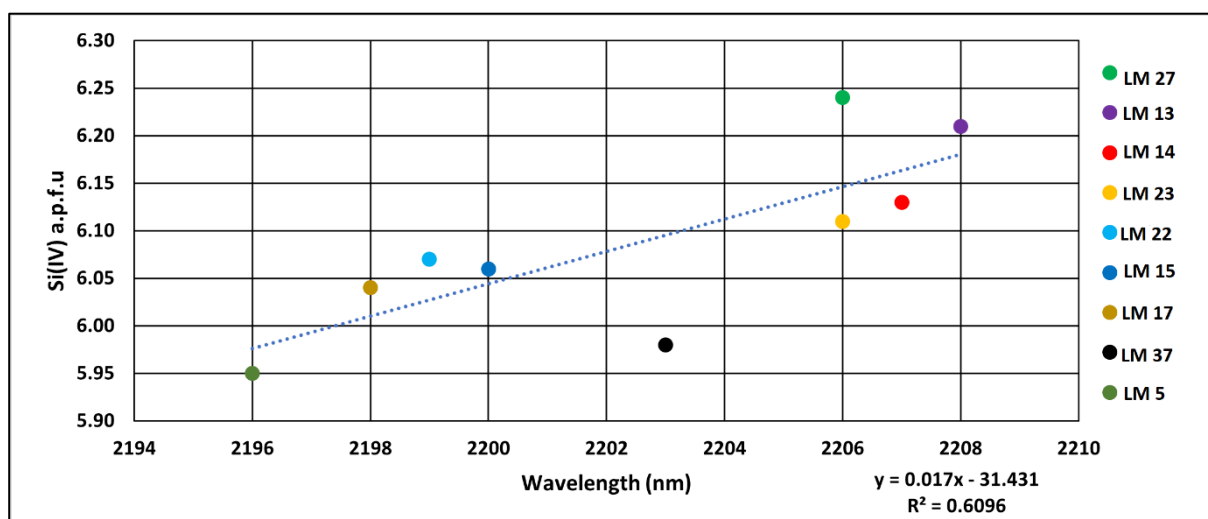


Figure 5.13: Relation between the observed wavelength position of the main cation around 2200 nm absorption minimum in the reflection spectra of lepidolites and their Si tetrahedral site occupancy calculated from the electron probe microanalysis. Linear regression results and R^2 values shown at bottom right.

Similarly, the 2200 nm feature plotted against Si(IV) content in the tetrahedral site also depicts a positive trend. A trend can be seen where the feature is shifting towards a higher wavelength with increasing Si(IV) content in the tetrahedral site.

All these observed shifts are almost certainly attributed to Tschermak substitution $Al^{3+}_{(IV)} + Al^{3+}_{(VI)} \leftrightarrow Si^{4+}_{(IV)} + Mg^{2+}_{(VI)}$ or $Fe^{2+}_{(VI)}$ (Cloutier et al., 2021).

5.1.6. Fuchsite mica

In the SWIR spectrum, the studied fuchsite mica exhibits the first deepest, narrowest, and symmetrical absorption feature at 2210 nm, associated with vibration bonds of Al-OH (Figure 5.14). Additionally, it displays the second deepest, narrowest, and most symmetrical absorption feature at 1412 nm, attributed to vibration bonds between OH and H₂O molecules. Moreover, shallow and broad absorption features are observed at 1932 nm, 2344 nm, and 2444 nm, respectively. These features are almost certainly due to the presence of the vibration bonds of H₂O molecule and secondary Al-OH (Clark et al., 1990; Cloutier et al., 2021).

In the VNIR part of the spectrum, the studied fuchsite mica displays distinct absorption features that distinguish it from other types of studied mica minerals (Figure 5.14A). This distinct feature of the mineral is defined by two relatively wide and almost symmetric absorption features observed at 425 nm and 621 nm. Consequently, these features can serve as diagnostic features of the mineral. The studied fuchsite mica contains a high content of Cr (0.10) in the octahedral site, as indicated in Table 3.1. As a result, these features are almost certainly attributed to the presence of electronic processes involving the transition metals of the Cr ion in the crystal structure of the mineral. Besides, these double absorption features play a significant role in the green colour observed in the mineral, as the Cr ion absorbs light in the red and blue regions of the spectrum while reflecting green light at 512 nm.

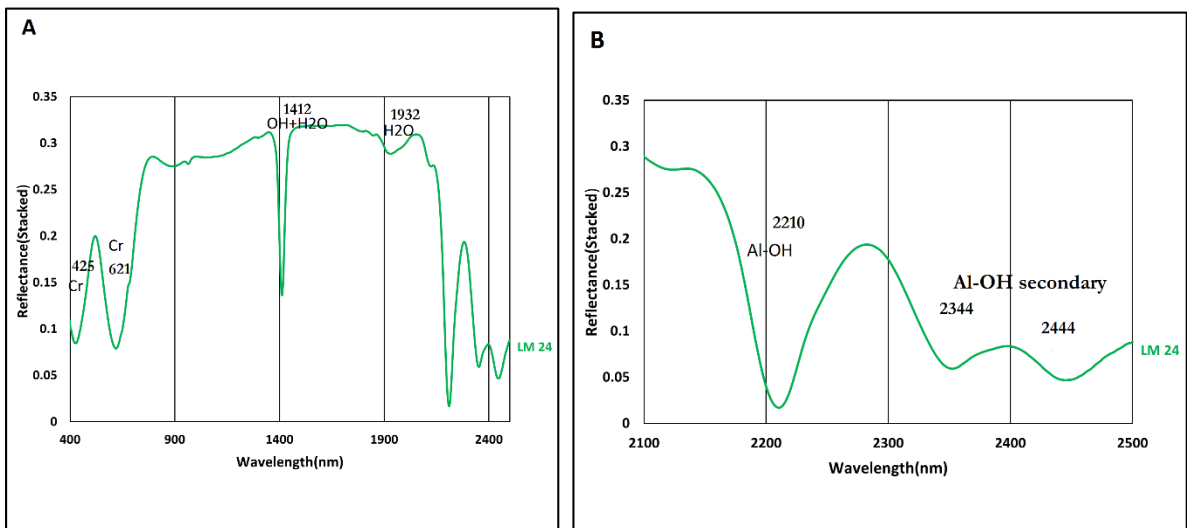


Figure 5.14: VNIR-SWIR spectral characteristics of the studied fuchsite mica in the 400-2500 nm range. The mineral depicts a diagnostic absorption feature in the VNIR part of the spectrum at 425 nm and 621 nm.

5.2 Comparison of VNIR-SWIR spectral characteristics of the studied trioctahedral types of mica

As described in Section 5.1, in the VNIR-SWIR parts of the spectrum, all the studied trioctahedral micas exhibit prominent absorption features (*Figure 5.15*). However, they bear close resemblance in their absorption features. The spectral characteristics of these micas in the 400–2500 nm region are presented in the stacked figure below. Detailed descriptions, including the band assignment, can be found in *Section 5.1*. This section provides a concise summary of the spectral characteristics and distinctive features of the studied trioctahedral type of mica, aiming to aid in their differentiation.

The VNIR and SWIR spectral characteristics of the studied polyolithionite and lepidolite micas exhibit similarity, characterized by broad and shallow absorption features at 459–564 nm and around 900 nm. Additionally, both minerals display deep, narrow, symmetrical, as well as broad and shallow absorption features around 1400 nm, 1900 nm, 2200 nm, 2340 nm, and 2450 nm (*Figure 5.15*). As a result of the comparable shapes and wavelength positions of these absorption features, distinguishing polyolithionite from lepidolite mica is challenging in these regions.

Similarly, in the VNIR and SWIR parts of the spectrum, the studied zinnwaldite and siderophyllite mica exhibit close resemblances in spectral characteristics, marked by the presence of absorption features around 900 nm, 1400 nm, and 2250 nm (*Figure 5.15*). However, in the case of zinnwaldite mica, the feature observed around 900 nm is relatively deep and symmetrical compared to siderophyllite mica. Additionally, the studied zinnwaldite mica depicts an absorption feature around 1900 nm and 2200 nm, which is absent in the studied siderophyllite mica. As a result, the deep and symmetrical absorption feature observed around 900 nm and the presence of an absorption feature observed around 1900 nm and 2200 nm can serve as a distinguishing feature of zinnwaldite to differentiate it from the studied siderophyllite mica. Moreover, the presence of a deep and symmetrical absorption feature around 900 nm and 2250 nm aids in distinguishing the studied zinnwaldite from polyolithionite and lepidolite micas since these features are not observed in the studied polyolithionite and lepidolite micas.

The studied siderophyllite mica doesn't have absorption features around 1900 nm and 2200 nm, which can be explained by the absence of vibrational bonds between H₂O and Al-OH molecules in the crystal structure of the mineral (*Figure 5.15B*). The absence of these features can serve as a diagnostic feature of the studied siderophyllite mica, allowing it to be distinguished from other studied trioctahedral types of mica, such as polyolithionite, lepidolite, and zinnwaldite.

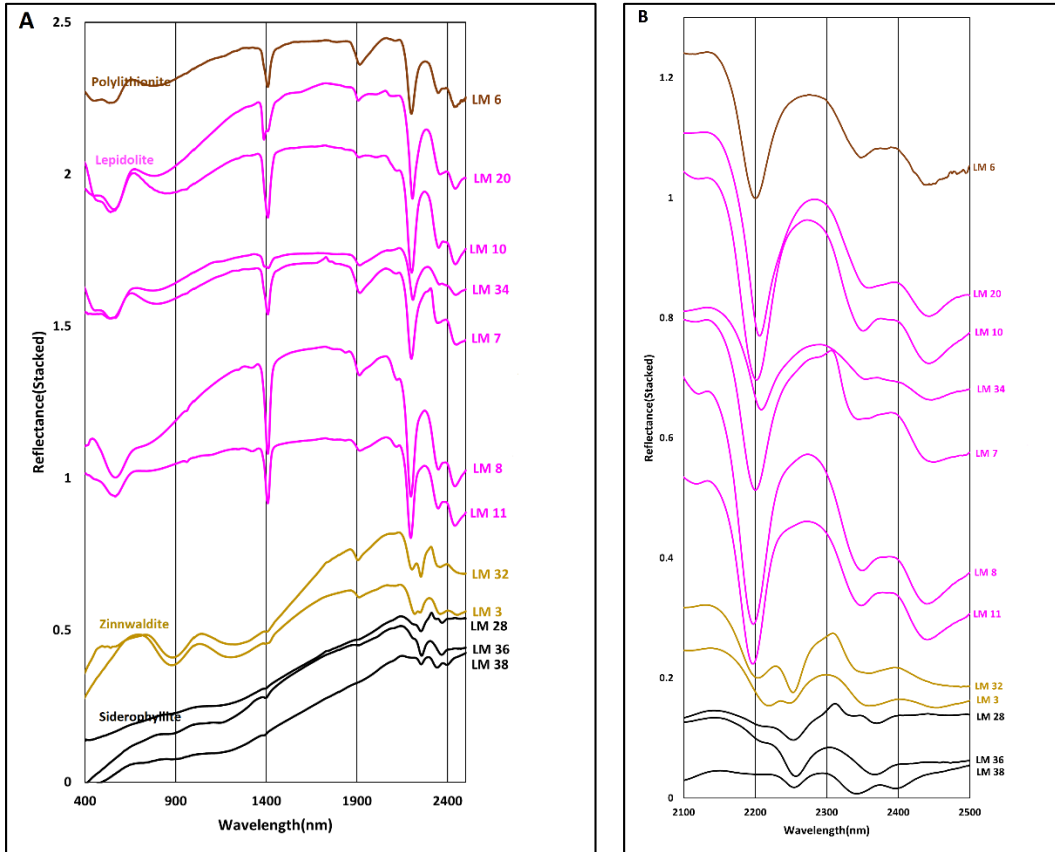


Figure 5.15: VNIR-SWIR spectral characteristics of the studied trioctahedral types of mica. The samples are stacked based on the assumed increasing Li(VI) octahedral site occupancy.

5.3 Comparison of VNIR-SWIR spectral characteristics of the studied lepidolite and muscovite mica

The SWIR spectral characteristics of the studied lepidolite and muscovite mica bear a close resemblance. As illustrated in Figure 5.16, both minerals display well-defined absorption features in the 1400–2500 nm range, attributed to vibration bonds of the hydroxyl ion (OH), H₂O molecule, and Al-OH. The depth of these features is also comparable. Additionally, in both minerals, the 2200 nm feature associated with Al-OH vibration bonds shifts towards the shorter wavelength position with increasing Al(VI) content in the octahedral site (Figure 5.16B). Likewise, the depth of the 2200 nm feature in both minerals increases with increasing Al(VI) content in the octahedral site (Figure 5.16B). As a result, based on the 2200 nm feature, distinguishing lepidolite from muscovite mica is not possible.

On the other hand, in the VNIR part of the spectrum, the studied lepidolite mica depicts shallow and broad absorption features in the 449–564 nm range, which are attributed to the presence of electronic processes in transition metals such as Mn(VI). However, except for LM 5 and LM 17, the majority of muscovite mica minerals do not display absorption features in this range (Figure 5.16B). As indicated in Table 3.1, sample LM 5 contains relatively high Mn(VI) (0.02), which is likely the cause of the absorption feature observed at

542 nm. Additionally, this sample exhibits a pink colour in the hand specimen, which is consistent with the effect of Mn. In contrast, in the case of sample LM 7, as illustrated in Table 3.1, there is an absence of Mn(VI) content in the octahedral site, and it appears colourless in the hand specimen. As a result, the absorption feature observed at 562 in sample LM 17 could possibly be attributed to the influence of other transition elements or impurities.

Therefore, this feature observed in the VNIR part of the spectrum is considered the distinguishing feature of lepidolite mica, as the majority of muscovite mica does not have this feature. However, differentiating them becomes challenging when the muscovite mica exhibits an absorption feature around 560 nm due to the presence of Mn(VI). Additionally, as observed in sample LM 17, the presence of other transition metals or impurities in muscovite mica can also form absorption features in the VNIR part of the spectrum; in this case, distinguishing lepidolite from muscovite is also difficult.

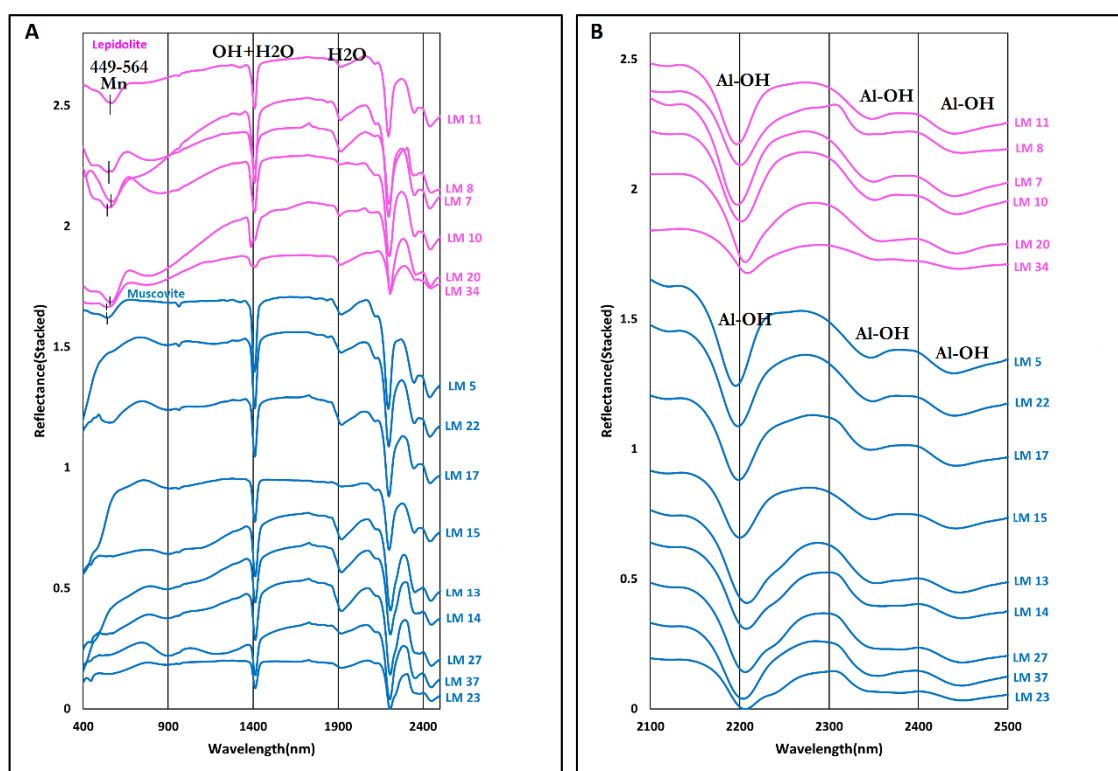


Figure 5.16: VNIR-SWIR spectral characteristics of the studied lepidolite and muscovite micas. The samples are stacked based on increasing Al(VI) content in the octahedral site, as calculated from the electron microprobe analysis. The two mineral groups depict similar spectral characteristics, specifically in the SWIR part of the spectrum, due to the presence of OH, H₂O and Al-OH features.

Table 5.1 Band assignments of absorption features (nm) of the studied mica minerals

Trioctahedral types of mica				
	1 st deepest feature	2 nd deepest feature	3 rd deepest feature	4 th deepest feature
Cations	Al-OH	OH + H₂O	H₂O	Secondary Al-OH features
Sample	Polyolithionite mica			
LM 6	2200	1409	1917	2348
Lepidolite mica				
LM 7	2200	1409	1915	2342
LM 8	2198	1409	1917	2348
LM 10	2202	1408	1908	2349
LM 11	2197	1408	1916	2348
LM 18	2203	1409	1916	2350
LM 20	2206	1388,1410	1907	2355
LM 34	2208	1393,1410	1913	2355
Zinnwaldite mica				
Cations	Al-OH and Fe-OH	Fe	H₂O	Secondary Al-OH features
LM 3	2218,2248	891	1920	2357
LM 32	2252,2205	896	1908	2356
Siderophyllite and other biotite group mica				
	Fe-OH	Mg-OH	-	-
LM 12	2252	2336	-	-
LM 16	2248	2386, 2330	-	-
LM 28	2256	2369, 2335	-	-
LM 35	2256	2369	1403	-
LM 36	2255	2365	1396	-
LM 38	2254	2342	-	-
Diocahedral types of mica (Muscovite and Fuchsite) mica				
Cations	Al-OH	OH +H₂O	H₂O	Secondary Al-OH features
LM 5	2196	1409	1916	2347
LM 13	2208	1413	1919	2353
LM 14	2207	1412	1918	2360
LM 15	2200	1410	1917	2349
LM 17	2199	1409	1919	2347
LM 22	2198	1409	1918	2349
LM 23	2206	1413	1920	2380
LM 25	2200	1410	1920	2349
LM 27	2206	1413	1920	2378
LM 37	2204	1412	1921	2355
	Al-OH	OH +H₂O	Cr³⁺	Cr³⁺
LM 24	2209	1412	621	425

Note: Band assignments of the octahedral cations of the studied mica minerals (adopted from Hunt, 1977; Clark, 1990; Clark et al.,1999; Cloutier et al., 2021). Additionally, it is important to note that, in the case of siderophyllite mica, the first and second deepest absorption features described in the text are interchangeable in the table .

SPECTRAL ANALYSIS OF LITHIUM-BEARING MICAS WITH SHORTWAVE AND LONGWAVE INFRARED SPECTROSCOPY

Table 5.2 Name of the studied mica samples based on EMPA, LWIR-MWIR and VNIR-SWIR spectroscopy

No.	Sample ID	EMPA classification	XRD analysis	LWIR-MWIR	VNIR-SWIR	Conclusion
1	LM 3	zinnwaldite	Can not distinguish the studied mica minerals	Zinnwaldite	Zinnwaldite	Zinnwaldite. Based on EMPA classification and spectral features obtained from VNIR and SWIR spectroscopy.
2	LM 5	Muscovite		Muscovite	Difficult to differentiate this sample from lepidolite samples in the VNIR and SWIR spectroscopy	Muscovite. Based on EMPA classification and the distinct absorption features observed in the LWIR and MWIR spectroscopy.
3	LM 6	Falls close to polyolithionite region		Polyolithionite	VNIR and SWIR spectroscopy cannot distinguish the studied polyolithionite from lepidolite mica samples.	Polyolithionite. Based on the EMPA classification and distinctive absorption features observed in the LWIR and MWIR spectroscopy.
4	LM 7	Lepidolite		Lepidolite		
5	LM 8	Lepidolite		Lepidolite		
6	LM 10	Lepidolite		Lepidolite		
7	LM 11	Lepidolite		Lepidolite		Lepidolite. Based on the EMPA classification and distinctive spectral feature observed in the LWIR spectroscopy
8	LM 12	-		Biotite group mica	Biotite group mica	Due to the lack of EMPA data, the name of this sample was given by a comparative analysis of absorption features observed in the LWIR, MWIR, VNIR, and SWIR spectroscopy of the other samples (e.g., LM 28, which is siderophyllite mica). Since it closely resembles to LM 28, it was given a general name (biotite group mica).
9	LM 13	Muscovite		Muscovite	Muscovite	Muscovite. Based on the distinct absorption features obtained from VNIR, LWIR, and MWIR spectroscopy.
10	LM 14	Muscovite		Muscovite		
11	LM 15	Muscovite		Muscovite		
12	LM 16	-		Biotite group mica	Biotite group mica	The same as sample LM 12
13	LM 17	Muscovite		Muscovite	VNIR and SWIR cannot distinguish this sample	Muscovite. Based on the distinct absorption features obtained from LWIR and MWIR spectroscopy

SPECTRAL ANALYSIS OF LITHIUM-BEARING MICAS WITH SHORTWAVE AND LONGWAVE INFRARED SPECTROSCOPY

					from the studied lepidolite samples	
14	LM 18	Lepidolite		Lepidolite	VNIR and SWIR cannot distinguish the studied lepidolite samples and muscovite sample.	Lepidolite. Based on the EMPA classification and distinctive spectral features observed in the LWIR spectroscopy.
15	LM 20	Lepidolite		Lepidolite		
16	LM 22	Muscovite		Muscovite	Muscovite	Muscovite. Based on the distinct absorption features obtained from VNIR, LWIR and MWIR spectroscopy.
17	LM 23	Muscovite		Muscovite		
18	LM 24	Muscovite		Fuchsite	Fuchsite	Fuchsite. Based on the distinctive absorption features observed in the VNIR and LWIR spectroscopy
19	LM 25	Muscovite		Muscovite	Muscovite	Muscovite. Based on the distinct absorption features obtained from VNIR, LWIR and MWIR spectroscopy.
20	LM 27	Muscovite		Muscovite		
21	LM 28	Siderophyllite		Biotite group mica	Biotite group mica	Siderophyllite. Based on EMPA classification and absorption features obtained from VNIR, SWIR , and MWIR spectroscopy
22	LM 32	zinnwaldite		Zinnwaldite	Zinnwaldite	Zinnwaldite. Based on the spectral features observed in the VNIR, SWIR, and LWIR spectroscopy
23	LM 34	Lepidolite		Lepidolite	The same LM 18	Lepidolite. Based on the EMPA classification and distinctive spectral feature observed in the LWIR spectroscopy
24	LM 35	-		Biotite group mica	Biotite group mica	The same as sample LM 12
25	LM 36	Siderophyllite		Biotite group mica	Biotite group mica	Siderophyllite. Based on EMPA classification and absorption features observed in the VNIR, SWIR, and MWIR spectroscopy
26	LM 37	Muscovite		Muscovite	Muscovite	Muscovite. Based on the distinct feature obtained from VNIR, LWIR and MWIR spectroscopy
27	LM 38	Siderophyllite		Biotite group mica	Biotite group mica	Siderophyllite. Based on EMPA classification and absorption features observed in the VNIR, SWIR, and MWIR spectroscopy

6 CALCULATIONS OF COMBINATION AND OVERTONES AND COMPARISON WITH OBSERVED FEATURES

In this study, the exact wavelength position of the Al-Al-OH bending vibration in the studied trioctahedral types of mica, such as polyolithionite, lepidolite, and zinnwaldite, could not be determined. This arose due to the interference of the bigger absorption peaks related to Si and Al tetrahedral cations. As a result, comparison of the calculated and observed combinations of vibration bonds associated with the Al-OH feature (Al-OH, 2Al-OH, or 3Al-OH) was not possible. These features are formed due to the combination band of bending (δ Al-Al-OH) and stretching (ν Al-Al-OH) fundamental vibrations.

On the other hand, significant variations were observed between the calculated first overtones formed due to 2*AlAl-OH stretch vibrations ($2*3620\text{ cm}^{-1}$) and the observed overtones detected around 1400 nm. The observed overtones are associated with (the bond between O and H) and the H₂O molecule. As can be seen in Table 6.1, the calculated overtones are lower compared to the observed overtones detected around 1400 nm.

In the studied dioctahedral types of mica, such as muscovite and fuchsite, the calculated combination vibration bonds (resulting from the combination bands of bending vibrations of Al-Al-OH (δ Al-Al-OH) observed around 915 cm^{-1} and stretching vibrations of Al-Al-OH (ν Al-Al-OH) observed around 3621 cm^{-1}) were found to be lower than the observed combination vibrational bonds detected around 2200 nm. Similarly, the calculated overtones formed due to 2*Al-Al-OH stretch vibrations ($2*3620\text{ cm}^{-1}$) were also lower than the observed overtones detected around 1400 nm.

SPECTRAL ANALYSIS OF LITHIUM-BEARING MICAS WITH SHORTWAVE AND LONGWAVE INFRARED SPECTROSCOPY

Table 6.1 The calculated and observed overtones and combinations of vibrational bonds of the studied mica minerals.

Sample	δOH (Al-Al-OH)	νOH (Al-Al-OH)	Calculated combination $\delta\text{OH} + \nu\text{OH}$	Observed combination	First overtone ($2\nu\text{Al-Al-OH}$) Calculated	Observed
Polyolithionite						
LM 6	-	3621	-	2200 nm	7242 cm^{-1} (1380 nm)	1409 nm
Lepidolite						
LM 7	-	3627	-	2200 nm	7254 cm^{-1} (1378 nm)	1409 nm
LM 8	-	3626	-	2198 nm	7252 cm^{-1} (1379 nm)	1409 nm
LM 10	-	3625	-	2202 nm	7250 cm^{-1} (1370 nm)	1408 nm
LM 11	-	3624	-	2197 nm	7248 cm^{-1} (1380 nm)	1408 nm
LM 18	-	3629	-	2203 nm	7258 cm^{-1} (1378 nm)	1409 nm
LM 20	-	3697	-	2206 nm	7394 cm^{-1} (1352 nm)	1388 nm
LM 34	-	3626	-	2208 nm	7252 cm^{-1} (1379 nm)	1393 nm
Zinnwaldite						
LM 3	-	3625	-	-		
LM 32	-	3621	-	-		
Muscovite and Fuchsite						
LM 5	928 cm^{-1}	3627 cm^{-1}	4555 cm^{-1} (2195 nm)	2196 nm	7254 cm^{-1} (1378 nm)	1409 nm
LM 13	926 cm^{-1}	3621 cm^{-1}	4547 cm^{-1} (2199 nm)	2208 nm	7242 cm^{-1} (1380 nm)	1413 nm
LM 14	920 cm^{-1}	3623 cm^{-1}	4543 cm^{-1} (2200 nm)	2207 nm	7246 cm^{-1} (1380 nm)	1412 nm
LM 15	921 cm^{-1}	3624 cm^{-1}	4545 cm^{-1} (2200 nm)	2200 nm	7248 cm^{-1} (1380 nm)	1410 nm
LM 17	926 cm^{-1}	3626 cm^{-1}	4552 cm^{-1} (2196 nm)	2199 nm	7252 cm^{-1} (1379 nm)	1409 nm
LM 22	922 cm^{-1}	3625 cm^{-1}	4547 cm^{-1} (2199 nm)	2198 nm	7250 cm^{-1} (1379 nm)	1409 nm
LM 23	918 cm^{-1}	3622 cm^{-1}	4540 cm^{-1} (2202 nm)	2206 nm	7244 cm^{-1} (1380 nm)	1413 nm
LM 25	913 cm^{-1}	3626 cm^{-1}	4539 cm^{-1} (2203 nm)	2200 nm	7252 cm^{-1} (1379 nm)	1410 nm
LM 27	923 cm^{-1}	3624 cm^{-1}	4547 cm^{-1} (2200 nm)	2206 nm	7248 cm^{-1} (1380 nm)	1413 nm
LM 37	920 cm^{-1}	3622 cm^{-1}	4542 cm^{-1} (2201 nm)	2204 nm	7244 cm^{-1} (1380 nm)	1412 nm
LM 24	907 cm^{-1}	3621 cm^{-1}	4528 cm^{-1} (2208 nm)	2209 nm	7242 cm^{-1} (1380 nm)	1412 nm

The scatter plot (*Figure 6.1*) depicts the wavelength positions of the calculated and observed overtones and combinations of vibrational bonds of the studied muscovite mica samples. As can be seen in the figure, all the points fall perfectly in the 1:1 line, which indicates perfect correlation between calculated and observed overtones and the combinations of vibrational bonds. However, some of the calculated points are offset systematically because the calculated wavelength is lower (higher energy) than the observed one (Table 6.1), which means that some extra energy is needed to excite the combination vibration.

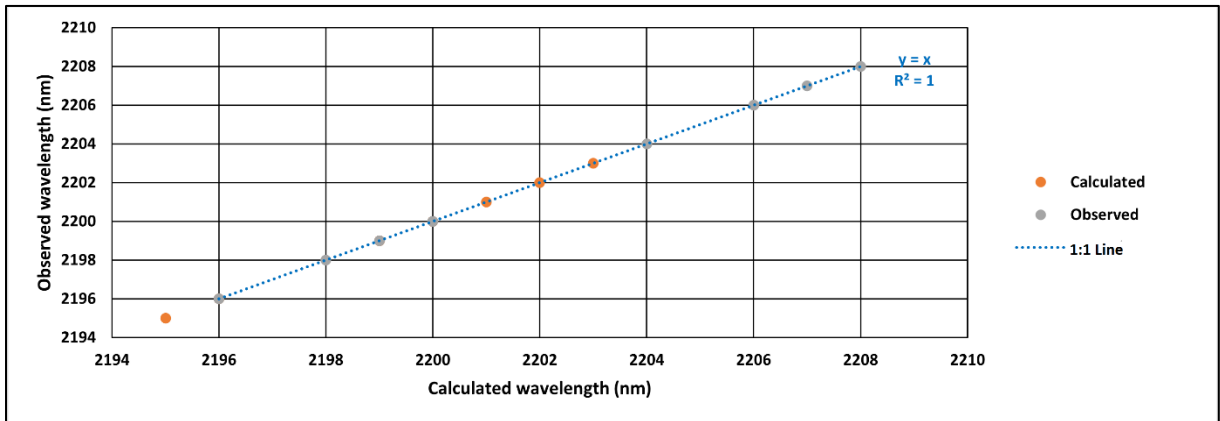


Figure 6.1: Shows the wavelength positions of calculated and observed overtones and combinations of the studied muscovite mica samples. All the points fall on the 1:1 line (a line through 2195, 2195 and 2208, 2208).

7 DISCUSSIONS

In this study, data acquired from electron microprobe analysis (EMPA), X-ray Diffraction (XRD), LWIR-MWIR spectroscopy, and VNIR-SWIR spectroscopy were used to analyze the spectral characteristics and the effect of the elemental substitutions on the shift of the absorption features of the dioctahedral and trioctahedral types of mica. This chapter discusses the methods and results obtained from this study. The discussion is as follows:

7.1 Methods

The electron microprobe analysis (EMPA) provides the major and minor element concentrations of the studied mica minerals, offering valuable insight into their chemical compositions. Nevertheless, it has limitations when it comes to detecting certain elements, such as lithium (Li), which is a critical octahedral cation to identify Li-bearing micas. This study addressed this limitation by estimating Li(VI) content using major element correlation, such as MgO for siderophyllite mica, as recommended by Tischendorf et al. (2004), and assuming Li(VI) content for polyolithionite, lepidolite, zinnwaldite, muscovite, and fuchsite mica, as described in Section 2.2.1. Most of the studied samples fall in the right position on the classification diagram. However, one sample from lepidolite mica falls outside of the region, and a polyolithionite sample (LM 6) also deviates from the right position (*Figure 3.1*). This suggests the assumed lithium concentration introduces a certain degree of uncertainty in identifying lithium-bearing micas.

In X-ray diffraction (XRD) analysis, all the studied mica minerals exhibit similar diffraction patterns with nearly the same peak positions (*Figure 3.2*). This similarity arises because the method is sensitive to peak shifts due to height differences and relative peak height issues caused by the preferential alignment of the sheet-like minerals. As a result, distinguishing the studied mica minerals using X-ray diffraction proved challenging.

LWIR-MWIR spectroscopy, on the other hand, provided valuable insights into the distinctive absorption features of the studied mica minerals. Notably, in the LWIR part of the spectrum, in the 700–1100 cm^{-1} range, all the studied mica minerals display distinct shapes of absorption features, allowing their identification. Additionally, the absorption features obtained from the LWIR part of the spectrum also reveal the absorption peak associated with Li-OH bending vibrations. The distinctive absorption feature, combined with the presence of an absorption peak associated with Li-OH, allows us to identify Li-bearing mica. These discriminations can be based on the overall shape of the spectral feature without relying on specific absorption peak shifts (*Figure 7.1*).

The VNIR-SWIR spectroscopy yielded valuable insights into the relationship between the absorption features and chemical compositions of the studied mica minerals. Additionally, it is effective for determining the systematic shift of the absorption features associated with vibration bonds of main octahedral cations, such as Al-OH, Fe-OH, and Mg-OH. Nevertheless, it has limitations in detecting the absorption feature resulting from the vibration bonds of Li-OH.

The result shows that all the studied mica minerals depict prominent absorption features attributed to the presence of transition metals such as Ti, Mn, Fe, and Cr and vibration bonds of OH, H₂O, Al-OH, Fe-OH, and Mg-OH. However, in the VNIR-SWIR part of the spectrum, the studied mica minerals exhibit a close resemblance in their absorption features. For instance, the spectral characteristics of polyolithionite and lepidolite mica closely resemble those of muscovite and fuchsite. Likewise, the spectral features of zinnwaldite and siderophyllite mica also closely resemble each other, especially in the 1400–2500 nm range (*Figure 7.2*).

These similarities in spectral characteristics could potentially be attributed to two factors. Firstly, the inability to determine the wavelength position of the absorption features associated with Li-OH. Secondly, due to the comparable shape of absorption features and wavelength positions of vibration bonds involving OH, H₂O molecules, Al-OH, Fe-OH, and Mg-OH, both in lithium-bearing mica and non-lithium-bearing mica. As a result, the spectral characteristics obtained from VNIR-SWIR spectroscopy proved challenging for distinguishing Li-bearing micas.

Therefore, based on the results obtained from this study, distinguishing lithium-bearing mica using VNIR and SWIR spectroscopy was not possible. Conversely, LWIR spectroscopy was found to be the most promising analytical method to distinguish lithium-bearing micas.

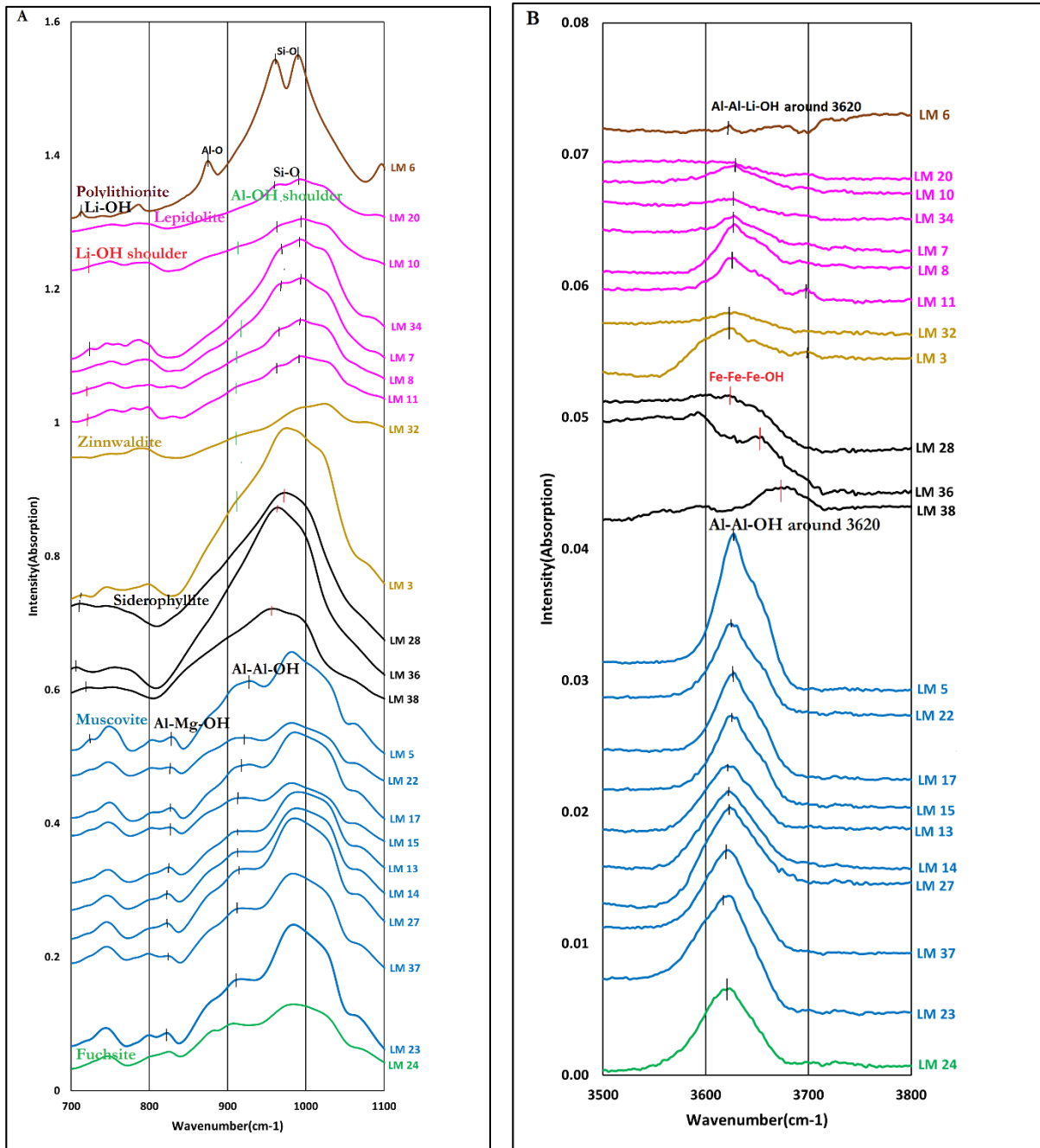


Figure 7.1: LWIR-MWIR spectral features of the studied trioctahedral and dioctahedral types of mica. Figure A depicts the distinct shape of the absorption features of the studied mica minerals in the OH-bending region. Figure B shows the spectral features of the studied mica in the OH-stretching region.

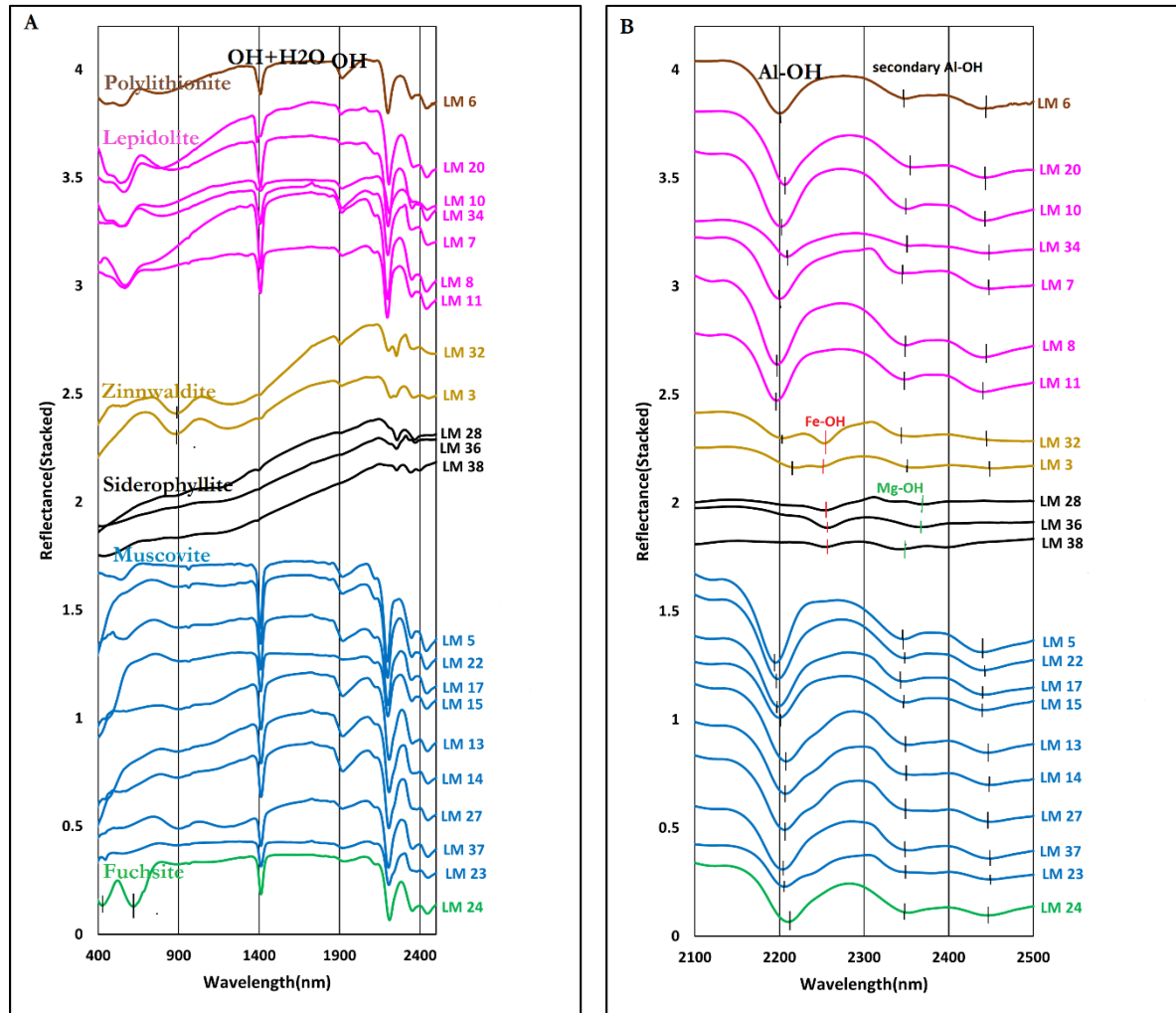


Figure 7.2: VNIR-SWIR spectral characteristics of the studied trioctahedral and dioctahedral types of mica. Figure A displays the spectral characteristics of the studied mica minerals in the 400–2500 nm region and the diagnostic features of the studied zinnwaldite and fuchsite mica. Figure B shows the spectral features of the studied mica in the 2100–2500 nm region.

7.2 Discussion on the results

7.2.1 The link between LWIR-MWIR spectral features and elemental substitutions

In this study, to understand the relationship between the spectral features and elemental substitution, the first step was identifying and assigning the bands of the absorption peaks to the main tetrahedral and octahedral cations that comprise the studied mica minerals. The absorption peaks that are associated with the main tetrahedral and octahedral cations were assigned based on previous studies, considering the chemical composition of the minerals and existing knowledge of their spectral signatures.

In the studied trioctahedral types of mica, such as polyolithionite, lepidolite, zinnwaldite, and siderophyllite, the absorption peaks observed in the 700–1100 cm^{-1} range are primarily attributed to Si-O in-plane

vibrations in the 957-999 cm^{-1} range, Al-O-Al in-plane vibrations in the 829–833 cm^{-1} range, Si-O-Si symmetric stretch modes in the 760–807 cm^{-1} range, and Al-O-Si in-plane vibrations in the 744–759 cm^{-1} range. These peaks and their respective band assignments have also been identified in previous studies on phlogopite and annite-siderophyllite micas (Jenkins, 1989; Redhammer et al., 2000; Beran, 2002).

However, the absorption peaks attributed to Fe-OH and Mg-OH bending vibrations, particularly in the studied zinnwaldite and siderophyllite mica, were not possible to identify. The reason is due to the dominance of absorption peaks attributed to Si and Al tetrahedral cations, hiding the visibility of absorption peaks associated with Fe-OH and Mg-OH bending vibrations. This indicated that in the 700–1100 cm^{-1} range, the tetrahedral cations, such as Si(IV) and Al(IV), have a significant influence on the formation of the absorption peaks observed in the studied trioctahedral types of mica.

On the other hand, in the studied lepidolite and zinnwaldite mica, a weakly expressed shoulder associated with Al-Al-OH bending vibrations around the 925 cm^{-1} region is readily discernable. Nevertheless, it was not possible to determine the exact wavenumber positions due to the interference of prominent absorption peaks associated with Si(IV) and Al(IV) tetrahedral cations (*Figure 7.1A*).

Similarly, the absorption peak associated with the presence of Li(VI) cation bonded with OH (Li-OH) bending vibration in the 706-725 cm^{-1} range is clearly observed in the studied trioctahedral types of mica. However, in samples such as LM 7, LM 8, LM 10, LM 11, and LM 20 from lepidolite and LM 32 from zinnwaldite mica, the absorption peak associated with Li-OH is only visible as a weakly expressed shoulder (*Figure 7.1A*). This observation also implies that the visibility of the peak is hidden by the presence of bigger absorption peaks attributed to Si(IV) and Al(IV) tetrahedral cations.

In the 3500–3800 cm^{-1} region, absorption peaks associated with Al-OH and Fe-OH stretching vibrations are the prominent features observed in the studied trioctahedral types of mica. As observed in *Figure 7.1B*, the studied polyolithionite, lepidolite, and zinnwaldite exhibit absorption peaks around the 3620 cm^{-1} region, which are attributed to stretching vibrations of Al-Al-Li-OH. A previous study by Robert et al. (1989) also identified this feature on the ephesite mica end member. In the case of siderophyllite mica, the absorption peaks associated with Fe^{2+} - Fe^{2+} - Fe^{2+} -OH and Al^{3+} - Al^{3+} - Fe^{2+} -OH stretching vibrations are observed in the 3591–3624 cm^{-1} range (*Figure 7.1B*). Notably, the absorption peak observed around 3591 cm^{-1} is absent in the other studied trioctahedral types of mica. The reason is probably due to the high concentration of Fe in the studied siderophyllite mica compared to the other studied micas (*Table 3.1*). These absorption peaks and their corresponding band assignments have also been identified in a previous study by Redhammer et al. (2000), particularly in the annite-siderophyllite micas.

In the dioctahedral types of mica, such as muscovite and fuchsite, the absorption peaks are distinct and similar to those observed in previous studies (e.g., Martínez-Alonso et al., 2002; Beran, 2002; Cloutier et al., 2021). In the 700–1100 cm^{-1} range, the absorption peaks observed in the studied muscovite and fuchsite mica arise from the vibration bonds involving the Si-O-Si in-plane vibrations in the 979–988 cm^{-1} range, the Al-Al-OH bending vibration in the 907–928 cm^{-1} range, and the Al-Mg-OH bending vibration in the 822–828 cm^{-1} range. Additionally, these features, specifically the Al-Al-OH observed in the 917–928 cm^{-1} range, were found to be correlated with the absorption features observed in the SWIR part of the spectrum.

In the 3500–3800 cm^{-1} range, the sharp and symmetric absorption peak observed in both muscovite and fuchsite mica around 3620 cm^{-1} are attributed to Al-Al-OH stretching vibration. This is in agreement with previous studies of muscovite mica conducted by Besson & Drits (1997); Martínez-Alonso et al. (2002); Cloutier et al. (2021).

After assigning the absorption peaks to the main tetrahedral and octahedral cations, the subsequent step involved observing the systematic shift of these absorption peaks. In the case of trioctahedral types of mica, specifically lepidolite and siderophyllite around 980 cm^{-1} , a shift of the absorption peak towards the higher wavenumber was observed with increasing Si(IV) content in the tetrahedral site (*Figure 7.1A*). However, it is important to note that this shift was not consistently systematic throughout the samples. Despite its non-systematic nature, the shift is likely attributed to the potential substitution of Al(IV) by Si(IV) in the tetrahedral site. Additionally, in the studied lepidolite mica around 960 cm^{-1} , a shift of the absorption peak was also observed towards the shorter wavenumber with increasing Si(IV) content in the tetrahedral site. Similarly, the shift of this peak was not systematic throughout the samples (*Figure 7.1A*). This observed shift is probably due to the possible substitution of Si(IV) by Al(IV) in the tetrahedral site.

Over all, in the LWIR part of the spectrum, due to the dominance of Al(IV) and Si(IV)-related absorption peaks, determining the wavenumber position of the absorption peaks attributed to the bending vibration of the main octahedral cations, such as Al-OH, Li-OH, Fe-OH, and Mg-OH, was not possible. As a result, the effects of elemental substitution caused by the bending vibration of octahedral cations in the studied trioctahedral types of mica minerals were not determined.

Conversely, in the studied muscovite mica, systematic shifts were observed based on the stacked spectra of increasing Al(VI) and Mg(VI) content in the octahedral site (*Figure 7.1A*). Similarly, the scatter diagrams plotting absorption features around 915 cm^{-1} against increasing Al(VI) content, as well as absorption features around 820 cm^{-1} against increasing Mg(VI) content, also illustrate systematic shifts. In the 917–928 cm^{-1} range, the absorption peak shifted towards the higher wavenumber with increasing Al(VI) content in the octahedral site (*Figure 7.3*). In contrast, in the 822–828 cm^{-1} range, the absorption peak shifted systematically towards the higher wavenumber with decreasing Mg(VI) content in the octahedral site (*Figure 7.5*). These

observed shifts of the absorption peaks are almost certainly associated with the potential substitution of Al(VI) and Mg(VI) in the octahedral site.

As illustrated in Figure 7.4, in the 3500–3800 cm^{-1} range, the Al-OH absorption peak shifts towards the higher wavenumber with increasing Al(VI) in the octahedral site. For instance, sample LM 5 contains the highest Al(VI) content, and the peak is observed at 3627 cm^{-1} and sample LM 23 contains the lowest Al(VI) content, and the peak is observed at 3621 cm^{-1} (in agreement with Besson & Drits, 1997). This observed shift is almost certainly attributed to the potential substitution of Mg(VI) by Al(VI) in the octahedral site.

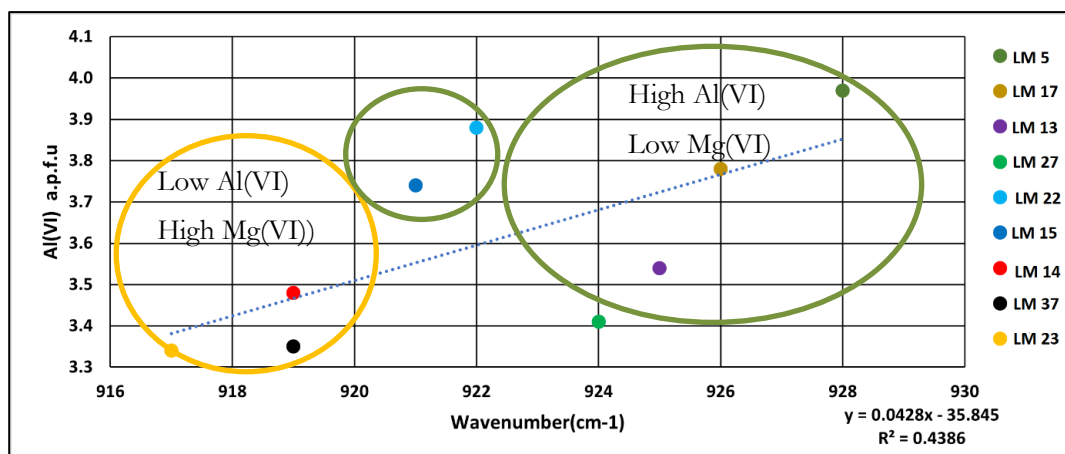


Figure 7.3: Relationship between the observed wavenumber position of the main cation around the 915 cm^{-1} absorption peak in the LWIR reflection spectra of muscovite and their Al octahedral site occupancy calculated from the electron probe microanalysis. Linear regression results and R^2 values are shown at the bottom right.

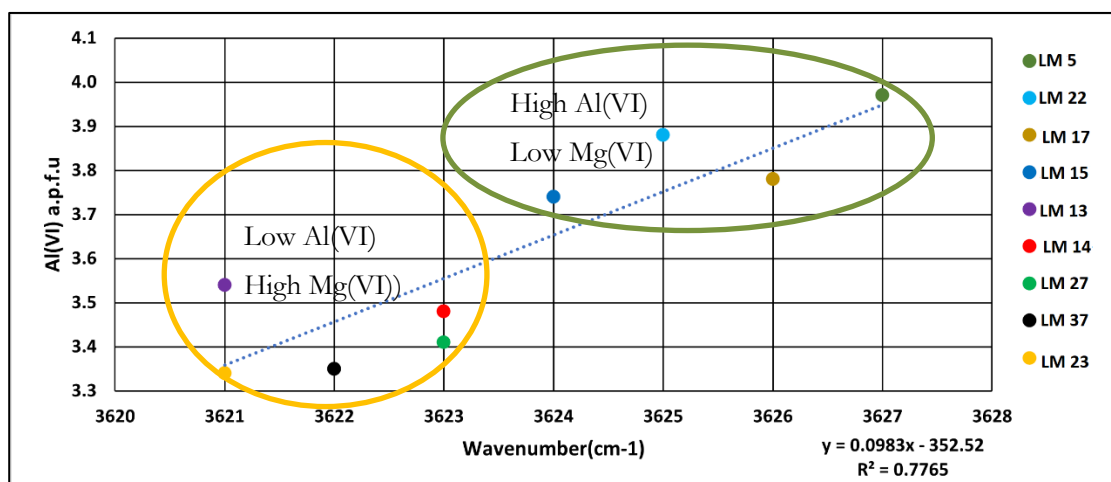


Figure 7.4: Relationship between the observed wavenumber position of the main cation around the 3620 cm^{-1} absorption peak in the LWIR reflection spectra of muscovite and their Al octahedral site occupancy calculated from the electron probe microanalysis. Linear regression results and R^2 values are shown at the bottom right.

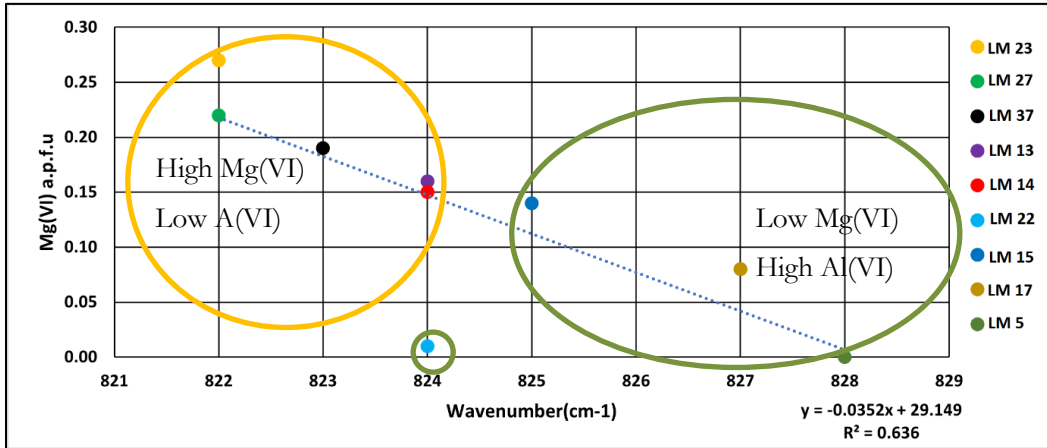


Figure 7.5: Relationship between the observed wavenumber position of the main cation around the 820 cm⁻¹ absorption peak in the LWIR reflection spectra of muscovite and their Mg octahedral site occupancy, as calculated from the electron probe microanalysis. Linear regression results and R² values are shown at the bottom right.

7.2.2 The link between SWIR spectral features and elemental substitutions

The spectral characteristics acquired from the SWIR spectroscopy yielded significant insights into the systematic shift of the absorption features resulting from the substitution of the main octahedral cations that comprise the studied mica minerals. This phenomenon is observed in both dioctahedral types of mica (e.g., muscovite) and trioctahedral types of mica (e.g., lepidolite), notably in the 2100–2500 nm range.

Likewise, to understand the relation between elemental substitution and the shift of absorption features, the first step involved assigning the bands to the main octahedral cations. The result indicates that in both dioctahedral types of mica, such as muscovite and fuchsite, and trioctahedral types of mica, including polyolithionite, lepidolite, and zinnwaldite, the absorption feature formed as a result of the vibration bond of Al-OH is the predominant feature, observed around 2200 nm. Additionally, secondary Al-OH features are also commonly discernible in the studied dioctahedral and trioctahedral types of mica, typically observed around 2350 nm and 2440 nm. The Fe-OH vibration bond is the predominant feature in the studied zinnwaldite and siderophyllite mica, observed around 2250 nm. The absorption feature arising from the vibration bond of Mg-OH is a common feature in the studied siderophyllite mica, primarily observed around 2340 nm.

In the studied muscovite mica, the stacked spectra analysis revealed a systematic shift of absorption feature towards the shorter wavelength with increasing Al(VI) content in the octahedral site. Additionally, the scatter diagram plotting 2200 nm feature against Al(VI) content depicts a negative correlation while displaying a positive correlation with Mg(VI) (Figure 7.6 and 7.7). These discernible patterns can be attributed to Tschermak substitutions involving $\text{Al}^{3+}(\text{IV}) + \text{Al}^{3+}(\text{VI}) \longleftrightarrow \text{Si}^{4+}(\text{IV}) + \text{Mg}^{2+}(\text{VI})$ or $\text{Fe}^{2+}(\text{VI})$. This substitution has a substantial influence on the decreasing or increasing Al(VI) content and the increasing or

decreasing contents of Si(IV), Mg(VI), and Fe²⁺(VI) in the tetrahedral and octahedral sites (Cloutier et al., 2021).

In this study, sample LM 5, can serve as an example for confirming the influence of Tschermak substitutions. The sample does not have Fe(VI) and Mg(VI), despite having relatively low Si(IV) contents. In contrast, the sample contains relatively high Al(VI) content in the octahedral sites, as illustrated in Table 3.1. Consequently, the 2200 nm feature shifts towards the shorter wavelength. This suggests the potential substitution of Si(IV) by Al(IV) in the tetrahedral site and Fe(VI) or Mg(VI) by Al(VI) in the octahedral site. This salient observation, moreover, indicates the relation between the content of Al(VI), Fe(VI), and Mg(VI) in the octahedral site and Al(IV) and Si(IV) in the tetrahedral site. Thus, it implies a lower content of Fe(VI) and Mg(VI) in the octahedral site accompanied by a higher Al(VI) content in the octahedral site, while lower Si(IV) in the tetrahedral site correspondingly leads to higher Al(IV) content in the tetrahedral site.

In addition to the absence of Fe(VI) and Mg(VI) content, sample LM 5 is also characterized by the presence of Li(VI) in the octahedral site, as observed in Table 3.1. Considering the content of the octahedral cations (Fe and Mg), it is likely that the three octahedral sites of this sample could potentially be occupied by AlAl and a vacant site. According to Deer et al. (2013), the presence of Li(VI) can replace Al or enter the vacant sites. Given the higher concentration of Al(VI) in this sample, Li(VI) cation appear to occupy the vacant octahedral site. As a result, the 2200 nm feature shifts towards the shorter wavelength position. This indicates that the effect of Li(VI) can be attributed to the influence of the ion sitting next to Al(VI) in the octahedral site.

In contrast, sample LM 23 of the studied muscovite contains relatively high Fe(VI) and Mg(VI) contents while having low Al(VI) content in the octahedral sites (*Figure 7.6 and 7.7*). As a result, the 2200 nm absorption feature shifts to a higher wavelength. This shift is likely attributed to the potential substitutions of Al(VI) by Fe(VI) or Mg(VI) in the octahedral site, signifying that an increasing abundance of Fe(VI) and Mg(VI) leads to a decreasing abundance of Al(VI) in the octahedral site.

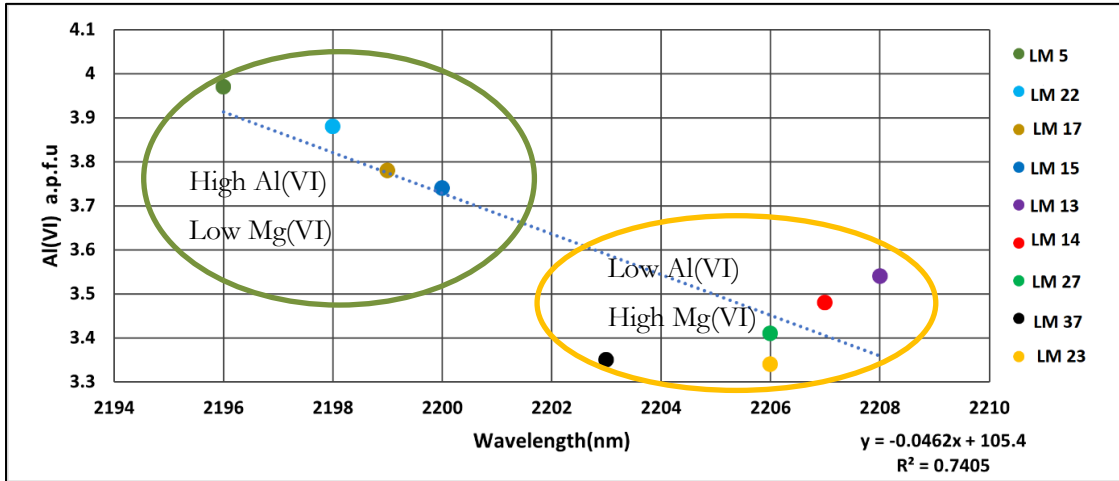


Figure 7.6: Relation between the observed wavelength position of the main cation around the 2200 nm absorption minimum in the reflection spectra of muscovite and their Al octahedral site occupancy calculated from the electron probe microanalysis. Linear regression results and R² values are shown at the bottom right.

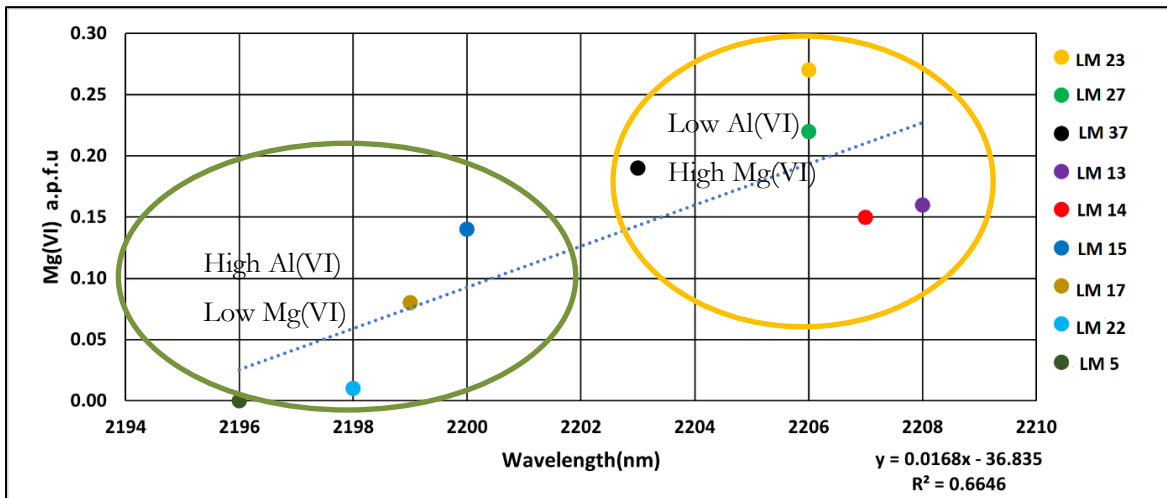


Figure 7.7: Relation between the observed wavelength position of the main cation around the 2200 nm absorption minimum in the reflection spectra of lepidolites and their Mg octahedral site occupancy calculated from the electron probe microanalysis. Linear regression results and R² values shown at bottom right.

In the case of lepidolite mica, the same pattern was observed: the 2200 nm absorption feature shifts towards the shorter wavelength with increasing Al(VI) content in the octahedral site. Similarly, in the scatter diagram plotting the 2200 nm feature against the Al(VI) content in the octahedral site, a systematic shift towards the shorter wavelength with increasing the Al(VI) content in the octahedral site was also observed (Figure 7.8). For instance, in sample LM 11, which contains a high Al(VI) content of 3.08 and a relatively low Li(VI) content of 3.05, the feature shifts towards the shorter wavelength positions. Conversely, sample LM 34 contains a relatively low Al(VI) content of 2.43 and a relatively high Li(VI) content of 3.18, resulting in the feature shifting towards the higher wavelength. Besides, compared to the other samples, sample LM 34 contains a relatively high content of Ti(VI) and Mn(VI) in the octahedral site (Table 3.1).

The observed shift is almost certainly attributed to the effect of the neighbouring ions sitting next to Al(VI) in the octahedral site. Al is bonded to OH, and next to this Al, there are two other trioctahedral ions sitting in the octahedral site. When more of these neighbouring sites are occupied by Li instead of another ion like Mg, Fe, or Al, then the feature shifts towards the shorter wavelength positions.

In the case of sample LM 11, the presence of Li(VI) occupying the site next to Al(VI) leads the feature to shift towards a shorter wavelength. Conversely, in sample LM 34, the presence of a relatively high content of Ti(VI) and Mn(VI) cations potentially enters the octahedral site as described by Redhammer et al. (2000). This suggests the higher concentrations of Ti and Mn, as well as the lower concentrations of Al(VI), may have a greater influence on the feature shifts towards the higher wavelength than the lithium driving the shift towards the shorter wavelength position.

It is important to note that in both samples, the content of Al(VI) and Li(VI) shows a negative correlation in the octahedral site. This correlation reveals that an increase in Al(VI) content corresponds to a decrease in Li(VI) content in the octahedral site.

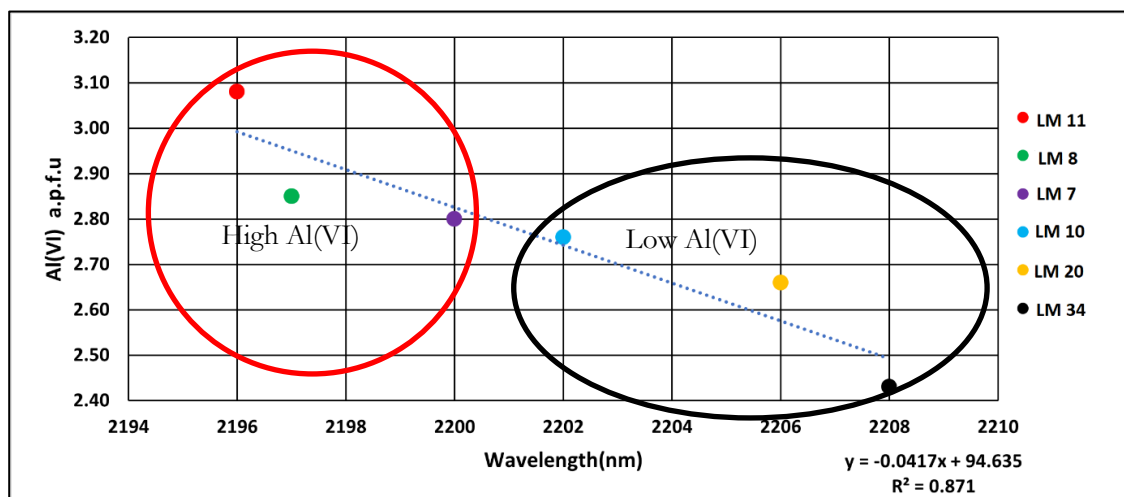


Figure 7.8: Relation between the observed wavelength position of the main cation around the 2200 nm absorption minimum in the reflection spectra of lepidolites and their Al octahedral site occupancy calculated from the electron probe microanalysis based on 22 oxygen. Linear regression results and R^2 values are shown at the bottom right.

In the studied siderophyllite mica, as described in Section 5.1.4 and depicted in Figure 5.7, a systematic shift was observed towards the shorter wavelength with increasing Fe(VI) and Mg(VI) content in the octahedral site. This shift is also attributed to Tschermak substitutions.

Involving $\text{Al}^{3+}(\text{IV}) + \text{Al}^{3+}(\text{VI}) \longleftrightarrow \text{Si}^{4+}(\text{IV}) + \text{Mg}^{2+}(\text{VI})$ or $\text{Fe}^{2+}(\text{VI})$. When Al(VI) substituted by Fe(VI) or Mg(VI) in the octahedral site, the feature shifts towards the shorter wavelength positions.

In summary, in the trioctahedral types of mica, such as siderophyllite, lepidolite, and polyolithionite, potential substitution of cations can occur in the octahedral and tetrahedral sites. For instance, a previous study by Redhammer et al.(2002) illustrates the effect of coupled substitution (Al-Tschermak substitution) in siderophyllite mica. This substitution involves $\text{Al}^{3+}(\text{IV})+\text{Al}^{3+}(\text{VI}) \longleftrightarrow \text{Si}^{4+}(\text{IV})+\text{Mg}^{2+}(\text{VI})$ or $\text{Fe}^{2+}(\text{VI})$ while various cations such as Li, Mn, and Ti can enter the octahedral sites. This coupled substitution progresses from siderophyllite towards lepidolite $2\text{Mg}^{2+} \longleftrightarrow \text{Al}^{3+}+\text{Li}^{+}$, in the octahedral site. In the tetrahedral site, substitution of more $\text{Si}^{4+}(\text{IV}) \longleftrightarrow \text{Al}^{3+}(\text{IV})$ in this case would require a replacement of 2^{+} ion with 1^{+} ion in the octahedral site to balance the charge (e.g., Mg^{2+} or Fe^{2+} by Li^{+}). Consequently, (Li, Li, Al) are the three ions in the octahedral site, which has a chemical formula of polyolithionite, $\text{KLi}_2\text{AlSi}_4\text{O}_{10}(\text{F},\text{OH})_2$. Therefore, going from lepidolite to polyolithionite, there is a decrease in Al(VI) and an increase in Li(VI) content in the octahedral site (as illustrated in Table 3.1).

Overall, the result obtained from this study indicates that the shift of the absorption features observed in the studied mica minerals are influenced by the presence of neighbouring ions sitting next to Al(VI) in the octahedral sites and the potential substitution of tetrahedral and octahedral cations. These factors can lead to changes in the vibrational environment and energy level, resulting in shifts in the absorption features.

7.3 Application to imaging spectroscopy on Li-bearing rock

The figures below show the SWIR wavelength map of the studied pegmatite rock sample. The sample was collected from a 20 m aplite-pegmatite dyke in Meldon aplite quarry, England. The Meldon aplite-pegmatite mainly consists of lithium-aluminum micas, quartz, albite, elbaite, and orthoclase minerals (Chaudhry, 2017).

As illustrated in Figures 7.9 and 7.10, the sample contains mica minerals within and outside of the veins. The wavelength map of the studied pegmatite sample in the 2190–2200 nm range is displayed in Figure 7.9. This wavelength range corresponds with the scatter diagram plotting the 2200 nm feature against Al(VI) content in the octahedral site. In the scatter diagram, the 2194–2200 nm indicates mica samples that contain high Al(VI) content. Similarly, in the wavelength image, the greenish to yellowish and pinkish color pixels in the 2194–2200 nm range discern the wavelength of micas with a high Al(VI) content.

In the 2200–2014 nm range, the wavelength map also highlights variations in Al(VI) contents in mica minerals (Figure 7.10). Similarly, the wavelength positions observed in the SWIR image also correspond with the scatter diagram plotting the 2200 nm feature against Al(VI) content in the octahedral site observed. In the wavelength map image, the blue and cyan color pixels exhibit the absorption features of mica minerals around 2200 nm. On the other hand, the greenish-colored pixels display the absorption features of mica minerals in the 2204–2207 nm range. In the scatter diagram, the samples depict absorption features around 2200 and 2202 nm, which contain high Al(VI) content, while low Al(VI) content is associated with the

absorption features in the 2204–2207 nm range. Hence, in the wavelength image, the blue pixels correspond with mica minerals that contain high Al(VI) content, and the greenish pixels observed in the 2202–2208 nm range are correlated with mica minerals that contain relatively low Al(VI) content.

Therefore, the wavelength shift observed in micas with varying Al(VI) content, detected using non-imaging SWIR spectroscopy, can also be effectively resolved and analyzed through the application of SWIR imaging spectroscopy.

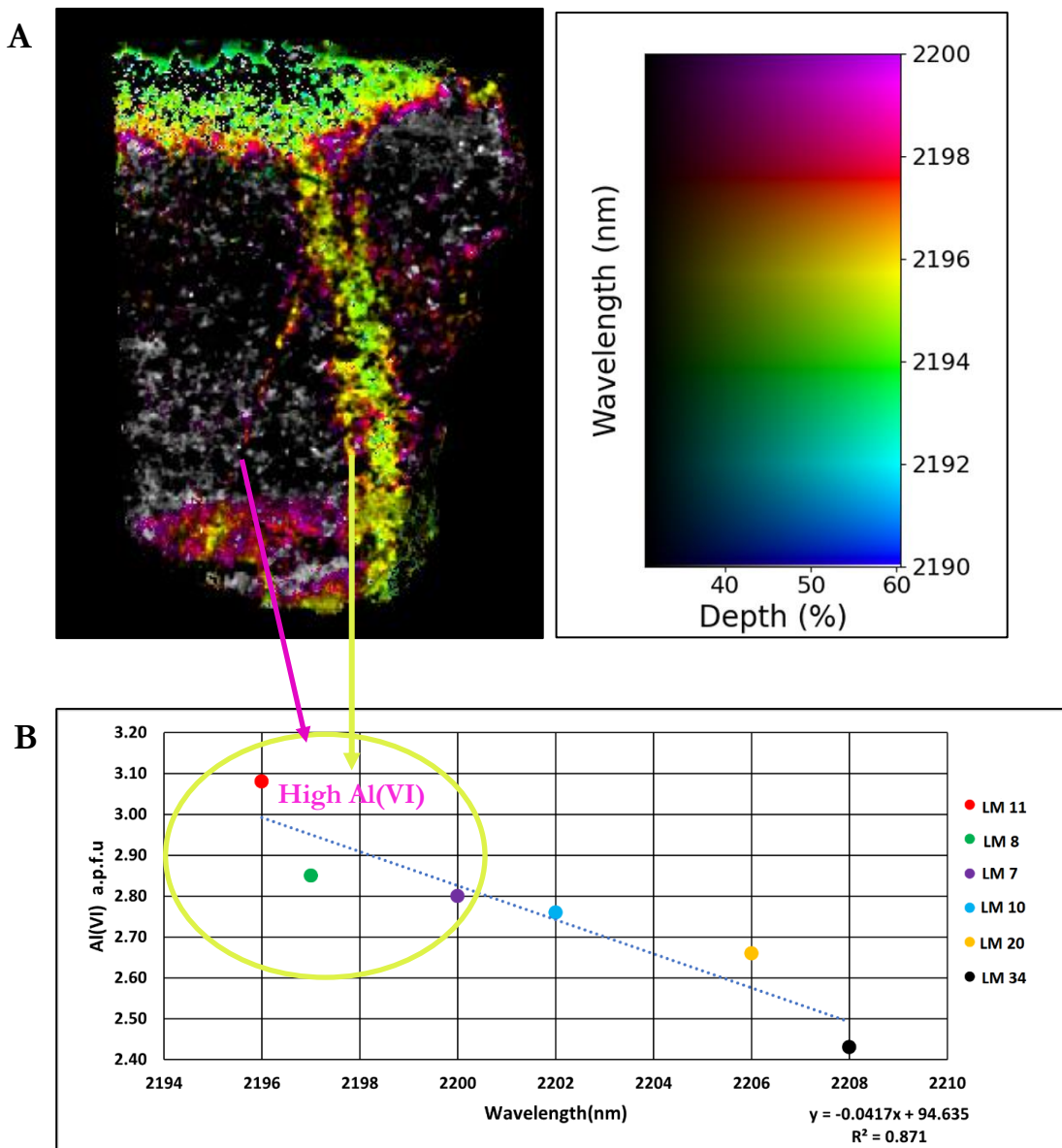


Figure 7.9: SWIR wavelength map of a pegmatite rock sample that contains mica minerals within and outside the veins. The image highlights mica minerals, which display absorption features in the 2190–2200 nm range (Figure A). Figure B displays the relation between the observed wavelength position of the main cation around the 2200 nm absorption minimum in the reflection spectra of lepidolite and their Al octahedral site occupancy, as calculated based on 22 oxygen atoms.

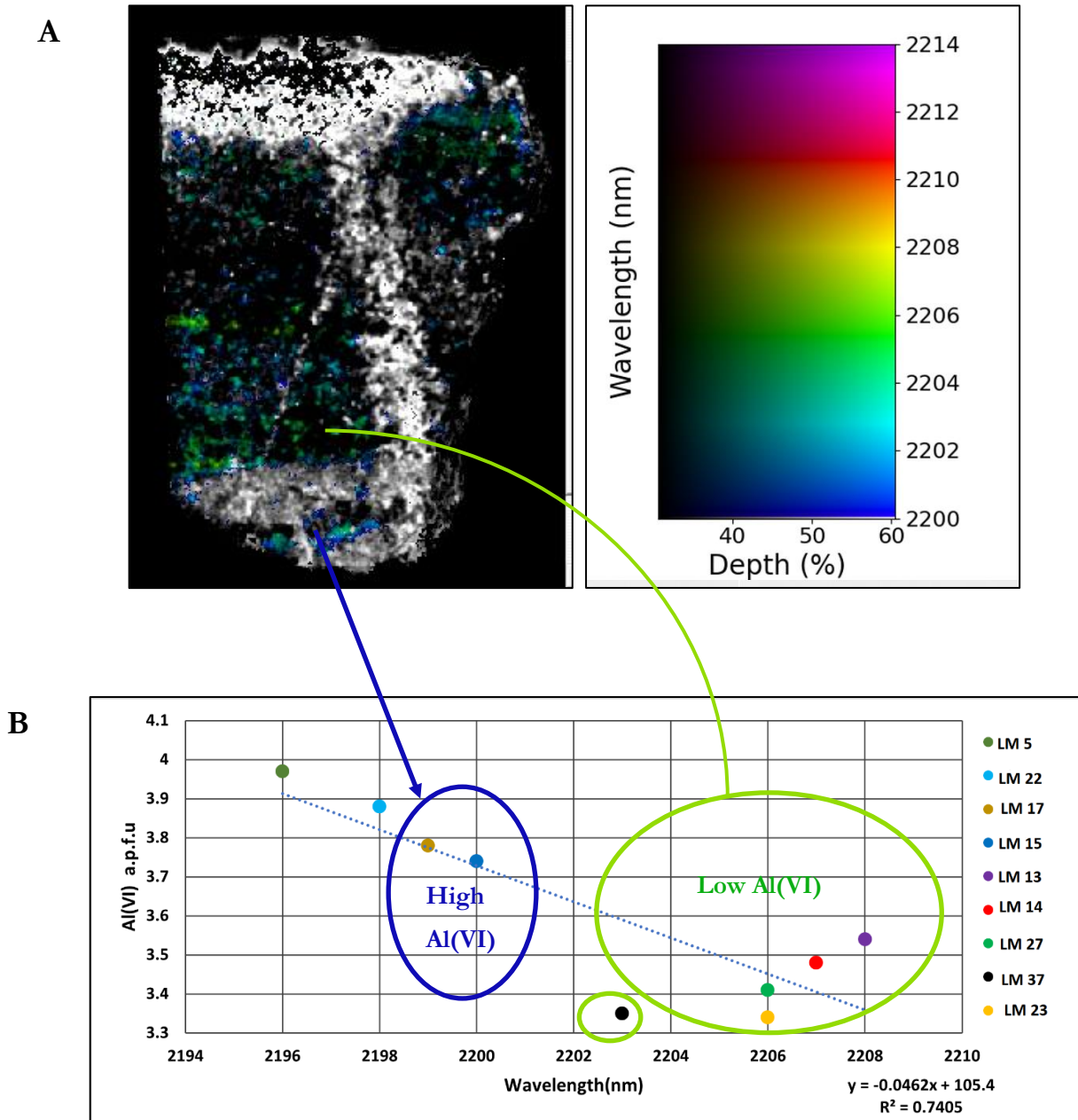


Figure 7.10: SWIR wavelength map of a pegmatite rock sample containing mica minerals with different Al(VI) content. The image highlights mica minerals that show absorption features in the 2200–2014 nm range (Figure A). Figure B depicts the relationship between the observed wavelength position of the main cation around the 2200 nm absorption minimum in the reflection spectra of muscovite and their Al octahedral site occupancy, as calculated based on 22 oxygen atoms.

8 CONCLUSION AND RECOMMENDATIONS

This study analyzed the spectral characteristics and effects of elemental substitutions on the shift of absorption features in the dioctahedral and trioctahedral types of mica. The study employed LWIR-MWIR, VNIR-SWIR spectroscopy integrated with electron microprobe analysis (EMPA) and X-ray diffraction (XRD). The results and discussion obtained from this study has led to the following conclusions;

Based on the results obtained from electron microprobe analysis (EMPA), the concentrations of tetrahedral and octahedral cations that comprise the studied mica minerals were calculated. Subsequently, a classification scheme was made using the parameters Mg-Li (*mgli*) and tFe+Mn+Ti-Al(VI) (*feal*), as calculated based on 11 oxygen stoichiometry. According to the parameters, mica minerals such as polyolithionite, lepidolite, zinnwaldite, siderophyllite, and muscovite were identified.

The X-ray diffraction (XRD) analytical method was found to be ineffective in the identification of the studied mica minerals. This difficulty arises because all the studied mica minerals depict similar diffraction patterns and peak positions, leading to difficulties in their differentiation.

The LWIR and MWIR absorption features in the 700–1100 cm^{-1} and 3500–3800 cm^{-1} ranges successfully distinguished the studied mica minerals. As discussed in the previous sections (Section 7.1), particularly in the 700–1100 cm^{-1} range, all the studied mica minerals, including polyolithionite, lepidolite, zinnwaldite, siderophyllite, muscovite, and fuchsite, exhibit distinct and distinguishable absorption features. Additionally, the absorption feature observed in the 700–1100 cm^{-1} depicts the absorption peak associated with the presence of Li-OH bending vibration around 720 cm^{-1} . The presence of the absorption peak attributed to Li-OH bending vibrations aids in identifying lithium-bearing micas. Moreover, the absorption feature observed in the LWIR part of the spectrum detects the systematic shift of absorption features, specifically in muscovite mica around the 820 cm^{-1} and 3620 cm^{-1} regions.

The analysis obtained from VNIR and SWIR spectroscopy in the 350–2500 nm range successfully identifies the studied mica minerals due to the presence of electronic processes in transition metals such as Mn, Ti, and Fe, as well as the vibrational bonds attributed to Al-OH, Fe-OH, and Mg-OH. However, the specific wavelength position associated with the Li-OH could not be determined. As a result, distinguishing lithium-bearing mica from non-lithium-bearing mica was not possible.

On the other hand, the absorption features observed in the 2100–2500 nm range effectively discern a systematic shift of wavelength positions associated with elemental substitutions of octahedral cations such as Al(VI), Fe(VI), and Mg(VI). Besides, the scatter diagrams plotting the 2200 nm feature against the content of Al(VI), Mg(VI), and Si(IV) in the tetrahedral and octahedral sites also exhibits the systematic shift of the absorption features.

Recommendations

Based on the result obtained from this study, the recommendation is as follows,

This study used an estimated and assumed lithium concentration to identify lithium-bearing mica, taking into account the limitations of EMPA in detecting lithium concentration. However, there was uncertainty owing to the assumed Li concentration. Since lithium (Li) is a critical octahedral cation for distinguishing lithium-bearing mica, measuring the concentration of lithium is highly recommended. Alternatively, if direct measurement of lithium is not possible, measuring the concentrations of fluorine (F) is strongly recommended. This recommendation is due to the positive correlation between Li and F content in mica minerals.

The SWIR spectral characteristics acquired using the ASD FieldSpec3 spectrometer have a limitation in determining the wavelength positions of absorption features associated with Li-OH vibration. As a result, a high-spectral-resolution spectrometer is recommended to discern and identify the feature attributed to Li-OH.

This study used a variety of mica minerals to analyze their spectral characteristics and the effects of elemental substitutions. Nevertheless, due to the limited number of samples, determining the effect of elemental substitution on the shifts of absorption features could not be achieved, particularly in polyolithionite and zinnwaldite mica. Therefore, it is recommended to acquire more samples of polyolithionite and zinnwaldite to enable a more comprehensive analysis. Additionally, other varieties of dioctahedral types of mica are also recommended to understand their spectral characteristics and determine the effect of elemental substitution on changing the chemical compositions of the minerals.

LIST OF REFERENCES

- ASD. (2011). FieldSpec ® 4 User Manual. *ASD Document 600979 Rev. A*, 110. <http://www.geo-informatie.nl/courses/grs60312/material2017/manuals/600540-JFieldSpec3UserManual.pdf>
- Besson, G., & Drits, V. A. (1997). Refined relationships between chemical composition of dioctahedral fine-grained micaceous minerals and their infrared spectra within the OH Stretching region. Part II: The main factors affecting OH vibrations and quantitative analysis. *Clays and Clay Minerals*, *45*(2), 170–183. <https://doi.org/10.1346/CCMN.1997.0450205>
- Bishop, J. L., Lane, M. D., Dyar, M. D., & Brown, A. J. (2008). Reflectance and emission spectroscopy study of four groups of phyllosilicates: smectites, kaolinite-serpentines, chlorites and micas. *Clay Minerals*, *43*(1), 35–54. <https://doi.org/10.1180/claymin.2008.043.1.03>
- Breiter, K., Hložková, M., Korbelová, Z., & Galiová, M. V. (2019). Diversity of lithium mica compositions in mineralized granite–greisen system: Cínovec Li-Sn-W deposit, Erzgebirge. *Ore Geology Reviews*, *106*(May 2018), 12–27. <https://doi.org/10.1016/j.oregeorev.2019.01.013>
- Cardoso-Fernandes, J., Silva, J., Perrotta, M. M., Lima, A., Teodoro, A. C., Ribeiro, M. A., Dias, F., Barrès, O., Cauzid, J., & Roda-Robles, E. (2021). Interpretation of the reflectance spectra of lithium (Li) minerals and pegmatites: A case study for mineralogical and lithological identification in the fregeneda-almendra area. *Remote Sensing*, *13*(18). <https://doi.org/10.3390/rs13183688>
- Cardoso-Fernandes, J., Teodoro, A. C., Lima, A., Perrotta, M., & Roda-Robles, E. (2020). Detecting Lithium (Li) mineralizations from space: Current research and future perspectives. *Applied Sciences (Switzerland)*, *10*(5). <https://doi.org/10.3390/app10051785>
- Chaudhry, M. N. (2017). *Lithium-aluminium micas from the Meldon aplite, Devonshire, England. September 1973*. <https://doi.org/10.1180/minmag.1973.039.303.05>
- Clark, R. N., King, T. V. V., Klejwa, M., Swayze, G. A., & Vergo, N. (1990). High spectral resolution reflectance spectroscopy of minerals. *Journal of Geophysical Research*, *95*(B8). <https://doi.org/10.1029/jb095ib08p12653>
- Clark, Roger N. (1999). Chapter 1: Spectroscopy of Rocks and Minerals, and Principles of Spectroscopy. *Manual of Remote Sensing, Volume 3*, 3, 3–58 <https://doi.org/10.1111/j.1945-5100.2004.tb00079.x>
- Cloutier, J., Piercey, S. J., Al, V. I., & Al, V. I. (2021). *Mineralogy, Mineral Chemistry and SWIR Spectral Reflectance of Chlorite and White Mica*. *Minerals* 2021, *11*, 471. <https://doi.org/10.3390/min11050471>
- Deer, W. A., Howie, R. A., & Zussman, J. (2013). An Introduction to the Rock-Forming Minerals. In *An Introduction to the Rock-Forming Minerals*. <https://doi.org/10.1180/dhz3751725>
- Dini, A., Lattanzi, P., Ruggieri, G., & Trumpy, E. (2022). Lithium Occurrence in Italy—An Overview. *Minerals*, *12*(8), 1–27. <https://doi.org/10.3390/min12080945>
- Duke, E. F. (1994). Near infrared spectra of muscovite, Tschermak substitution, and metamorphic reaction progress: implications for remote sensing. *Geology*, *22*(7), 621–624.

- <https://doi.org/10.1130/0091-7613>
- European Commission. (2020). Critical Raw Materials for Strategic Technologies and Sectors in the EU. AForesight Study. In *Critical Raw Materials Factsheets*. <https://doi.org/10.2873/92480>
- Ferro, P., & Bonollo, F. (2019). Materials selection in a critical raw materials perspective. *Materials and Design*, 177, 107848. <https://doi.org/10.1016/j.matdes.2019.107848>
- Gourcerol, B., Gloaguen, E., Melleton, J., Tuduri, J., & Galiegue, X. (2019). Re-assessing the European lithium resource potential – A review of hard-rock resources and metallogeny. *Ore Geology Reviews*, 109, 494–519. <https://doi.org/10.1016/j.oregeorev.2019.04.015>
- Hecker, C. A., van Ruitenbeek, F. J. A., van der Werff, H. M. A., Bakker, W. H., Hewson, R., & van der Meer, F. D. (2019). Spectral absorption feature analysis for finding ore: A tutorial on using the method in geological remote sensing. *IEEE Geoscience and Remote Sensing Magazine*, 7(2), 51–71. <https://doi.org/10.1109/MGRS.2019.2899193>
- Jenkins, D. M. (1989). Empirical study of the infrared lattice vibrations (1100-350 cm⁻¹) of phlogopite. *Physics and Chemistry of Minerals*, 16(4), 408–414. <https://doi.org/10.1007/BF00199563>
- Kavanagh, L., Keohane, J., Cabellos, G. G., Lloyd, A., & Cleary, J. (2018). Global lithium sources-industrial use and future in the electric vehicle industry: A review. *Resources*, 7(3). <https://doi.org/10.3390/resources7030057>
- Kesler, S. E., Gruber, P. W., Medina, P. A., Keoleian, G. A., Everson, M. P., & Wallington, T. J. (2012). Global lithium resources: Relative importance of pegmatite, brine and other deposits. *Ore Geology Reviews*, 48, 55–69. <https://doi.org/10.1016/j.oregeorev.2012.05.006>
- Kholoshyn, I., Panteleeva, N., Trunin, O., Burman, L., & Kalinichenko, O. (2020). Infrared spectroscopy as the method for evaluating technological properties of minerals and their behavior in technological processes. *E3S Web of Conferences*, 166. <https://doi.org/10.1051/e3sconf/202016602002>
- LeGras, M., Laukamp, C., Lau, I. C., Mason, P., & CSIRO. (2018). NVCL Spectral Reference Library - Phyllosilicates Part 2: Micas. *NVCL Spectral Reference Library, EP183095*, 66. www.csiro.au
- Li, A., Yang, W. Bin, Shan, Q., Yu, X. Z., Xu, G. Z., Han, J. S., Zhang, Z. Y., Weng, Q., & Zhao, X. C. (2021). Mineralogy and short wavelength infrared spectral analysis of white mica in the No. 782 REE–Nb–Zr deposit, NE China. *Ore Geology Reviews*, 138. <https://doi.org/10.1016/j.oregeorev.2021.104390>
- Lypaczewski, P., & Rivard, B. (2018). Estimating the Mg# and AlVI content of biotite and chlorite from shortwave infrared reflectance spectroscopy: Predictive equations and recommendations for their use. *International Journal of Applied Earth Observation and Geoinformation*, 68, 116–126. <https://doi.org/10.1016/j.jag.2018.02.003>
- Melka, K. (2009). A scheme for the classification of micaceous minerals: 6(153), 69–75.
- Pommeret, A., Ricci, F., & Schubert, K. (2022). Critical raw materials for the energy transition. *European Economic Review*, 141(November 2021), 103991. <https://doi.org/10.1016/j.euroecorev.2021.103991>

- Redhammer, G. J., Beran, A., Schneider, J., Amthauer, G., & Lottermoser, W. (2000). Spectroscopic and structural properties of synthetic micas on the annite-siderophyllite binary: Synthesis, crystal structure refinement, Mossbauer, and infrared spectroscopy. *American Mineralogist*, *85*(3–4), 449–465. <https://doi.org/10.2138/am-2000-0406>
- Robert, J., Beny, J. M., Benyani, C., & Volfinger, M. (1989). Characterization of lepidolite By Raman and infrared spectrometries. I. relationship between OH-stretching wavenumbers and composition. *Canadian mineralogist*, *27*, 225–235.
- Savitri, K. P., Hecker, C., van der Meer, F. D., & Sidik, R. P. (2021). VNIR-SWIR infrared (imaging) spectroscopy for geothermal exploration: Current status and future directions. *Geothermics*, *96*(July), 102178. <https://doi.org/10.1016/j.geothermics.2021.102178>
- Tischendorf, G., Förster, H.-J., & Gottesmann, B. (1999). The correlation between lithium and magnesium in trioctahedral micas: Improved equations for Li 2 O estimation from MgO data . *Mineralogical Magazine*, *63*(1), 57–74. <https://doi.org/10.1180/002646199548312>
- Tischendorf, G., Förster, H.-J., Gottesmann, B., & Rieder, M. (2007). True and brittle micas: composition and solid-solution series. *Mineralogical Magazine*, *71*(3), 285–320. <https://doi.org/10.1180/minmag.2007.071.3.285>
- Tischendorf, G., Rieder, M., Förster, H.-J., Gottesmann, B., & Guidotti, C. V. (2004). A new graphical presentation and subdivision of potassium micas. *Mineralogical Magazine*, *68*(4), 649–667. <https://doi.org/10.1180/0026461046840210>
- Yang, K., Huntington, J. F., Gemmell, J. B., & Scott, K. M. (2011). Variations in composition and abundance of white mica in the hydrothermal alteration system at Hellyer, Tasmania, as revealed by infrared reflectance spectroscopy. *Journal of Geochemical Exploration*, *108*(2), 143–156. <https://doi.org/10.1016/j.gexplo.2011.01.001>
- Yavuz, F. (2001). LIMICA: A program for estimating Li from electron-microprobe analyses and classifying trioctahedral micas in terms of composition and octahedral site occupancy. *Computers and Geosciences*, *27*(2), 215–227. [https://doi.org/10.1016/S0098-3004\(00\)00086-8](https://doi.org/10.1016/S0098-3004(00)00086-8)
- Zviagina, B. B., Drits, V. A., & Dorzhieva, O. V. (2020). Distinguishing features and identification criteria for K-dioctahedral 1M micas (Illite-aluminocladonite and illite-glaucanite-celadonite series) from middle-infrared spectroscopy data. *Minerals*, *10*(2). <https://doi.org/10.3390/min10020153>

APPENDICES

Appendix 1: Mica mineral samples were used for this study. Samples were chosen based on varying species of di- and tri-octahedral types of mica. The given names of minerals are based on EMAP, LWIR, MWIR, VNIR, and SWIR spectroscopy results.

Sample ID	Locality	Sample description	Mineral
LM 3	Nanpean Quarry, St Austell, Cornwall, UK	Topaz granite sample NAN4	Zinnwaldite
LM 5	Harding, New Mexico	Lithium muscovite mineral sample	Muscovite
LM 6	Cinovec, Czech Rep	Polyolithionite mineral sample	Polyolithionite
LM 7	Near Harare, Zimbabwe	Lepidolite mineral sample	Lepidolite
LM 8	Unknown	Lepidolite mineral sample	Lepidolite
LM 10	Goncalo, Guarda, Portugal	Lepidolite-rich rock sample	Lepidolite
LM 11	Guarda, Portugal	Lepidolite-rich rock sample	Lepidolite
LM 12	Unknown	Biotite sheet crystal?	Siderophyllite
LM 13	Unknown	Muscovite sheet crystal	Muscovite
LM 14	Unknown	Very large muscovite sheet	Muscovite
LM 15	Unknown	Pegmatite rock sample with large micas	Muscovite
LM 16	Unknown	Large phlogopite crystal?	Siderophyllite
LM 17	Unknown	Large muscovite crystal	Muscovite
LM 18	Unknown	Large lepidolite crystal	Lepidolite
LM 20	Haapaluoma pegmatite, Finland	Pegmatite rock sample	Lepidolite
LM 22	Unknown	Pegmatite with large tourmaline	Muscovite
LM 23	Unknown	Micaceous pegmatite	Muscovite
LM 24	Unknown	Small mineral sample	Fuchsite
LM 25	Cap de Creus Pegmatite body	Pegmatite, CP51	Muscovite
LM 27	Unknown	Mica flakes from the ITC display cabinet	Muscovite
LM 28	Tor Rocks Quarry, Harford, Devon, UK	Granite rock	Biotite

LM 32	Cinovec, Teplia, Czech Rep	Micaceous pegmatite rock	Zinnwaldite
LM 34	Kalba Range, Kazakhstan	Small sample lepidolite+albite	Lepidolite
LM 35	Kit Hill, Cornwall, UK	Granite, the small piece only KH1	Muscovite and Biotite
LM 36	Carn Brea, Cornwall, UK	Granite rock sample	Muscovite and Biotite
LM 37	Lee Moor Quarry, Devon, UK	Greisenised granite, Lee Moor 1	Muscovite
LM 38	Unknown	Decorative biotite-granite rock	Siderophyllite

SPECTRAL ANALYSIS OF LITHIUM-BEARING MICAS WITH SHORTWAVE AND LONGWAVE INFRARED SPECTROSCOPY

Appendix 2: Raw Electron microprobe analysis (EMPA) of the studied mica minerals

Sample	LM 6				LM 7					LM 8						LM 11							
No. grains	1	2	3	4	1	2	3	4	5	1	2	3	4	5	6	1	2	3	4	5	6	7	
	Major element (Wt%)																						
SiO ₂	60.42	60.67	59.37	60.68	52.08	50.28	53.64	50.99	51.77	46.93	47.61	47.51	46.86	46.36	45.92	45.09	51.17	45.32	50.13	50.44	46.33	46.29	
TiO ₂	1.62	2.04	1.39	2.00	0.00	0.00	0.00	0.00	0.00	0.03	0.04	0.02	0.02	0.05	0.05	0.00	0.00	0.00	0.00	0.00	0.00	0.00	
AlO ₂	11.93	11.58	12.61	11.84	26.38	26.52	27.78	26.22	26.59	32.22	25.70	28.71	27.79	35.29	35.27	38.70	27.22	38.17	28.62	28.43	37.87	37.99	
Cr ₂ O ₃	0.00	0.00	0.00	0.00	0.00	0.00	0.00	0.00	0.00	0.00	0.00	0.00	0.00	0.00	0.00	0.00	0.00	0.00	0.00	0.00	0.00	0.00	
FeO	1.10	1.39	1.09	1.11	0.00	0.00	0.02	0.03	0.01	0.09	0.20	0.12	0.12	0.02	0.03	0.03	0.07	0.03	0.01	0.05	0.04	0.02	
MnO	0.21	0.26	0.17	0.26	0.78	0.75	0.80	0.85	0.90	1.94	3.69	2.42	3.10	0.95	1.08	0.08	1.02	0.16	0.87	0.90	0.13	0.12	
MgO	0.00	0.00	0.00	0.00	0.00	0.00	0.00	0.00	0.00	0.00	0.00	0.00	0.00	0.00	0.00	0.00	0.00	0.00	0.00	0.00	0.00	0.00	
CaO	0.00	0.00	0.00	0.00	0.00	0.00	0.00	0.00	0.00	0.00	0.00	0.00	0.00	0.00	0.00	0.00	0.00	0.00	0.00	0.00	0.00	0.00	
Na ₂ O	0.23	0.27	0.21	0.26	0.26	0.28	0.23	0.24	0.24	0.25	0.17	0.22	0.19	0.41	0.36	0.59	0.11	0.56	0.16	0.13	0.52	0.54	
K ₂ O	11.84	11.71	11.90	11.82	9.09	8.90	9.13	9.08	9.18	10.23	9.89	10.05	9.98	10.19	10.30	9.33	9.02	9.31	8.79	8.88	9.28	9.34	

SPECTRAL ANALYSIS OF LITHIUM-BEARING MICAS WITH SHORTWAVE AND LONGWAVE INFRARED SPECTROSCOPY

Sample	LM 10			LM 20			LM 34			LM 1			LM 3			
	No.grains	1	2	3	1	2	3	1	2	3	1	2	3	1	2	3
SiO ₂	52.90	52.43	52.35	52.64	53.86	53.86	49.90	50.97	52.55	54.95	54.49	54.59	49.27	44.88	45.07	49.47
TiO ₂	0.00	0.00	0.00	0.00	0.00	0.00	0.22	0.23	0.22	0.08	0.05	0.08	0.35	0.25	0.40	0.32
AlO ₂	26.30	25.97	26.44	24.29	24.16	23.82	24.36	23.08	23.63	23.55	23.93	23.46	20.83	22.16	21.82	20.92
Cr ₂ O ₃	0.00	0.01	0.00	0.00	0.01	0.00	0.00	0.01	0.00	0.00	0.02	0.01	0.00	0.00	0.01	0.00
FeO	0.05	0.05	0.06	0.01	0.03	0.04	0.00	0.01	0.00	0.21	0.09	0.08	1.79	13.48	12.86	10.02
MnO	0.25	0.22	0.25	0.45	0.48	0.42	2.73	4.26	3.73	0.37	0.34	0.33	0.14	0.16	0.20	0.13
MgO	0.00	0.00	0.00	0.00	0.00	0.00	0.00	0.00	0.00	0.00	0.01	0.00	0.23	0.20	0.24	0.23
CaO	0.00	0.00	0.00	0.00	0.00	0.00	0.00	0.00	0.00	0.00	0.00	0.00	0.00	0.00	0.00	0.00
Na ₂ O	0.26	0.31	0.32	0.23	0.16	0.12	0.32	0.27	0.22	0.47	0.45	0.41	0.19	0.10	0.31	0.17
K ₂ O	10.81	10.66	10.71	11.35	11.46	9.96	10.83	10.88	10.97	10.59	10.65	10.67	10.33	10.48	10.00	10.28

SPECTRAL ANALYSIS OF LITHIUM-BEARING MICAS WITH SHORTWAVE AND LONGWAVE INFRARED SPECTROSCOPY

Sample	LM 32			LM 28			LM 36					LM 38				LM 5					
No.grains	1	2	3	1	2	3	1	2	3	4	5	1	2	3	4	1	2	3	4	5	6
SiO ₂	46.63	47.04	47.67	37.85	43.46	36.18	34.54	34.74	34.79	33.13	34.57	35.16	34.99	35.02	34.45	44.01	43.61	44.22	43.88	44.43	44.49
TiO ₂	0.00	0.00	0.00	1.56	0.75	3.37	1.84	1.87	1.88	3.07	2.32	4.32	4.27	4.20	4.23	0.01	0.01	0.00	0.01	0.00	0.00
AlO ₂	21.14	20.62	20.78	21.42	26.92	19.66	19.96	19.76	19.47	19.70	20.06	14.85	14.56	14.50	14.27	37.83	37.51	38.12	37.66	37.84	38.04
Cr ₂ O ₃	0.00	0.01	0.00	0.00	0.00	0.00	0.01	0.00	0.00	0.04	0.00	0.02	0.03	0.00	0.04	0.00	0.00	0.00	0.00	0.00	0.00
FeO	12.07	11.42	11.84	19.24	10.91	21.54	20.38	19.86	20.15	21.38	20.02	22.06	22.52	22.70	22.08	0.06	0.08	0.04	0.06	0.11	0.07
MnO	1.39	1.49	1.26	0.21	0.12	0.23	0.33	0.36	0.40	0.37	0.31	0.27	0.31	0.31	0.29	0.17	0.18	0.09	0.17	0.21	0.18
MgO	0.00	0.00	0.00	4.68	3.12	4.03	4.88	4.98	5.07	4.31	4.65	7.98	8.04	8.16	8.01	0.00	0.00	0.00	0.00	0.00	0.00
CaO	0.00	0.00	0.00	0.00	0.04	0.00	0.01	0.00	0.00	0.00	0.00	0.00	0.00	0.00	0.00	0.00	0.00	0.00	0.00	0.00	0.00
Na ₂ O	0.16	0.15	0.13	0.08	0.20	0.10	0.15	0.12	0.12	0.18	0.20	0.04	0.07	0.08	0.07	0.52	0.54	0.55	0.53	0.54	0.52
K ₂ O	10.43	10.31	10.35	9.76	10.45	9.52	9.51	9.48	9.58	9.39	9.50	9.56	9.57	9.56	9.44	10.99	11.00	11.068	11.04	11.13	11.04

SPECTRAL ANALYSIS OF LITHIUM-BEARING MICAS WITH SHORTWAVE AND LONGWAVE INFRARED SPECTROSCOPY

Sample	LM 13			LM 14		LM 15			LM 17			LM 22			LM 23				LM 27		
No.grains	1	2	3	1	2	1	2	3	1	2	3	1	2	3	1	2	3	4	1	2	3
SiO ₂	46.85	47.41	44.92	45.80	40.48	46.97	46.50	47.24	46.33	47.33	45.94	46.63	45.77	46.54	44.86	44.99	44.92	45.36	44.72	45.27	45.52
TiO ₂	0.15	0.12	0.13	0.36	0.40	0.80	0.67	0.69	0.27	0.30	0.28	0.14	0.14	0.16	0.66	0.70	0.78	0.72	0.52	0.48	0.61
AlO ₂	33.96	34.52	32.68	32.44	31.38	37.37	36.99	37.67	36.92	37.63	37.63	38.06	37.57	38.24	32.66	32.70	32.31	33.16	31.33	31.85	32.32
Cr ₂ O ₃	0.00	0.00	0.01	0.01	0.00	0.00	0.00	0.00	0.00	0.00	0.00	0.00	0.01	0.00	0.01	0.00	0.00	0.03	0.00	0.01	0.00
FeO	3.92	3.88	3.31	4.01	4.04	0.87	0.84	0.82	1.52	1.52	1.47	1.40	1.19	1.24	4.63	4.52	4.51	4.44	4.97	4.96	5.04
MnO	0.01	0.01	0.04	0.00	0.00	0.01	0.01	0.02	0.00	0.00	0.00	0.02	0.04	0.04	0.11	0.10	0.10	0.12	0.09	0.12	0.10
MgO	0.97	0.92	0.92	0.18	1.21	0.73	0.75	0.76	0.51	0.48	0.51	0.16	0.17	0.17	1.37	1.28	1.39	1.36	1.03	0.98	1.15
CaO	0.00	0.00	0.00	0.00	0.00	0.00	0.00	0.01	0.00	0.00	0.00	0.00	0.00	0.00	0.00	0.00	0.00	0.00	0.00	0.00	0.00
Na ₂ O	0.40	0.50	0.47	0.04	0.63	0.78	0.76	0.80	0.86	0.86	0.91	0.66	0.45	0.64	0.51	0.46	0.53	0.52	0.61	0.53	0.63
K ₂ O	11.12	10.93	10.02	10.48	10.59	10.67	10.67	10.68	10.57	10.66	10.55	10.88	11.13	10.85	10.83	10.82	10.84	10.88	10.67	10.90	10.67

SPECTRAL ANALYSIS OF LITHIUM-BEARING MICAS WITH SHORTWAVE AND LONGWAVE INFRARED SPECTROSCOPY

Sample	LM 37				LM 24		
	No.grains	1	2	3	4	1	2
SiO ₂	43.75	45.93	46.00	44.29	47.20	47.64	47.21
TiO ₂	0.37	0.33	0.31	0.37	0.40	0.41	0.52
AlO ₂	33.63	34.69	34.86	34.35	30.93	32.03	34.79
Cr ₂ O ₃	0.00	0.00	0.00	0.00	1.64	1.13	0.88
FeO	2.34	2.74	2.35	2.14	1.61	1.79	0.98
MnO	0.06	0.10	0.04	0.06	0.00	0.00	0.00
MgO	0.91	0.95	1.05	0.93	2.62	2.65	1.55
CaO	0.00	0.00	0.00	0.00	0.00	0.00	0.00
Na ₂ O	0.82	0.78	0.83	0.81	0.77	0.90	1.18
K ₂ O	10.24	10.47	10.42	10.49	10.18	10.10	9.91